

https://dspace.org/

Investigating the use of alumina (Al2O3) to substitute magnesia (MgO) in capsule components for diamond synthesis in high pressure high temperature (HPHT) process

Mazula, Maqhawe

2020-04

https://hdl.handle.net/10539/30082

Downloaded from a DSpace repository. https://dspace.org/

Investigating the use of alumina (Al_2O_3) to substitute magnesia (MgO) in capsule components for diamond synthesis in high pressure high temperature (HPHT) process

Maqhawe Mazula

A dissertation submitted to the Faculty of Engineering and the Built Environment, University of the Witwatersrand, Johannesburg, in fulfilment of the requirements for the degree of Master of Science in Engineering.

Johannesburg, April 2020

Declaration

I declare that this dissertation is my own unaided work. It is being submitted to the degree of Master of Science to the University of the Witwatersrand, Johannesburg. It has not been submitted before for any degree or examination to any other university.

_____

Maqhawe Mazula

23 day of April 2020

Dedication

This dissertation is dedicated to my wife, parents, brothers and sisters

Acknowledgements

I would like to offer my sincere gratitude to my Witwatersrand University supervisor Prof I Sigalas and my co-supervisor from Element Six Pty Ltd Dr F Schoofs for tremendous supervisory role offered. Your endless supervisory support made me complete this research work.

I would like to thank the Element Six Pty Ltd Characterisation Quality department for the support offered and the use of their Characterisation Laboratory, equipment and support personnel Yvonne, Itumeleng, Zandile, Maggie, Khosi, Monica, Nthabiseng, Sibusiso, Eric and William.

A special thank you to Element Six – ZAPRO at Springs for project financial support. Mintek in Johannesburg, Element Six – GIC in the UK, Element Six – SEPRO in Sweden for assisting with other experimental work.

To my amazing wife, parents and my brothers and sisters for the encouragement offered during the study. Without your support, this research work would have lacked the necessary support you offered.

Abstract

The research work described in this dissertation concerns an investigation into the feasibility of replacing magnesia with alumina, as a seedpad material for diamond synthesis from diamond seeds, in the high pressure high temperature 5 GPa, 1450 ^{o}C, (HPHT) cubic press. A seedpad is a magnesia ceramic disc with diamond seeds crystals embedded at defined orientation and spacing onto a disc. Seedpad purity is critical to prevent contaminating or destabilising HPHT diamond synthesis. The supplied commercial magnesia grade used by Element Six Pty Ltd for seedpads manufacture, Nedmag has a purity of 98.5 % MgO, the remainder accounts for impurities like CaO, B_2O_3 and SiO_2. MgO and CaO have the ability to absorb atmospheric moisture to form hydroxides, B_2O_3 and SiO_2 may contaminate diamond synthesis by forming inclusions in the crystalline lattice. Magnesia seedpads are pre-treated in the 1140 ^{o}C vacuum furnace to decompose moisture and impurities, and stored in a nitrogen cabinet to prevent moisture re-absorption. Alternative seedpad material not susceptible to moisture absorption, of higher purity than Nedmag, able to make seedpads with sufficient strength comparable to magnesia seedpads was investigated.

Spray dried alumina, spray dried from KSM99, a high grade alumina powder sourced from Albemarle GmbH, Germany, was found to be a possible alternative powder for making higher purity alumina seedpad with a sufficient strength comparable to magnesia seedpad. The moisture test conducted proves magnesia (Nedmag) has a greater moisture absorption than alumina (KSM99) in ambient air. The spray dried magnesia and alumina powders were fully characterised, uniaxial compacted and fired to specific seedpad compacts density. A test to compare compressive fracture strength for both materials was done on an Instron mechanical test apparatus on cylindrical magnesia and alumina compacts, alumina compacts showed the mechanical strength required for seedpads manufacture. Graphite with metal solvents (GMS) prepared using Element Six Pty Ltd method, were used as a carbon source for diamond synthesis in the HPHT cubic press. The stability of magnesia and alumina in the presence of (GMS) at HPHT diamond synthesis condition shows suitability for both ceramics to be used as seedpads. The diamond crystals synthesised from magnesia seedpads and alumina seedpads were of similar colour and morphology.

Table of Contents

Contents

Declaration ii

Dedication iii

Acknowledgements iv

Abstract v

Table of Contents vi

List of Figures x

List of Tables xiv

List of Abbreviations and Symbols xv

Chapter 1: Introduction 1

Chapter 2: Literature Review 4

2.1 Synthetic diamond 4

2.1.1 The crystallography of graphite and diamond 4

2.1.2 Physical properties of graphite and diamond 5

2.1.3 Synthesis of diamond 6

2.1.4 High Pressure High Temperature (HPHT) diamond synthesis 7

2.2 Alumina and magnesia 15

2.2.1 Crystallography and phases of magnesia and alumina 16

2.2.2 Physical and mechanical properties of magnesia and alumina 18

2.3 Ceramic components manufacture 18

2.3.1 Preparation of powders for compaction 19

2.3.2 Compacting of powders 19

2.3.3 Sintering 22

2.4 Mechanical properties of materials 24

2.4.1 Tensile tests 24

2.4.2 Compression tests 25

2.4.3 Failure of brittle materials 26
2.4.4 Distribution of flaws in ceramic materials 28
Chapter 3: Experimental Methods 32
3.1 Raw materials used for the study 32
3.1.1 Spray dried alumina and Spray dried magnesia 32
3.1.2 Graphite and metal solvents (GMS) 33
3.1.3 Diamond seeds 33
3.1.4 Capsule components 34
3.2 Characterisation of raw materials 34
3.2.1 Powder particle size distribution (PSD) 34
3.2.2 Powder moisture 35
3.2.3 Powder bulk and tap density 35
3.2.4 Powder loss on ignition (LOI) 37
3.2.5 X-ray fluorescence spectrometry (XRF) 37
3.2.6 X-ray diffraction (XRD) 38
3.2.7 Thermogravimetric analysis (TGA) 40
3.2.8 Scanning electron microscope (SEM) 41
3.2.9 Compressive fracture strength test 41
3.3 HPHT diamond synthesis components preparation 44
3.3.1 Magnesia seedpads and alumina seedpads preparation 44
3.3.2 Graphite with metal solvents (GMS) slugs 45
3.4 Characterisation of seedpad compacts, GMS granules and GMS slugs 47
3.4.1 The density of fired compacts 47
3.4.2 Inductively coupled plasma spectrometry (ICP) 47
3.4.3 Oxygen and carbon analysis 47
3.5 High pressure high temperature (HPHT) diamond synthesis 48
3.5.1 Capsule design for HPHT synthesis 48

3.6 Characterisation of HPHT synthesised capsule 50
Chapter 4: Experimental Results 52
4.1 Characterisation of raw magnesia (Nedmag) and raw alumina (KSM99) powders 52
4.2 Magnesia and alumina powders moisture absorption test 54
4.3 Characterisation of spray dried magnesia and spray dried alumina powders 56
4.3.1 PSD, LOI, moisture and density of powders results 57
4.3.2 Powder particle morphology 58
4.3.3 XRD and XRF powder results 59
4.4 Manufacture of magnesia seedpads and alumina seedpads compacts 61
4.5 Compressive fracture strength test for magnesia and alumina 63
4.6 Manufacture of GMS slugs 68
4.7 HPHT Diamond synthesis results 70
4.7.1 Cubic synthesis test using seedpads without diamond seeds 71
4.7.2 SEM-EDS profile of seedpads and GMS slugs 73
4.7.3 Diamond synthesis at HPHT 77
Chapter 5: Discussion 79
5.1 Moisture absorption by magnesia and alumina ceramics 79
5.2 Components manufacture 80
5.3 Mechanical behaviour and properties of seedpads 82
5.4 Diamond synthesis 84
Chapter 6: Conclusion 85
References 86
Appendicies 93
Appendix A Characterisation of powders 93
Appendix B Components manufacturing 97
Appendix C Mechanical behaviour of materials 99

Appendix D Synthesis 102

List of Figures

Figure 1 A sketch showing a seedpad used for HPHT diamond synthesis. 1
Figure 2 The structure of (a) graphite and (b) diamond [10]. 4
Figure 3 The carbon phase diagram [18]. 7
Figure 4 Proposed reaction mechanism in the synthetic diamond formation using iron as a metal solvent [21]. 9
Figure 5 Schematic drawing of a cubo-octahedral synthetic diamond in an exposed surface of a reaction cell [21]. 10
Figure 6 Pressure temperature diagram for diamond synthesis showing typical conditions (P_1, T_1) [8]. 10
Figure 7 Schematic drawing of (a) belt press apparatus (b) cubic press apparatus [22], [25]. 11
Figure 8 Cubic capsule cell assembly used in anvil self-formed gasket system for HPHT cubic press diamond synthesis [26]. 12
Figure 9 High pressure synthesis cell used to grow reconstituted diamond [21]. 12
Figure 10 Colourless inclusion on the surface of an octahedral diamond [2]. 13
Figure 11 Al-C-O Phase Diagram (1995 Caian Qiu) – Calculated [28]. 14
Figure 12 Al-Fe-O Phase Diagram (1993 Eriksson G.) – Theoretical [28]..... 14
Figure 13 Al-Ni-O Phase Diagram (1993 Kuznetsov V.) – Experimental [28]..... 15
Figure 14 The crystal structure of magnesia [33]. 16
Figure 15 (a) Crystal structure of α alumina (b) top view (c) octahedral structure [34]. 17
Figure 16 The alumina phases (α, δ, ǿ, Ƙ, ɣ) and the transition stages at different temperatures [34]. 17
Figure 17 Density versus compaction pressure of alumina powder compaction [35]. 20
Figure 18 Density distribution in the upper half of a dry pressed cylinder [39]. 20
Figure 19 Sintering of the powder particles [36]. 22
Figure 20 Conventional and true stress strain diagram for ductile material (steel) not to scale [46]. 24
Figure 21 Tensile and compressive engineering stress strain curve for grey cast iron and concrete [48]. 25
Figure 22 (a) Internal cracks geometry and (b) a schematic stress profile along the x – x’ [50]..... 27

Figure 23 Total flaw distribution and largest flaw distribution in a material [51]. 29
Figure 24 Three types of distribution offset along the x-axis for easier comparison, where x is the flaw size [51]. 29
Figure 25 Graphical presentation for determining m and σ [52]. 31
Figure 26 An illustration of an atom showing energy levels K, L, M and N [63]. 38
Figure 27 X-ray 1 and 2 diffraction [65]. 39
Figure 28 Instron test rig model 1175. 42
Figure 29 Illustration of peeling and splitting compared to intact ends [70]. 42
Figure 30 Drawing and specifications of samples prepared for compression test [70]. 44
Figure 31 Firing profile cycle for magnesia and alumina seedpads compacts and GMS slugs. 45
Figure 32 Flow diagram used for manufacturing of GMS slugs. 46
Figure 33 (a) cubic diamond seeds, Seedpads compacts with embedded diamond seeds assembly for (b) magnesia seedpad and (c) alumina seedpad. 49
Figure 34 An illustration section view showing the arrangement of seeded magnesia or alumina seedpad and GMS slugs in a capsule. 49
Figure 35 (a) 41 mm cubic capsule components (b) assembled and closed cubic capsule showing outer envelope and a thumbtack metal casing. 50
Figure 36 Particle size distribution of magnesia (Nedmag) and alumina (KSM99) powders from Malvern Mastersizer 2000 analyser. 53
Figure 37 SEM-EDS for (a) magnesia (Nedmag) and (b) alumina (KSM99) powders. 54
Figure 38 Moisture absorption results for magnesia (Nedmag) and alumina (KSM99). 55
Figure 39 TGA graphs for magnesia (Nedmag) and alumina (KSM99) in synthetic air and nitrogen. 56
Figure 40 Particle size distribution of spray dried magnesia and spray dried alumina. 58
Figure 41 SEM images of (a) spray dried magnesia powder and (b) spray dried alumina powder. 59
Figure 42 XRD for spray dried magnesia powder. 60
Figure 43 XRD for spray dried alumina powder. 60

Figure 44 Density vs pressure of fired magnesia seedpads compacts and alumina seedpads compacts. 62
Figure 45 XRD for fired magnesia seedpad compacts. 62
Figure 46 XRD for fired alumina seedpad compacts. 63
Figure 47 Test sample under the Instron test rig. 64
Figure 48 Fractured samples of (a) magnesia compact and (b) alumina compact. .. 64
Figure 49 Magnesia compacts compressive stress-strain graph. 65
Figure 50 Alumina compacts compressive stress-strain graph. 65
Figure 51 Compressive fracture strength of magnesia and alumina compacts box plot. 66
Figure 52 % density of magnesia compacts and alumina compacts. 66
Figure 53 Weibull parameter determination graph. 67
Figure 54 GMS granule particles used for uniaxial pressing GMS slugs. 68
Figure 55 SEM-EDS of a GMS solvent granule surface showing graphite and metal solvents distribution. 69
Figure 56 Pressed cubic capsule showing self-extruded gasket and metal casing disc from a thumbtack. 72
Figure 57 (a) and (c) alumina seedpad before and after HTHP synthesis, (b) and (d) magnesia seedpad before and after HPHT synthesis. 73
Figure 58 SEM images of (a) GMS slug for magnesia seedpad, (c) magnesia seedpad, (b) GMS slug for alumina seedpad, (d) alumina seedpad after HPHT synthesis. 74
Figure 59 % weight concentration of magnesia and alumina through the GMS slugs and through the magnesia seedpad or alumina seedpad interface. 75
Figure 60 % weight concentration of iron through the GMS and magnesia seedpad or alumina seedpad interface. 76
Figure 61 % weight concentration of nickel through GMS slugs and magnesia seedpads or alumina seedpad interface 76
Figure 62 Diamond synthesised from (a) magnesia seedpads (b) alumina seedpads. 77
Figure 63 Section of GMS slug and solvent metal film region surrounding the synthesised diamond 78
Figure 64 TGA graphs for magnesia (Nedmag) and alumina (KSM99) powders. 80

Figure 65 Cumulative particle size distribution of spray dried magnesia and spray dried alumina powders. 81
Figure 66 SEM image of alumina spray dried particles with some voids. 83
Figure A1 (a) magnesia (Nedmag) (b) alumina (KSM99) powder particle size distribution (before spray drying). 93
Figure A2 XRF results of spray dried alumina. 94
Figure A3 XRF results of spray dried magnesia. 96

List of Tables

Table 1 The crystal structures of diamond and graphite [12]..... 5
Table 2 Properties of diamond and graphite [12]. 6
Table 3 Properties of magnesia and alumina [27]. 18
Table 4 Advantages and limitations of uniaxial pressing [41]. 21
Table 5 Magnesia (Nedmag) and alumina (KSM99) powder specifications [53][54]. 33
Table 6 Carr index and Hausner Ratio for powder flow character [60] 37
Table 7 Results from Malvern comparing Nedmag and KSM99. 52
Table 8 Moisture absorption test results, measured using LOI (wt %) 55
Table 9 Spray dried magnesia and spray dried alumina powders characterisation.. 57
Table 10 (a) spray dried magnesia and (b) spray dried alumina XRF results. 61
Table 11 Summary of magnesia and alumina fracture strength results. 68
Table 12 Results of green GMS slugs. 70
Table 13 Results of fired GMS slugs. 70
Table 14 Magnesia seedpad capsule and alumina seedpad capsule. 71
Table 15 Cubic press feedback results for HPHT synthesis. 71
Table 16 % LOI per surface area of the particle. 79
Table 17 Pressed results of (a) green magnesia seedpads (b) alumina seedpads.. 97
Table 18 Fired compacts results of (a) magnesia seedpads (b) alumina seedpads. 98
Table 19 Magnesia compacts results. 99
Table 20 Alumina compacts results..... 100
Table 21 Weibull analysis..... 101
Table 22 Composition of various elements at seedpads and graphite with metal solvents interface. 102

List of Abbreviations and Symbols

Al_2O_3 = Aluminium oxide

MgO = Magnesium oxide

PVA = polyvinyl alcohol

PEG = poly ethyl glycol

SEM = Scanning Electron microscope

EDS = Electron dispersive spectrometer

XRD = X-ray diffraction

XRF = X-ray fluorescence

ICP = Inductive coupled plasma

TGA = Thermogravimetric analysis

LOI = Loss on Ignition

HPHT = High pressure high temperature

GMS = Graphite with metal solvent

Chapter 1: Introduction

The widespread selection and use of ceramic materials in a plethora of applications can be ascribed to their superior properties. Modern industrial technology is always seeking better performing ceramic materials for new and existing applications, be they structural or functional. Ceramic components are utilised in high pressure high temperature (HPHT) diamond synthesis by Element Six Pty Ltd as thermal insulators, electrical insulators and synthesis press gaskets. Magnesia finds a use for making ceramic cups and seedpads compacts. A seedpad is a disc compact made from spray dried magnesia powder, carrying diamond seeds embedded onto one of disc's side at a defined orientation and spatial arrangement as shown in Figure 1. The diamond seeds grow in a diamond synthesis press at high temperature (1450 ^{o}C) and pressure (5 GPa) in the presence of a carbon source, graphite, with metal solvents Fe, Co and Ni as catalysts (GMS).

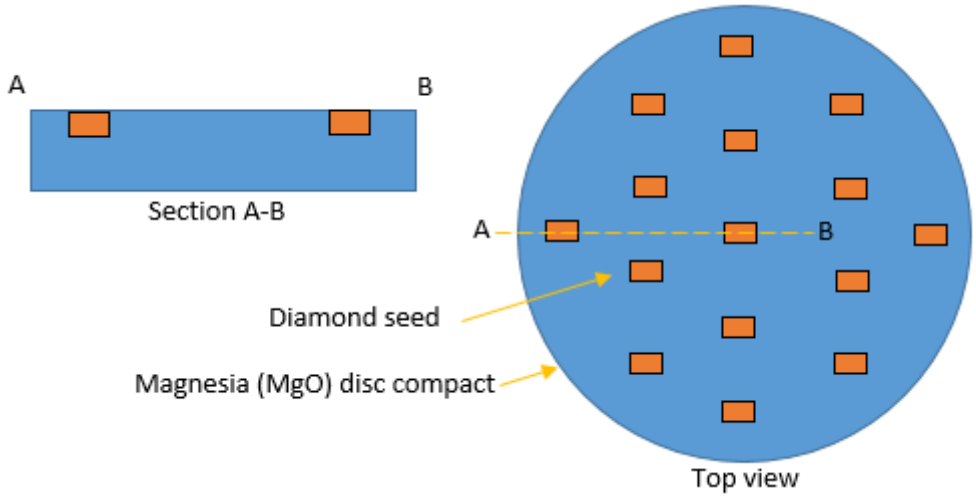

Figure 1 A sketch showing a seedpad used for HPHT diamond synthesis.

Magnesia seedpads have brought the following instability to HPHT diamond synthesis (i) spray dried magnesia source Nedmag, obtained from Nedmag Industries in the Netherlands, has a purity of 98.5% MgO, the remainder accounts for impurities, Fe_2O_3, CaO, SiO_2 and B_2O_3. MgO and CaO react with moisture from the atmosphere to form hydroxides, calcium hydroxide further absorbs carbon dioxide from the air to form

carbonates [1]. Hydroxides and carbonates decompose during HPHT synthesis resulting in diamond growth instability. Silica and boron oxide contaminate diamonds during crystal growth by forming inclusions that appear as dark spots in the diamond crystal structure [2]. Element Six Pty Ltd has invested in pre-treatment of seedpads in a vacuum furnace at 1140 ^{o}C to remove moisture and decompose impurities. Moisture re-absorption is prevented by storing seedpads under a nitrogen cabinet prior to use at HPHT synthesis presses. Seedpad material stability and its purity in HPHT diamond synthesis conditions is key to successful diamond synthesis.

The purpose of this study is to explore the suitability of a sourced spray dried alumina powder for manufacturing seedpad compacts of comparable geometry, density and strength to current magnesia seedpads and test alumina seedpads in HPHT diamond synthesis, as a replacement for magnesia seedpads. Alumina seedpads, like magnesia seedpads, should have sufficient strength to hold diamond seeds during pre-synthesis handling processes and at initial HPHT press compacting to prevent distorting pre-defined diamond seeds arrangement and spacing. Insufficient seedpads strength may lead to diamond seeds losing spacing and orientation, this may result in unequal graphite diffusion into growing seeds and results in wrong diamond growth directions. Spray dried alumina powder was obtained from Albemarle GmbH, Germany, spray dried from its pure grade alumina, KSM99. Alumina is known for its stability in the presence of moisture and carbon dioxide [1], alumina seedpad material might possibly address stability problems currently being faced. Alumina finds application in mechanical systems due to its high hardness, high moduli of elasticity and satisfactory mechanical strength [3]. Alumina has excellent compressive strength and has a good creep resistance due to its stability at high temperature [4]. Compression comparison tests on magnesia compacts and alumina compacts were conducted using the Instron test rig, Weibull analysis was used to compare and predict the fracture strength performance and hence mechanical stability of the two materials under compression.

Alumina is used in many ceramic industrial applications and for production of metallic aluminium. There is a steady supply of magnesia and alumina worldwide, but the

demand for alumina and aluminium remain high. Aluminium metal recyclability provides an added advantage for long term conservation of alumina reserves. Despite its world economic demand, alumina has maintained its stable prices over the years [5], [6]. The global availability of alumina remains high with its ore bauxite mining still being done through cheaper open cast mining [7].

Chapter 2 gives a detailed overview of the literature on magnesia and alumina availability, properties and crystallography. Manufacture of seedpads through uniaxial compaction and firing to make seedpads compacts with sufficient strength is described. The literature overview of graphite with metal solvent slugs (GMS) used as a carbon source for diamond growth is also described in that chapter.

Chapter 3 gives a detailed report on the methodology used to compare the properties of magnesia and alumina, as powders. The ceramics firing and sintering process are described, followed by characterization of the derived compacts and subsequently of their behaviours during the diamond synthesis process.

Chapter 4 summarises the results from the powder characterisation and experiments conducted to compare magnesia seedpads and alumina seedpads in the HPHT diamond synthesis. The chapter describes experimental results to compare and predict the compressive fracture strength of magnesia and alumina compacts and the use of Weibull statistics to evaluate compressive fracture strength results. The stability of these two seedpads in the presence of GMS slugs was evaluated by Scanning Electron Microscope (SEM) and Electron Dispersive Spectroscopy (EDS) profile. The synthesised diamonds from magnesia and alumina seedpads were evaluated and compared. Chapter 5 gives the discussion of results for magnesia and alumina usage following HPHT diamond synthesis. Lastly, Chapter 6 gives the conclusions resulting from this work. The Appendix provides additional information for the dissertation

Chapter 2: Literature Review

2.1 Synthetic diamond

Several attempts have been made to crystallise diamond from various carbonaceous starting materials. The first clear success was by Swedish group ASEA in February 1953, General Electric followed in December 1954 [8]. Today, 90% of industrial diamonds produced in the world are synthetic diamonds. Diamonds find extensive use in industry as abrasive, in surgery, in astronomy, in experimental physics and electronics [9]. Diamond and graphite are both allotropes of carbon, the sixth element in the periodic table of elements. The structures of diamond and graphite are shown in Fig 2 (a) and (b).

2.1.1 The crystallography of graphite and diamond

Graphite exists in arrays of layered sheets, as shown in Figure 2 (a), the carbon atom is covalently bonded to three other carbon atoms neighbouring, leaving the fourth electron free and delocalised within a sheet. Carbon atoms in diamond are bonded to four other carbon atoms by a single covalent bond forming a tetrahedral structure, as shown in Figure 2 (b) [10].

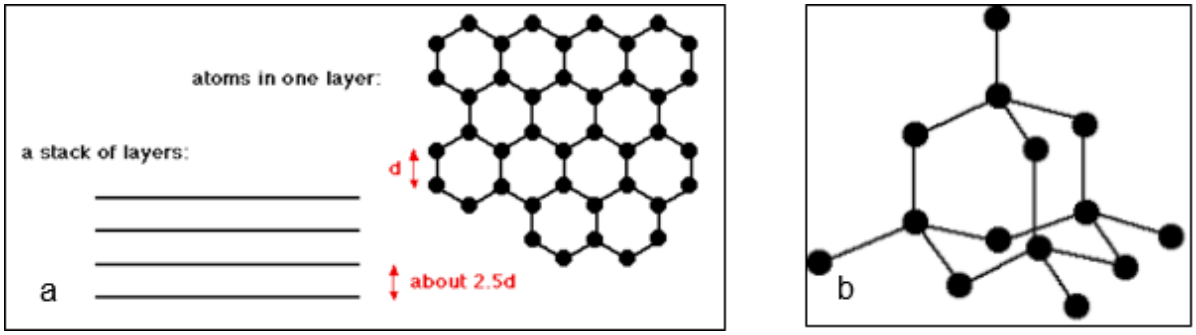

Figure 2 The structure of (a) graphite and (b) diamond [10].

The diamond structure has four valence electrons in the s and p orbitals that combine to form sp^3 bonds through hybridisation. The four valence electrons are equally

distributed in the sp^3 orbital, making each orbital to point towards the four corners of the tetrahedral. All bonds in diamond have a length of 1.54 Å and a bond angle of 109.47°. The graphite structure, s orbital combines with 2p orbital to form the sp^2 orbital. The sp^2 orbital has a Px and Py planer orbital and a δ bond at an angle of 120° perpendicular to Pz orbital forming a π bond [11]. The crystal structures of graphite and diamond are summarised in Table 1. The cubic faces {100} do not occur in natural diamond and the most common synthetic diamond is the cubo-octahedral with almost equal areas of {100} and {111} faces.

Table 1 The crystal structures of diamond and graphite [12].

Structure	Diamond	Graphite
Carbon bonding	Covalent sp^3	Covalent sp^2, van der Waals
Crystalline form	Cubic, hexagonal	Hexagonal, rhombohedral
Crystalline Lattice Parameter, nm	Cubic, 0.3567	Hexagonal, a_0 = 0.246, c_0 = 0.6708
Common crystal face	{111}, {011}, {001}	{0001}, {10$\bar{1}$0}, {10$\bar{1}$1}, {$\bar{1}$012}
Cleavage and slip plane	{111}	{0001}

2.1.2 Physical properties of graphite and diamond

The strong carbon-carbon bonds make diamond and graphite high melting and high boiling point materials. Graphite's slippery feel is due to layered sheets sliding over each other, a property that makes graphite softer. The presence of delocalised electrons in graphite allows it to conduct electricity. Graphite density is lower than that of diamond due to some empty spaces in-between layered sheets [10], [11]. The combination of strong directional covalent bonds without slip planes and the high density of these bonds in the diamond structure are responsible for the high hardness, the desired property for its application in stone and non-ferrous alloy cutting and machining, polishing and oil and gas drilling. Diamond has a thermal conductivity higher (five times that of copper) than any other solid material at room temperature. It

is the ideal material for transmission of light from infrared to ultraviolet and has an unusually high refractive index. Diamond has the highest atomic packing of any material, because of its strong bonds, and a molar density of 0.293 g-atom/cm^3. This property makes diamond the stiffest, hardest and least compressible of all substances [13]. Table 2 summarises properties of graphite and diamond.

Table 2 Properties of diamond and graphite [12].

Property	Diamond	Graphite
Density (g/cm^3)	3.52	2.26
Young's modulus, GPa	910 – 1250	Single Crystal: 1060 (a direction) 36.5 (c direction) Pyrolitic graphite, 28 – 31 Molded graphite, 5 – 10
Compression strength GPa	8.68 – 16.53	0.065 – 0.089
Specific heat at 25°C, kJ/kgK	0.502 – 0.519	0.690 – 0.719

2.1.3 Synthesis of diamond

Synthesis of diamonds is broadly categorised under the following methods (i) Catalysed synthesis: carbon and metal catalysts are heated to a high temperature until graphite dissolves in molten metal, the pressure is applied until the system reaches a diamond stable region where the diamond is formed (High Pressure High Temperature (HPHT) catalysed diamond synthesis) [14]. (ii) Shock synthesis: highly compressed graphite is subjected to heat produced by an explosive, diamond is formed [15]. (iii) Static pressure synthesis: graphite forms diamond directly at pressures of 13 GPa and temperature of 3000 K to 4000 K [16]. (iv) Chemical Vapour Deposition (CVD): carbon from a vapour state is deposited onto a diamond seed crystals at a low pressure where

the diamond is thermodynamically unstable with respect to graphite. The mobility of carbon atoms on a clean crystal at 1000 ^{o}C is high enough to make them become attach them to the existing lattice [17].

2.1.4 High Pressure High Temperature (HPHT) diamond synthesis

HPHT diamond synthesis from graphite at elevated temperature and pressure follows a phase diagram shown in Figure 3, intermediate phases occur, (i) graphite and metastable diamond, chaoite, at lower pressure and (ii) metastable graphite with the diamond, carbine, at higher pressure. It is noted that at a lower pressure than diamond formation in a phase diagram, heated graphite can sublimate to form a vapour, however, at elevated temperature and pressure, graphite liquid is formed [18].

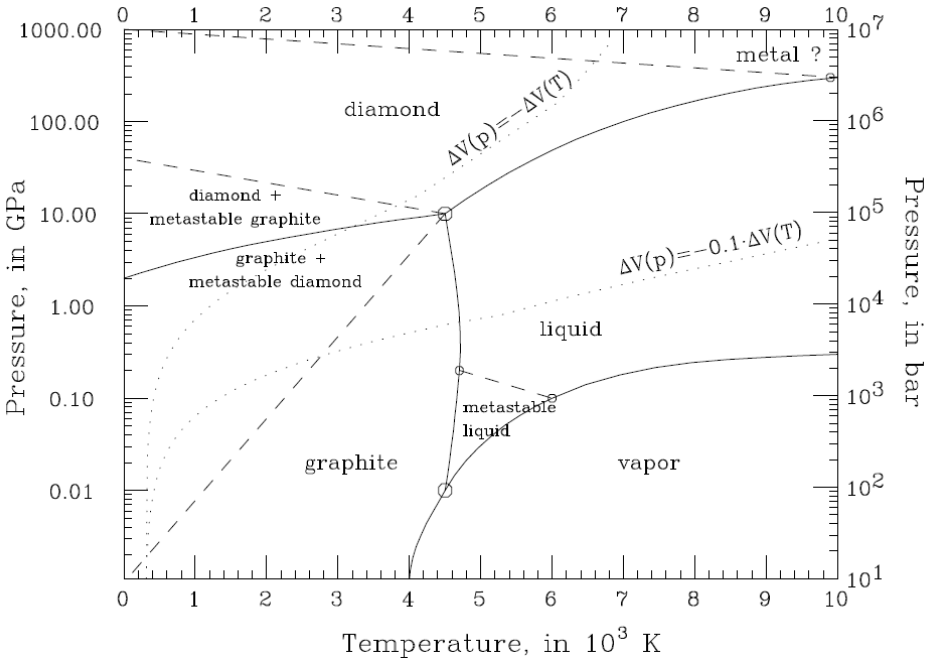

Figure 3 The carbon phase diagram [18].

The formation of the diamond from graphite follows a phase change described by Equation 1, the positive Gibbs free energy of formation shows that graphite is more stable than diamond at all temperatures at atmospheric pressure.

$$\mathrm{C(graphite)} \longrightarrow \mathrm{C(diamond)},\ \Delta G = +2.9\mathrm{kJ/mol} \qquad \text{Equation 1}$$

Diamond is denser than graphite, increasing pressure favours the formation of the diamond. The graphite-diamond equilibrium from the system is achieved between two phases when Gibbs free energy change at temperature T and pressure P is zero. The change of Gibbs free energy, $\Delta G^{o}_{P,T}$ is given by Equation 2.

$$\Delta G^{o}_{P,T} - \Delta G^{o}_{1,T} = \int_{1}^{P} \Delta V_R \, dP \qquad \text{Equation 2}$$

$\Delta G^{o}_{1,T}$ = Gibbs free energy at pressure 1 bar and temperature T,

ΔV_R = Volume change

At high pressure and temperature, the volume change is a function of T and P and cannot be assumed constant. An expression for a volume change is needed to complete integration from Equation 2, and can be simplified and obtained from Equation 3 [19], [50].

$$dV = \alpha V dT - \beta V dP \qquad \text{Equation 3}$$

α = coefficient of thermal expansion,

β = isothermal coefficient of compression,

Metal solvents are used for catalysing diamond synthesis, metals of group VIII on the periodic table are more effective solvents, other metals such as manganese, chromium, tantalum and niobium can also be used as solvents [21]. Non-metallic solvents have also been used as catalysts for diamond growth such as carbonates (Na_2CO_3 and $CaCO_3$), phosphates, borates, [22], [23] and Mg-Si-C solvents [24]. The utilisation of metal solvents in diamond synthesis relies on the stability of carbide formation, the solubility of carbon in the metal and surface wetting characteristics (surface energy) with graphite. Putyatin et al. (1989), Figure 4 have shown in detail iron-carbon systems reaction mechanisms at the temperature range of 900 K – 2000 K and a pressure range of 4 GPa – 8 GPa. The wetting angle of a molten metal solvent in contact with graphite at high pressure is lower than the wetting angle at atmospheric

pressure, this indicates a stronger interaction of graphite with the metal at high pressure than at atmospheric pressure.

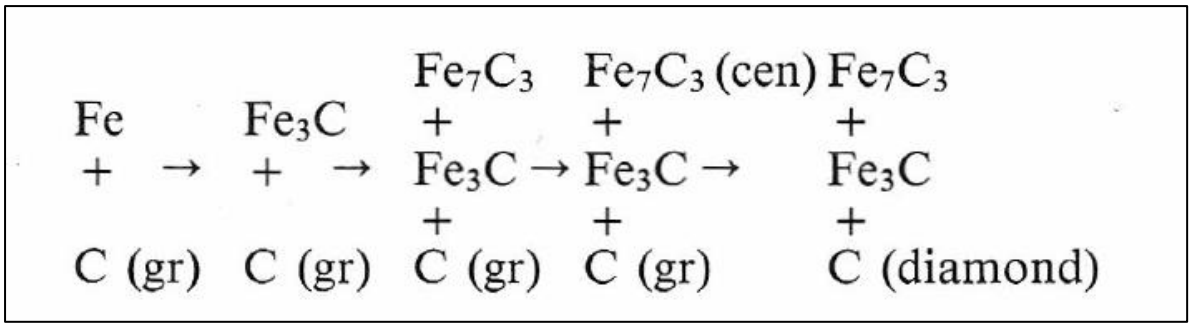

Figure 4 Proposed reaction mechanism in the synthetic diamond formation using iron as a metal solvent [21].

Nickel carbide is also formed at high temperatures to facilitate diamond formation in a similar manner as is the case for iron. Suitable catalyst choice is determined by work of adhesion between carbon and metal equivalent to about 84 – 126 kJ/mole [21], this corresponds to activation energy for diamond synthesis from graphite. Metals such as palladium, nickel, cobalt and iron which have work of adhesion of 90 – 110 kJ/mol are suitable for catalysis [21]. Other metals such as copper with lower values and are unsuitable for use as a catalyst. Most producers of synthetic diamonds favour binary catalyst combinations. USA General Electric uses iron-nickel, Element Six cobalt- iron. A good and a bad carbide former are utilised in these combinations. Nickel and cobalt are bad carbide formers whilst manganese and iron are good carbide formers. A carbide former is an intermediate combination of carbon and metal solvent in the diamond synthesis process. The combination of a bad and good carbide formers assist in the control and stabilisation of an intermediate metal solvent – carbide eutectic and this forms low melting point alloy combination [21]. The metal phase near diamond is shown in Figure 5 corresponds to initial alloy composition, this is because the carbon content in the metal film near diamond is reduced due to the diffusion of graphite onto the diamond surface during crystal growth. The diffusion of graphite through metal surrounding diamond is the rate determining step [21].

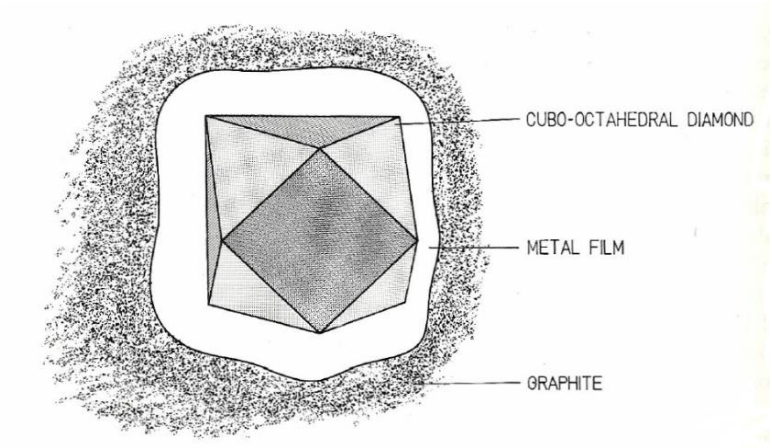

Figure 5 Schematic drawing of a cubo-octahedral synthetic diamond in an exposed surface of a reaction cell [21].

The final morphology of synthetic diamond provides clues on thermodynamics, chemical conditions and changes of these variables during diamond growth. The increase of temperature at elevated synthesis pressure favours a change of cubic to octahedral morphology, as shown in Figure 6.

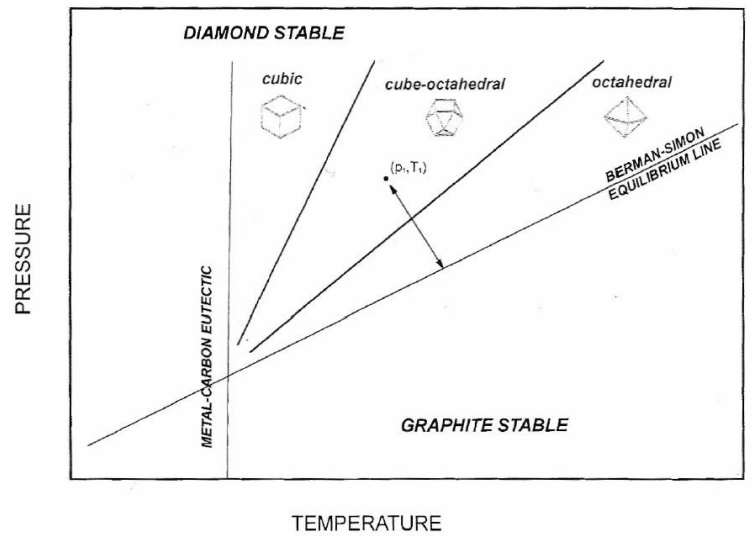

Figure 6 Pressure temperature diagram for diamond synthesis showing typical conditions (P_1, T_1) [8].

Special apparatus must be used to generate high pressure and high temperature required to grow diamond greater than 5 GPa and 1400 ^{o}C, respectively. Belt press apparatus consists of a central die and top and bottom punch made of sintered tungsten carbide cobalt shown in Figure 7 (a) [22]. Cubic press apparatus consists of six anvils, shown in Figure 7 (b), mounted on six pistons simultaneously pushed towards a pyrophyllite cubic envelope by computerised rams [25]. Other apparatus used are multi anvil type tetra, and octahedral shaped presses containing a sample and a heater with four, six and eight anvils respectively.

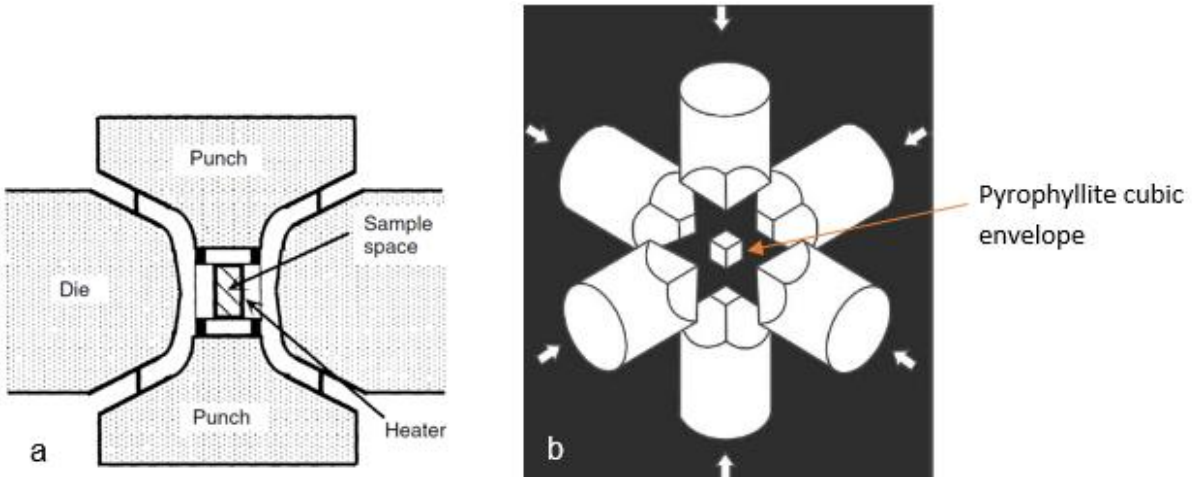

Figure 7 Schematic drawing of (a) belt press apparatus (b) cubic press apparatus [22], [25].

The centre of the cubic press is a cavity for pyrophyllite cubic envelope, the pressure builds up from compressing anvils on a pyrophyllite cube results in a self-formed extrusion gasket shown in Figure 8 [26].

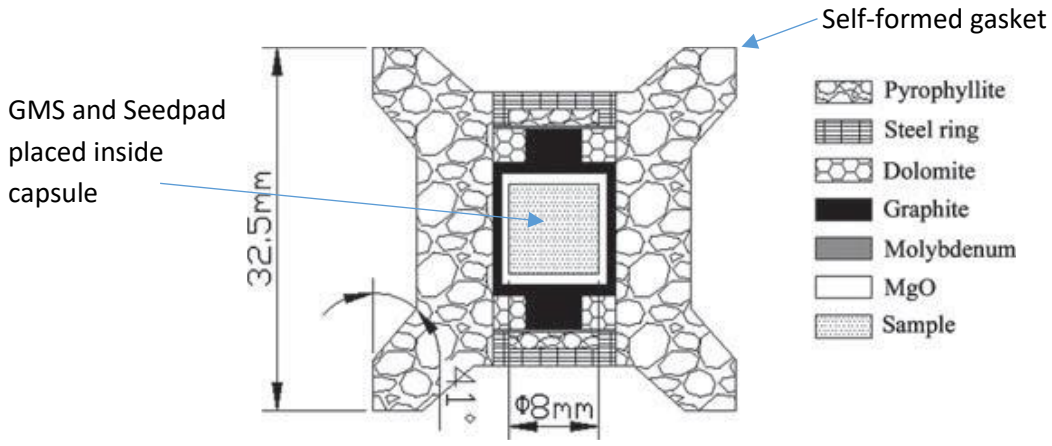

Figure 8 Cubic capsule cell assembly used in anvil self-formed gasket system for HPHT cubic press diamond synthesis [26].

The high pressure cell with a seedpad and metal solvent/catalyst shown in Figure 9 is placed inside a cubic envelope for diamond synthesis. Reconstituted diamonds are grown from a diffusion diamond source (graphite) in the presence of solvent/catalyst at elevated high pressure and high temperature [21].

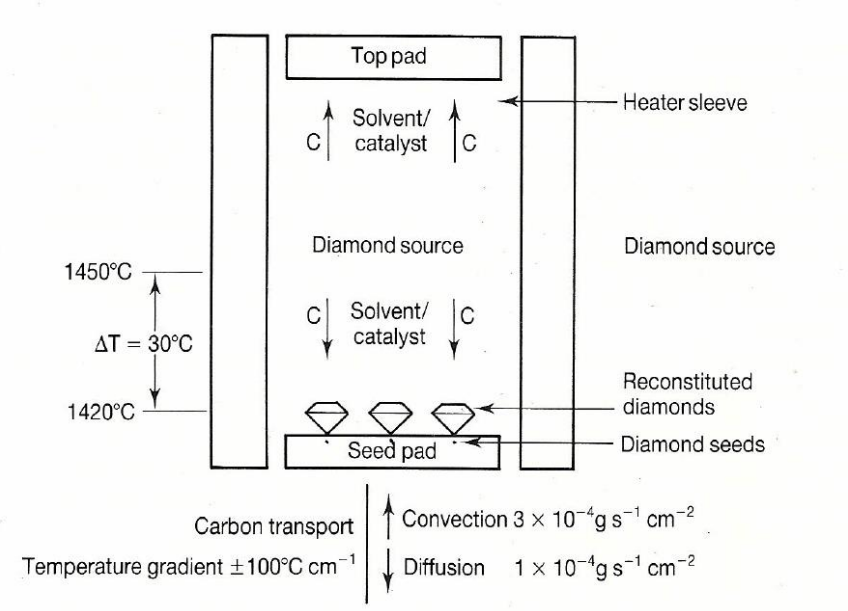

Figure 9 High pressure synthesis cell used to grow reconstituted diamond [21].

A seedpad must be in solid phase during HPHT diamond synthesis cycle to hold diamond seed crystals at set orientation and spatial arrangement facing and in contact with solvent/catalyst metals. Distortion to diamond seed crystals orientation may lead to poor shape due to wrong crystal face directional growth and poor seeds spacing may affect the diffusion of graphite. Distorted seeds with closer proximity to each other may deplete surrounding graphite faster leading to the distorted final shape of grown diamonds. The presence of impurities in the magnesia seedpad material currently used by Element Six Pty Ltd may contaminate diamonds during diamond growth by forming inclusions such as shown in Figure 10. Ambient air moisture absorption by magnesia destabilises diamond growth. Magnesia, currently used as seedpad material, has a melting point of 3080 ^{o}C [27], hence during diamond synthesis temperature, magnesia retains its solid phase. Exploring alumina, as a seedpad material, should also retain the solid phase during the HPHT diamond synthesis because alumina melts at 2046 ^{o}C [27].

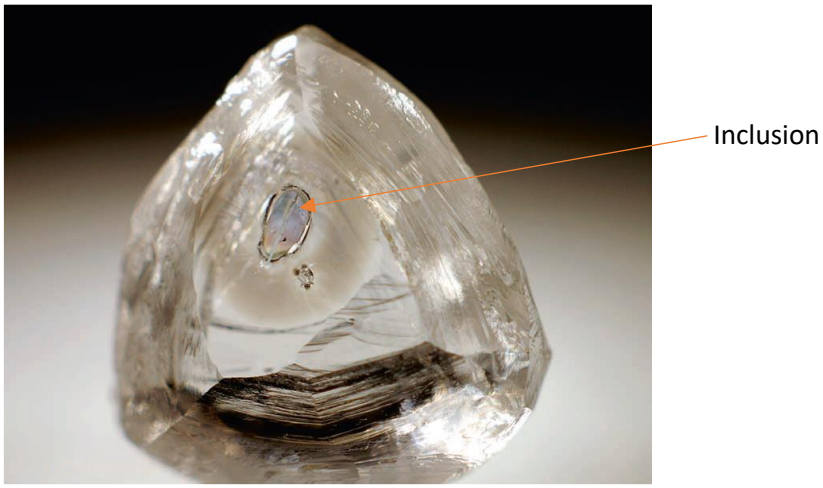

Figure 10 Colourless inclusion on the surface of an octahedral diamond [2].

The stability of alumina seedpad material in contact with graphite can be predicted from the phase diagram in Figure 11. At a lower carbon content in the alumina region, melting occurs at temperatures between 1850 ^{o}C to 2049 ^{o}C, and this is greater than diamond synthesis temperature of 1420 ^{o}C.

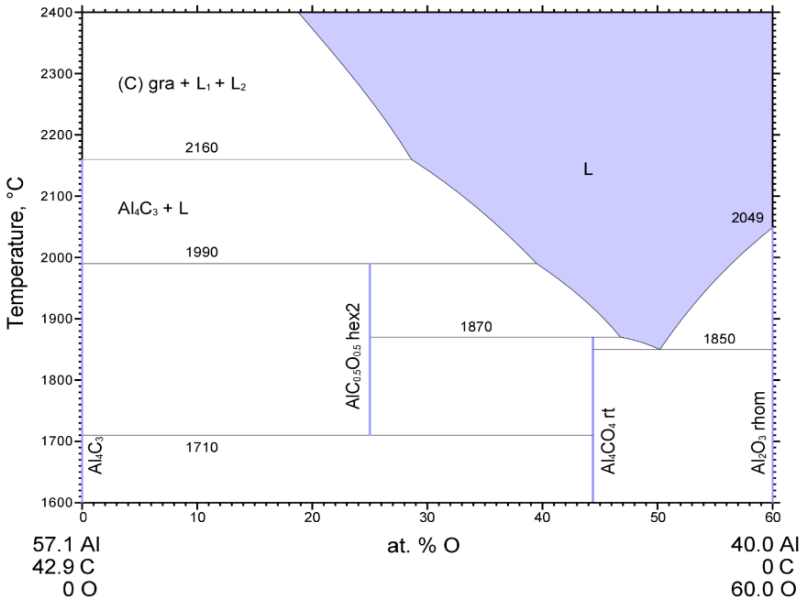

Figure 11 Al-C-O Phase Diagram (1995 Caian Qiu) – Calculated [28].

Solvent metal Iron, from GMS slugs, was expected to diffuse negligible into the alumina seedpad material at HPHT diamond synthesis, the stability of iron-alumina relation is predicted from the phase diagram in Figure 12.

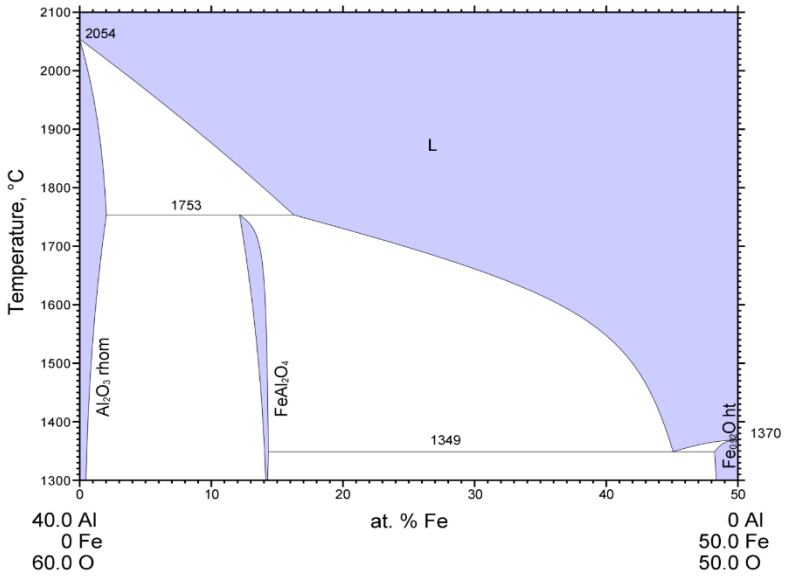

Figure 12 Al-Fe-O Phase Diagram (1993 Eriksson G.) – Theoretical [28].

Solvent metal nickel, from GMS slugs, was expected to diffuse negligible into the alumina seedpad at HPHT, the stability of nickel-alumina is predicted from the phase diagram in Figure 13.

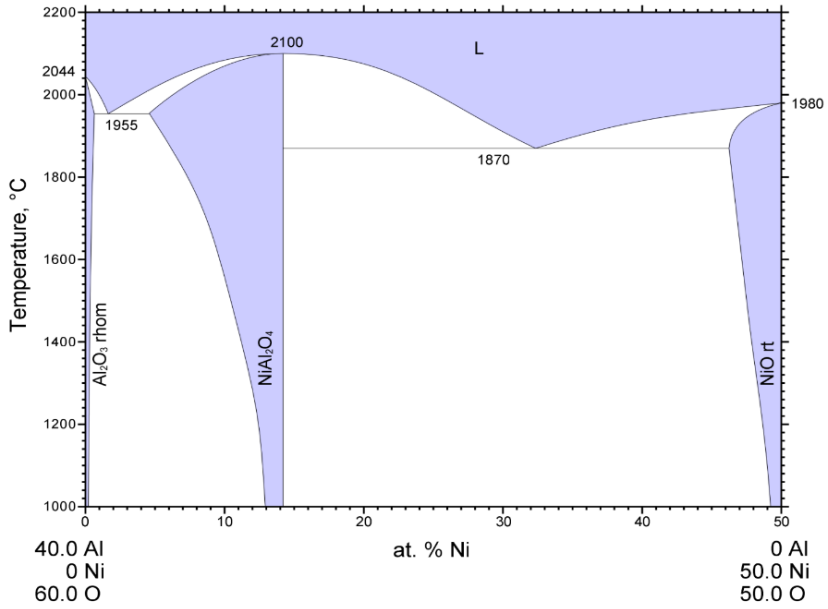

Figure 13 Al-Ni-O Phase Diagram (1993 Kuznetsov V.) – Experimental [28].

A study to understand the properties of alumina and magnesia in preparation for making alumina seedpads was conducted. The two material properties were compared with the aim of exploring alumina properties to make a seedpad of similar geometry and density to current magnesia seedpad used by Element Six Pty Ltd.

2.2 Alumina and magnesia

Magnesia occurs naturally in sulphates, carbonates, chlorides and hydrated oxides in simple or complex salts. The magnesia containing main ores include magnesite $MgCO_3$, brucite $Mg(OH)_2$, dolomite $CaMg(CO_3)_2$, bischofite $MgCl_2.6H_2O$ and seawater [29]. Alumina occurs naturally in the mineral ores corundum (Al_2O_3), diaspore AlO(OH), gibbsite $Al(OH)_3$ and bauxite (mixed gibbsite, boehmite (γ-AlO(OH) and diaspore). The mineral commonly found in nature is bauxite with purity ranging

between 35 % – 55 % alumina, impurities include silica, haematite and TiO_2 [30]. The minerals ruby and sapphire are forms of corundum, their colour is attributable to small impurities found in the mineral. Other forms of alumina minerals are bayerite, and nordstrandite [31].

2.2.1 Crystallography and phases of magnesia and alumina

Magnesia, MgO, is a ceramic oxide formed by the bonding of the cation Mg^{2+} with the anion, O^{2-}, in a cubic structure, as shown in Figure 14. Magnesia has a high melting point and has a stable phase at high pressure and high temperature [32].

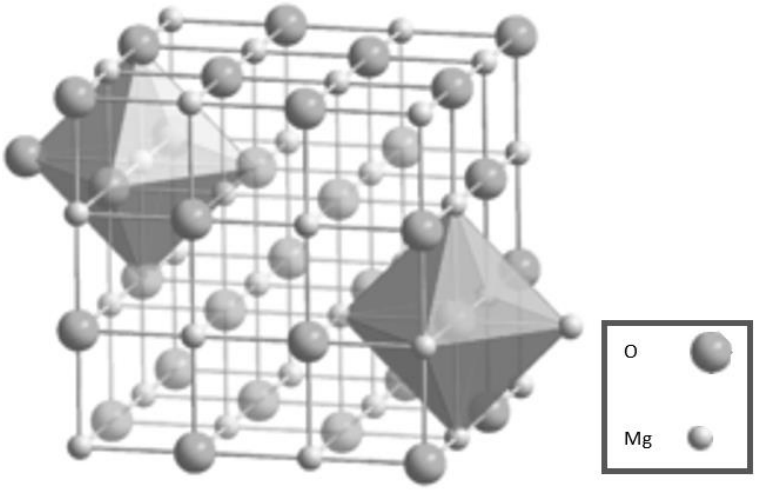

Figure 14 The crystal structure of magnesia [33].

Alumina, Al_2O_3, is a ceramic oxide formed when the cation, Al^{3+}, bonds with the anion, O^{2-}, in an octahedral structure. Aluminium cations occupy planes A and B, two thirds of the basic array structure in hexagonal sites shown in Figure 15 [34].

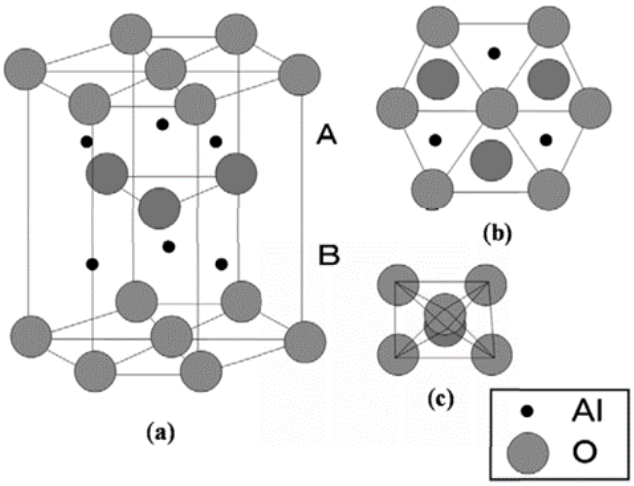

Figure 15 (a) Crystal structure of α alumina (b) top view (c) octahedral structure [34].

The basic unit cell of corundum is hexagonal, existing as different phases shown in Figure 16, (α, δ, ǿ, Ƙ, ɣ). The α phase is thermodynamically stable at high temperatures, other phases transform to the α phase at high temperatures. The α phase form is metastable and does not transform back into other phases upon cooling [4].

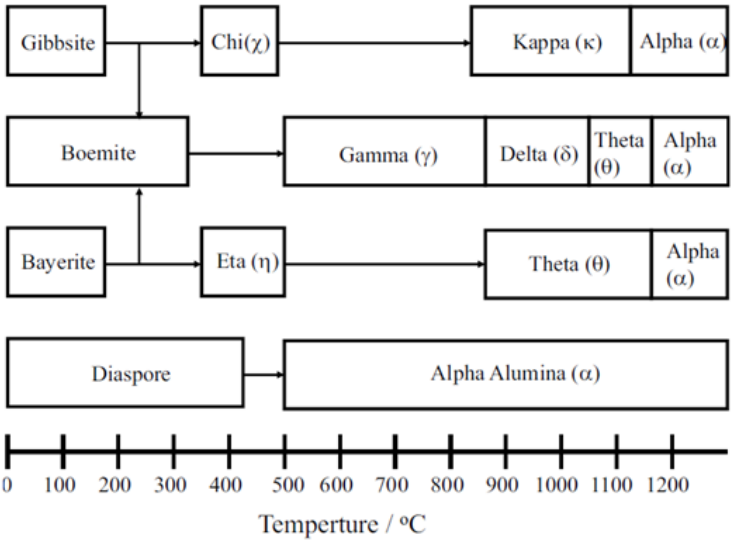

Figure 16 The alumina phases (α, δ, ǿ, Ƙ, ɣ) and the transition stages at different temperatures [34].

2.2.2 Physical and mechanical properties of magnesia and alumina

Magnesia and alumina are hard materials making them suitable for certain ceramic applications, their physical and mechanical properties are summarised in Table 3. Alumina has a higher density, a superior compressive strength and has twice fracture toughness than magnesia.

Table 3 Properties of magnesia and alumina [27].

Property	**Magnesia**		**Alumina**		
	Min	**Max**	**Min**	**Max**	**Units (S.I.)**
Density	3.54	3.58	3	3.98	Mg/m^3
Fracture Strength	833.3	1666.6	690	5500	MPa
Fracture Toughness	2.7	2.8	3.3	5	$MPa.m^{1/2}$
Shear Modulus	92	122	88	165	GPa
Tensile Strength	83.3	166.7	69	665	MPa
Young's Modulus	270	330	215	413	GPa
Melting Point	3080	3135	2277	2369	K

2.3 Ceramic components manufacture

Ceramic components manufactured in this study were seedpads and GMS slugs using a uniaxial press, the study on powder preparation, uniaxial compaction and sintering were conducted to gain some understanding of these processes.

2.3.1 Preparation of powders for compaction

Spray drying is the most after used method for granulating powders for manufacturing ceramic components. Binders are added to powder at a slurry stage before spray drying to give pressed components sufficient strength required to be ejected from the compacting mould, handled without falling apart and possibly machined while in the green state. Binders in granules assist particles to maintain their shape in powder handling, transportation and storage. Lubricants such as clays, talc, stearates of magnesium or zinc and waxes are added into powders to reduce friction between tooling and powder compact during compaction. Plasticisers are used to reduce the viscosity of binders, for example, polyethene glycols (PEG) on binder polyvinyl alcohol (PVA) [35]. Powder mixing where pressing aids are not evenly distributed are undesirable because components formed may have a poor density distribution in a body [36].

2.3.2 Compacting of powders

Powder densification to make ceramic components can be achieved through one of the following methods, (i) sintering to densify the powder, (ii) compaction to high density followed by sintering and (iii) pressing and sintering simultaneously [36]. Compaction pressure deforms powder granules into a high-density component using two methods of pressing powders: uniaxial pressing and isostatic pressing [37]. Uniaxial pressing involves the compaction of powder in a rigid or hardened die by applying pressure in one uniaxial direction to final or near net component geometric tolerances [35]. Isostatic pressing utilises bags filled with powder immersed in a pressure vessel, powders are compacted by a pressurising vessel to a pre-set pressure to form compacts [37]. At the initial stages of powder pressing, density increases rapidly then increases more slowly with further pressure increase as shown in Figure 17 [37].

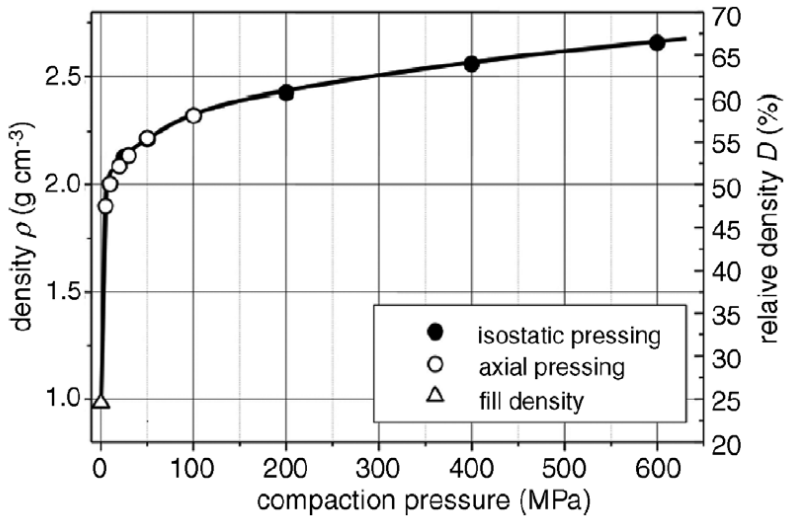

Figure 17 Density versus compaction pressure of alumina powder compaction [35].

Compacting pressure gradients in a uniaxial pressing due to powder-powder friction and powder – die wall friction effects component density gradient shown in Figure 6, friction plays a major role in setting up the compacting pressure gradients. The resultant force of die wall friction and particle-particle friction works against applied pressure, the shear stress at the wall increases with increasing pressure. The areas experiencing high pressure will compact more and become denser than the areas experiencing less pressure [38].

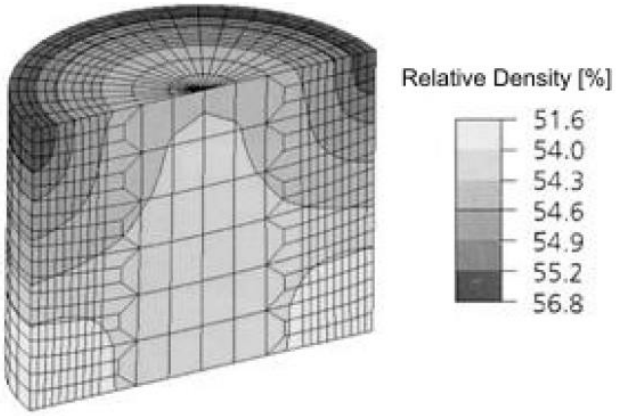

Figure 18 Density distribution in the upper half of a dry pressed cylinder [39].

The density gradient can be reduced by (i) properly levelling powder in the die, poor powder addition such as heaping makes heaped area to be compacted to higher density. (ii) Choosing suitable binders and lubricants help to reduce powder – wall friction, preventing pressed component density gradients. (iii) Elimination of agglomerates prevents powder from a uniform exposure to applied pressure, the agglomerates can shrink faster than the surrounding compact during firing, causing density gradients [40]. Elastic energy stored in the compact causes a spring back behaviour after pressing, the component size increases slightly axially as well as radially after ejection due to spring back effect. Increasing compact pressing pressure results in the increase of spring back effect. The difference in pressure for a compacted part in the die and the ejected part from the die that has experienced a spring back lead to cracks that are perpendicular to the applied force. Plasticiser is added into powder to reduce the spring back effect on pressed compacts [36]. Table 2 summarises advantages and limitations of uniaxial pressing.

Table 4 Advantages and limitations of uniaxial pressing [41].

Advantages	Limitations
The compaction can be done in a dry state at less than 3% powder moisture.	Poor density distribution within a compact from top to bottom is undesirable during sintering.
Density achieved depends strongly on the powder properties and whether any binders were used.	Suitable for small and simple geometrical components.
Low dimensional tolerance and smooth surface finish can be achieved.	Die wear leads to dimensional problems and replacement of dies is expensive.
High throughput of components due to short cycle times and the system can be fully automated.	Powder treatment such as the addition of binders and plasticisers are necessary before use in the press.

2.3.3 Sintering

Sintering is the consolidation of compacts or powdery agglomerate under the influence of temperature to create a mechanically cohesive, usually polycrystalline solid [36]. The sintering processes involve:

- Consolidation – formation of necks that combine particles together
- Densification – reducing porosity, this results in overall size reduction
- Grain coarsening – grain growth
- Physiochemical reactions – in the powder and sintered material

Figure 19 shows the starting powder particles and their subsequent configuration when sintered with densification and shrinkage and without densification.

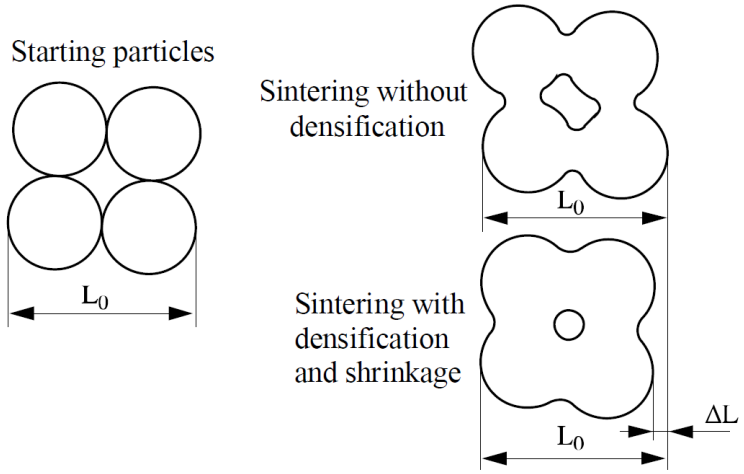

Figure 19 Sintering of the powder particles [36].

Isostatic or uniaxial pressing is generally employed to aid sintering, pressure can be utilised during the sintering process to achieve desired sinter quality. Heat is usually added during sintering but the chosen device has to withstand high temperatures. Pressureless sintering does not utilise devices providing pressure to aid sintering. The driving force of sintering involves (i) minimising surface energy and energy of grain boundaries (ii) minimising external energy as in hot pressing/isostatic pressing (ii) minimising of chemical energy as in reactive sintering [36]. Thermal energy is required for sintering to overcome energy barriers between higher energy states of compacted

powder to lower energy states of consolidated material. Minimization of surface energy provides the driving force during pressureless sintering.

Grain boundary energy for most materials, especially metals, is smaller than surface energy [42]. Solid particles have surplus energy γ_{SV} per unit area on their surfaces, where s is the solid and v is the vapour. In a sintered polycrystalline material, the grains are separated by grain boundaries whose surplus energy is given by γ_{GB}, where GB is the grain boundary. In general $\gamma_{GB} < \gamma_{SV}$, therefore the powder lowers its energy as the particle surfaces convert into grain boundaries during sintering to a polycrystalline material. The driver for sintering is the reduction of system interfacial energy given by Equation 4.

$$G = \gamma A \qquad \text{Equation 4}$$

γ = specific interface energy

A = surface area

Interfacial energy G can be lowered by reducing γ or A or both A and γ, area A can be reduced by combining small powder particles with volumes v, and surface a, to form new larger particles with a volume V and surface area A [36]. Equation 5 demonstrates the area A, is less than the area a, made from a number n, of small particles combined.

$$A < na \qquad \text{Equation 5}$$

Alumina and Magnesia are both susceptible to grain growth at the closing stages of sintering, this can lead to undesirable material properties [43], [44]. To counter grain growth, nano-sized particles are used as starting feedstock to achieve grains within the desired sintered size range. Other methods that have been utilised to reduce the effect of grain growth are doping with grain growth inhibitors such as yttria, zirconia and silicon carbide. These materials will act as grain boundary pinning agents and can reduce grain boundary mobility. Shortening sintering time by the use of superior sintering methods such as microwave or spark plasma has proven to be an effective method of countering grain growth [45].

2.4 Mechanical properties of materials

In order to fully understand the behaviour of seedpad compact during pressure transmission, a study of materials mechanical behaviour was done.

2.4.1 Tensile tests

The stress-strain diagram shown in Figure 20 was obtained by subjecting a test piece under a tensile load.

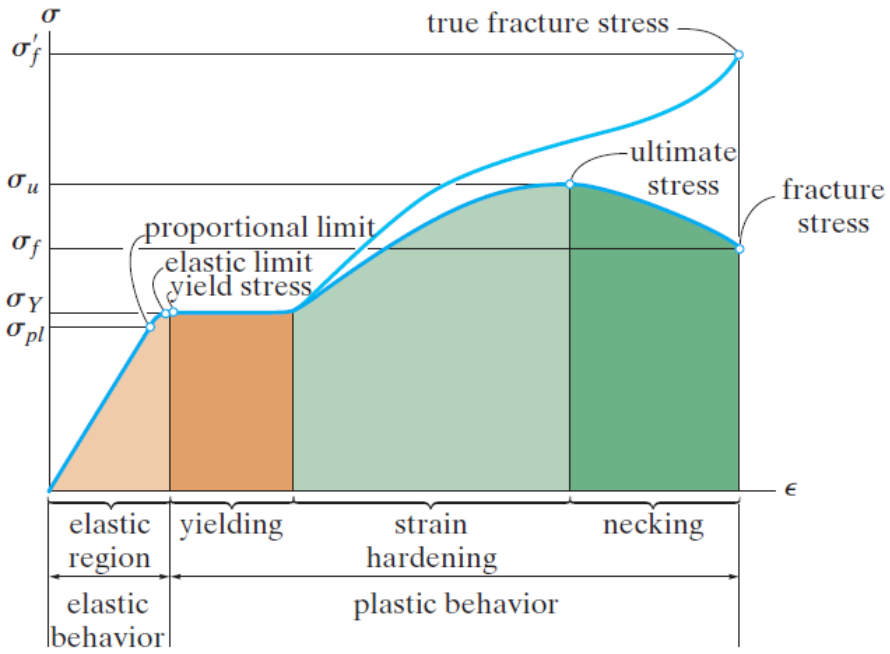

Figure 20 Conventional and true stress strain diagram for ductile material (steel) not to scale [46].

In the elastic behaviour region, the stress is proportional to strain and the graph is almost a straight line up to the proportionality limit σ_{pl}. Applying stress beyond the proportional limit causes the curve to bend and flatten out towards the elastic limit. The material returns to its original shape if stress or load is removed before the elastic limit. For metals and most ductile materials, the proportional limit and elastic limit are closer to each other and difficult to detect. Past the yield point of the stress-strain curve, the material starts to deform permanently, the stress that causes yielding is called yield stress or yield point σ_Y. The region beyond yielding is the strain hardening, which typically has the form of a curve that gradually bends upwards to a maximum stress

value called ultimate tensile stress σ_u. During loading or stress increase, the cross sectional area of the specimen decreases over its entire length. A point is reached where the cross section area decrease becomes localised to a certain region in the specimen, this process is called necking and the stress strain diagram bends downwards until the sample breaks at fracture stress, σ_f. True stress strain diagram is obtained if the actual cross sectional area was used instead of the original cross sectional area of the material or test specimen, the breaking point occurs at true fracture stress σ'_f[46]. The designs of most engineering components are made to work in the proportionality region. Brittle materials and most ceramics fracture beyond the yield point, while ductile materials will show plastic deformation before fracture [47].

2.4.2 Compression tests

Brittle materials are weaker in tensile stress compared to compression stress. Under tensile stress, the presence of small flaws, be they cracks or voids facilitates the propagation of cracks in the direction perpendicular to the applied tensile stress. The stress-strain graphs for brittle materials are shown in Figure 21, grey cast iron and a concrete material [48].

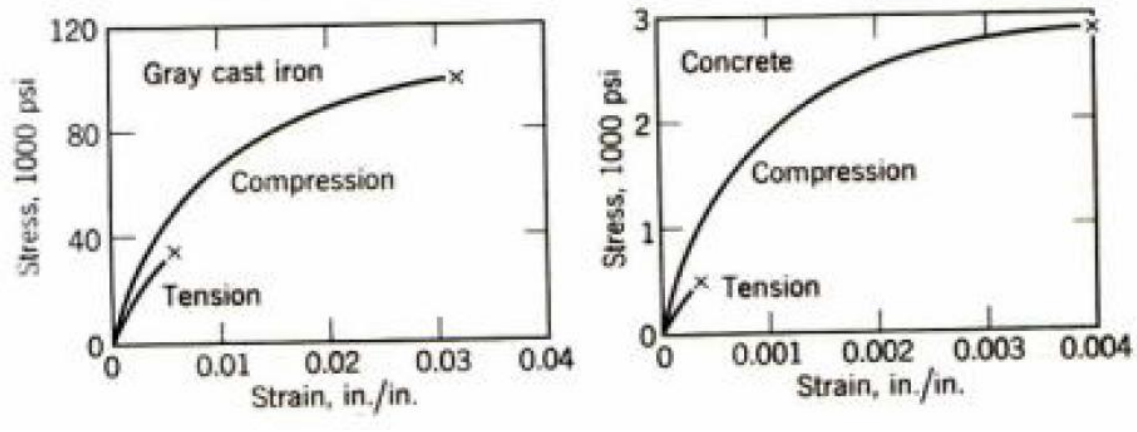

Figure 21 Tensile and compressive engineering stress strain curve for grey cast iron and concrete [48].

Compressive failure in brittle materials occurs by shear fractures at a plane of 45° to the direction of compression force. The frictional force at the ends causes the material

to barrel, the compressive force is more in the middle than on barrelled sidewalls [49]. Friction and bulking limit the compression test. The ends of the material are subjected to friction that prevents lateral movement and the cones formed at the ends result in specimens forming barrels. Friction can be reduced by lubricating specimen ends and the effects of friction can be reduced by increasing height to diameter ratio. Although increasing height to diameter ratio reduces friction, a higher ratio above 3 can cause buckling [49].

2.4.3 Failure of brittle materials

In engineering, a fracture mode can be brittle or ductile. Classification is based on whether or not the material undergoes plastic deformation. Ductile materials absorb more energy before fracture whilst brittle materials absorb less energy before fracture. Fracture process involves crack formation and propagation in response to the stress applied. Plastic deformation shows up at advancing crack tips in ductile materials whilst there is a rapid crack formation with very little plastic deformation in brittle materials. Ceramics are mostly brittle materials and therefore undergo very little or no plastic deformation under applied stress. It has been observed that ceramic materials have fracture strength lower than theoretically predicted. Griffith's theory indicates that this discrepancy is due to flaws (typically cracks) that exist in the body and surface of the material. Figure 22 (a) and (b) demonstrates the stress profile in the presence of microscopic cracks [50].

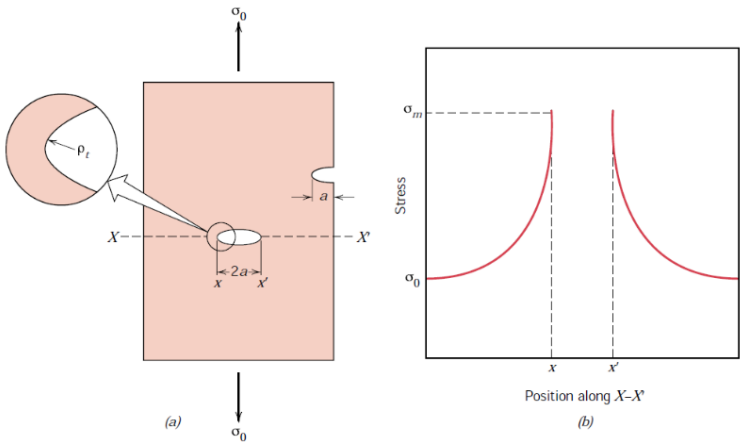

Figure 22 (a) Internal cracks geometry and (b) a schematic stress profile along the x – x' [50].

Assuming the crack has an elliptical shape oriented perpendicular to applied stress. The max stress at the crack tip, σ_m is given by equation 6.

$$\sigma_m = 2\sigma_o \left(\frac{a}{\rho t}\right)^{1/2} \qquad \text{Equation 6}$$

σ_o = nominal applied tensile stress,

ρt = radius of the coverture at the crack tip,

a, = length of the surface crack or half-length of internal crack

For a long crack with a small radius, the ratio (a/ρ_t) is large and this yields σ_m that are many times σ_o. The ratio of σ_m/σ_o is the stress concentration factor K_t, given by Equation 7, it is a measure of how external stress is being amplified at the surface of a crack tip.

$$K_t = \left(\frac{\sigma_m}{\sigma_o}\right) = 2\left(\frac{a}{\rho t}\right)^{1/2} \qquad \text{Equation 7}$$

The fracture toughness K_c, Equation 8, is the measure of resistance to brittle fracture, it is the stress concentration factor at which with increasing σ_o the crack begins to propagate.

$$Kc = Y\,\sigma_c\sqrt{\pi a} \qquad \text{Equation 8}$$

Y = dimensionless parameter that depends on both crack and specimen sizes and geometries as well as a manner of load application.

σ_c = critical stress required for crack propagation in a brittle material is given by Equation 9.

$$\sigma_c = \left(\frac{2E\gamma s}{\pi a}\right)^{1/2} \qquad \text{Equation 9}$$

E = modulus of elasticity,

ɣs = specific surface energy,

Failure in ceramic materials is due to unstable crack propagation under tensile or compressive stress that exceeds the ultimate tensile or compressive stress of the material. Brittle failure occurs when the Mode 1 stress intensity factor K_1 reaches the fracture toughness of a material K_{1C}. The test procedure commonly used for validating the strength of ceramics and hard materials is a flexure test. The flexure test method can either be a 3 point or 4 point bend test. Material specimens are prepared by simple machining and placed on a test apparatus. The strength determined in bending is termed the flexural strength, the Transverse Rupture Strength (TRS), or Modulus of Rupture (MOR), corresponds to maximum tensile stress developed at the point of fracture [50].

2.4.4 Distribution of flaws in ceramic materials

The flaw distribution in ceramic materials generally follows a normal distribution. Test pieces taken from a parent material may contain different flaws varying from small to large sizes. The largest flaws will cause failure in material under applied stress, test sample with the largest flaws will be closer to the right tail shown in Figure 23. Samples with largest flaws have non-symmetric distributions [51]. The size, orientation and shape of flaws in a given flaw population determines the variability of failure stress [50].

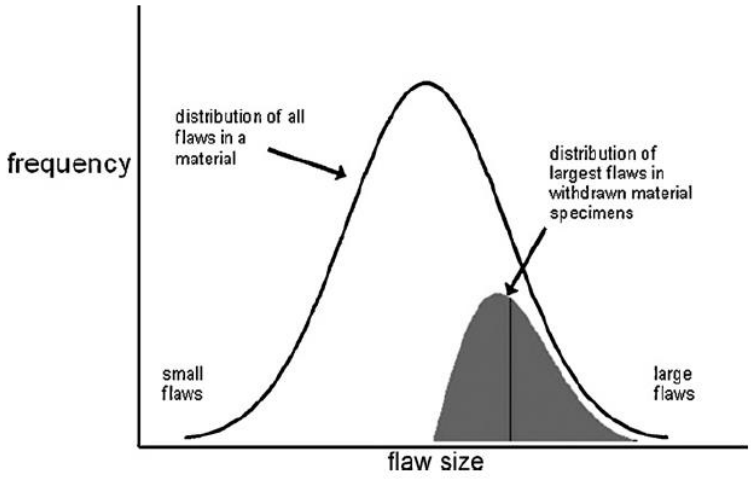

Figure 23 Total flaw distribution and largest flaw distribution in a material [51].

There are generalized distribution models for extreme value statistical models. These models are used due to deviations from Gaussian or normal distribution shapes. There are three models, namely Gumbel, Frechet and Weibull. Fisher and Tippet (1928) were credited with defining the extreme value distribution and showing that there could only be three types.

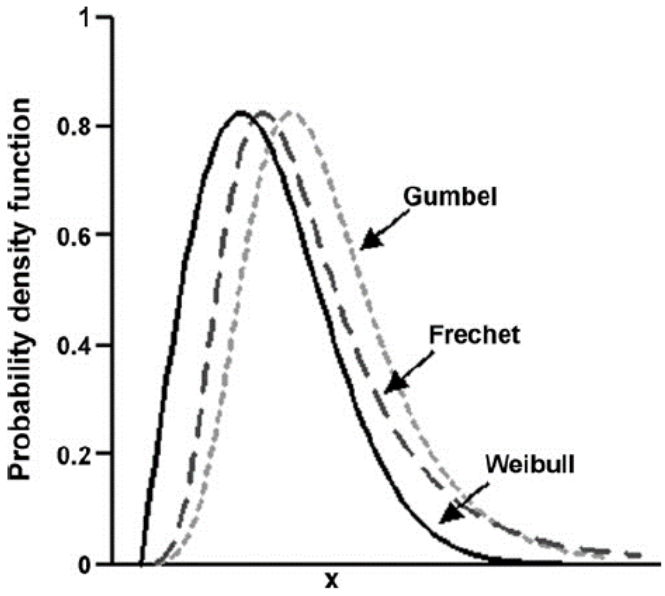

Figure 24 Three types of distribution offset along the x-axis for easier comparison, where x is the flaw size [51].

Both Gumbel and Weibull functions in Figure 24 have demonstrated a good fit for the strength of ceramic materials. A Weibull distribution can provide a more accurate prediction with a small number of samples, hence considered to be the best choice. The cumulative probability is such that the probability of failure P_f, given by Equation 10, increases with the increase of fracture stress variable σ.

$$P_f = 1 - e^{-\left(\frac{\sigma-\sigma_u}{\sigma_o}\right)^m} \qquad \text{Equation 10}$$

σ_u = threshold strength parameter

σ_o = scale parameter or characteristic strength

m = Weibull modulus

This is a Weibull three parameter strength distribution. The threshold strength parameter σ_u represents the minimum strength of the material i.e. where it will not break. The scale parameter or characteristic strength σ_o is dependent on the stress configuration, test specimen size and the flaw population of the material being tested. The test piece size and stress subjected to the sample will determine the shift of the distribution along the abscissa axis. The parameter m is the Weibull modulus representing the strength distribution width. A high value of gradient or steep slope in Figure 25 indicates a narrow distribution is more desirable as materials with higher modulus are predictable as far as failure stress is concerned.

Setting σ_u equal to zero, a simplified two parameter Weibull function is defined, Equation 11. The σ_u represents the lower strength, the boundary conditions for flaw sizes. Applying the double logarithms from both sides, Equation 12, an expression that yields a simplified graphical Weibull parameter is reached, Equation 13.

$$P_f = 1 - e^{-\left(\frac{\sigma}{\sigma_o}\right)^m} \qquad \text{Equation 11}$$

$$\ln(1 - P_f) = -\left(\frac{\sigma}{\sigma_o}\right)^m \qquad \text{Equation 12}$$

$$\ln\left(\ln\left(\frac{1}{1-P_f}\right)\right) = m(\ln\sigma) - m(\ln\sigma_o) \qquad \text{Equation 13}$$

The characteristic strength σ_o is a location parameter, large σ_o shifts data to the right while small σ_o shift data to the left. The characteristic strength is the strength value when the left hand side of the equation above is zero [51].

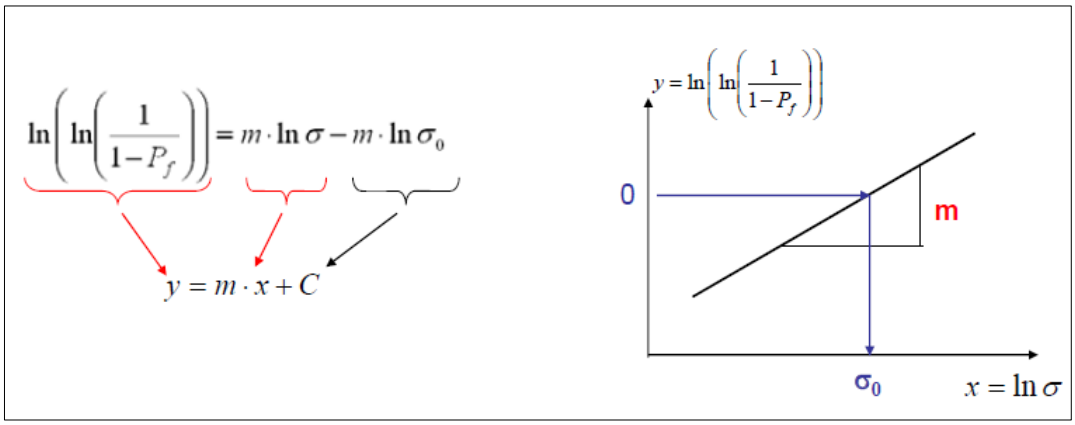

Figure 25 Graphical presentation for determining m and σ [52].

If the failure probability of N specimen is known, the failure probability of N+1 specimen can be predicted. The probability is defined by equation 14, the number of tests N is typically 20 to establish reasonable accuracy and predictability [50].

$$Pf(\sigma_i) = \frac{i - 0.5}{N} \qquad \text{Equation 14}$$

Diamond synthesis is dependent on the strength of seedpads material to hold grit at the defined position, purity of alumina provides added advantage to stabilising HPHT diamond synthesis.

Chapter 3: Experimental Methods

This chapter describes in detail the methods used to make magnesia seedpads, alumina seedpads and GMS slugs. Magnesia seedpads and alumina seedpads were assembled with GMS slugs into capsules and used in HPHT cubic diamond synthesis press to compare seedpads stability during diamond synthesis. Characterisation of magnesia and alumina powders, seedpads and synthesised materials were described in order to investigate the outcome for using alumina seedpads in HPHT diamond synthesis.

3.1 Raw materials used for the study

3.1.1 Spray dried alumina and Spray dried magnesia

Spray dried magnesia powder and spray dried alumina powder for making seedpads were sourced from Wonderstone Mine Ltd, Ottosdal, North West province of South Africa. Alumina was spray dried by its manufacturer, Albemarle GmbH, Germany from its pure alumina grade KSM99 raw powder. The manufacturer of magnesia is Nedmag Industries in the Netherlands, the raw magnesia powder, Nedmag, was spray dried by Wonderstone Mine Ltd. Table 5 show specifications for raw magnesia powder (Nedmag) and raw alumina powder (KSM 99) used for spray drying powders. Nedmag powder utilised polyvinyl alcohol (PVA) and hydro wax, KSM99 powder utilised poly ethyl glycol (PEG) binder for spray drying. Both Nedmag and KSM99 were sourced from Wonderstone Mine Ltd for characterisation to understand raw powders before spray drying, as they did not contain binders nor were they spray dried.

Table 5 Magnesia (Nedmag) and alumina (KSM99) raw powder specifications [53], [54].

Nedmag (MgO)	%
MgO	98.5
CaO	0.74
SiO2	0.12
B2O3	0.01
Al2O3	0.07
Fe2O3	0.44
MnO2	0.12
Screen size	63 µm

KSM99 (Al_2O_3)	%
Al2O3	>99.0
Na2O	0.05
Screen size	4 µm

3.1.2 Graphite and metal solvents (GMS)

High purity graphite and metal solvents (cobalt, nickel and iron powders) were used for making GMS granules that were uniaxially pressed and sintered to GMS slugs. Iron powder UN3089 was sourced from BASF Chemicals, Germany. Cobalt powder Co006012 was sourced from Goodfellows Ltd, the United Kingdom. Nickel powder 1378 was sourced from Alfa Chemistry, USA. Graphite powder 2N was sourced from American Elements, USA. Binders used were methylcellulose A4C, sourced from Dow Europe GmbH and polyethene glycol 200, sourced from Honeywell Fluka the UK.

3.1.3 Diamond seeds

Cubic diamond seeds 30/35 mesh size were sourced from CR Gem Superbrasive Co. Ltd, China. Diamond seeds were screened using 30/35 mesh, (530 µm / 500 µm), 3-inch diameter British Standard sieves to obtain same seed sizes for assembling magnesia seedpad and alumina seedpad. Diamond seeds and synthesised diamonds

were visually checked using a ZEISS Primoster optical microscope for chipping and inclusions. Defective diamond seeds were removed because they affect the quality of the synthesised diamond.

3.1.4 Capsule components

Element Six Pty Ltd cubic diamond synthesis press was used for study hence cubic capsule components; envelopes, thumbtacks, graphite heaters, MgO cups, iron cups were sourced from Laixeng, China.

3.2 Characterisation of raw materials

Characterisation of magnesia, alumina and GMS powders and components was done using different analytical methods: sieve analysis, laser diffraction, XRD and SEM-EDS to as per Element Six Pty Ltd method of pre-qualifying raw materials before diamond synthesis. Standard quality control procedures, used by Element Six Pty Ltd, were used for characterisation.

3.2.1 Powder particle size distribution (PSD)

Spray dried magnesia and spray dried alumina powders PSD were determined and compared using British Standard test sieves ASTM - E1638-18. Electroformed sieves were placed from the bottom pan in ascending sizes order of 45 µm, 125 µm, 300 µm and 500 µm. Pascal sieve shaker was pre-set by the manufacturer to a specific vibration amplitude of 1.5 mm and a frequency of 40 Hz, the vibration time was set to 15 minutes. A Mettler M4800 scale was used to weigh a 100 g sample to an accuracy of 0.01 g, the mass of powder retained on each sieve size was determined as percentage fraction of 100 g initial mass. The PSD is critical in determining how particles would freely sit in a die cavity during a uniaxial pressing of seedpads compact process.

PSD of raw powders were compared by a laser diffraction method, ASTM D4464-15, using a Malvern Mastersizer 2000 on raw magnesia (Nedmag) powder and raw

alumina (KSM99) powder. Raw powders were suspended in deionised water with sodium hexa-meta-phosphate as a dispersing agent before being introduced into a Malvern analyser. The statistics of derived size diameters were obtained to compare magnesia (Nedmag) and alumina (KSM99) particle size distribution. The D50 is also known as mass or volume median diameter of particles, this is the diameter for which 50% of the sample's particles is smaller than and 50%, the same rationale applies to the D10 and D90 parameters. The volume-mean diameter D[4,3] and the surface area mean diameter D[3,2] were also obtained [55]. The PSD graphs were used to compare the particle size distributions of magnesia (Nedmag) and alumina (KSM99) powders [56]. The particle size of raw powders assists in pre-determination of final sintering behaviour in powder compacts.

3.2.2 Powder moisture

The moisture content in powders is critically monitored during the uniaxial compaction process. Lower moisture content may result in compact cracking and higher moisture content may result in compacts sticking onto tooling forming surface imperfections. Moisture analyser AND ML50 with a measurement resolution of 0.1 % set at 115 ^{o}C for 10 min analysis time was used to determine moisture content in the powder samples. A sample of 10 g was weighed to an accuracy of 0.01 g using a Mettler M4800 scale and placed on a moisture analyser pan, moisture calculation was derived from Equation 15 [57].

$$\text{Moisture (Wt \%)} = \frac{\text{Wet sample mass (g)} - \text{Dried sample mass (g)}}{\text{Wet Sample mass (g)}} \text{x } 100 \quad \text{Equation 15}$$

3.2.3 Powder bulk and tap density

Powder bulk density determines how much powder mass will be deposited into the die cavity during volume feeding of a uniaxial press. A lower powder density results in low final compacted seedpad compact mass and a higher powder density results in high final compacted seedpad compact mass from same powder volume generated by uniaxial press shoe feeder. Magnesia and alumina powders bulk and tapped density were measured using a Hosokawa powder characteristic tester, ASTM D6683-19. The powder sample was passed through a 750 µm screen to freely fall into a standard 100

cm^3 calculated volume cup of predetermined mass (mass of empty cup). The cup filled with powder was levelled using a straight edged steel rule and placed on a Mettler M4800 scale to accurately weigh to 0.01 g to obtain a combined mass of the cup and powder sample (mass of filled cup). The bulk density was determined using Equation 16 [58].

$$\text{Bulk density } (\text{g/cm}^3) = \frac{\text{mass of filled cup (g)} - \text{mass of empty cup (g)}}{100\ \text{cm}^3} \quad \text{Equation 16}$$

A tap density calculation used the same method for bulk density determination, but an extension tube was inserted into the cup to add more powder. The powder sample in the cup was tapped 180 times at a frequency of 50 Hz. The extension tube was removed to level the powder to determine powder tapped density [58]. Powder flow quality during compacting was assessed by compressibility or Carr index. Powders with high frictional interaction have a higher Carr index, they tend to form undesirable density gradient on compacts. Carr index was determined by calculating the difference between tapped density and bulk density divided by tapped density using Equation 17 [59].

$$\text{Carr Index } (\%) = \frac{\text{Tap density } (\text{g/cm}^3) - \text{ Bulk density } (\text{g/cm}^3)}{\text{Tap density } (\text{g/cm}^3)} \text{x}100 \quad \text{Equation 17}$$

Hausner ratio is also a common method of expressing powder flow and is related to the Carr index by Equation 18 [59].

$$\text{Hausner ratio} = \frac{1}{1 - \text{Carr index}} \quad \text{Equation 18}$$

Table 6 summarises flow character in relation to Carr index and Hausner ratio to powder flow character.

Table 6 Carr index and Hausner Ratio for powder flow character [60].

Carr Compressibility index %	Flow character	Hausner Ratio
1 – 10	Excellent	1.00 – 1.11
11 – 15	Good	1.12 – 1.18
16 – 20	Fair	1.19 – 1.25
21 – 25	Passable	1.26 – 1.34
26 – 31	Poor	1.35 – 1.45
32 – 37	Very poor	1.46 – 1.59
>38	Very, very poor	>1.60

3.2.4 Powder loss on ignition (LOI)

LOI determines organic or volatile material content in powders, organic matter may include added binders. LOI was used to predict and compare binder content and mass loss in seedpad fired compacts from uniaxial pressed spray dried magnesia powder and spray dried alumina powder. Powder samples were weighed to 20 g on a Precisa 310M scale accurately to 0.001 g at room temperature, heated to 900°C in a muffle furnace for an hour and cooled in a desiccator to room temperature for re-weighing. The percentage of powder mass loss was equivalent to percentage LOI given by Equation 19.

$$\text{LOI (Wt \%)} = \frac{\text{Initial powder mass (g)} - \text{Heated powder mass (g)}}{\text{Initial powder mass (g)}} \text{x100} \quad \text{Equation 19}$$

3.2.5 X-ray fluorescence spectrometry (XRF)

The Energy Dispersive XRF elemental analysis of magnesia (Nedmag) and alumina (KSM99) powders was conducted on an XRF PW2410 Phillips instrument. This technique was used to determine qualitatively and semi-quantitatively the elements

present in the sample to verify powder purity. The detection limits were from 0.5 ppm to 100 % and the detection capability ranged from sodium to uranium [61]. Heavier elements had better detection limits than lighter elements, the amount of material present was related to the intensity of the corresponding peak [62].

The elements corresponding to the individual peaks were determined by the characteristic energy emitted by an atom of the element. The energy levels of the lines denoted as K, L, or M were emitted from an atom excited by high energy x-rays. Each atom emits more than one type of lines and the ensemble of the lines emitted is a characteristic of that atom [62]. Excited electrons shown in Figure 26 from the K shell left the atom entirely and were replaced by L and M shell electrons emitting K_α and K_β radiation. The L shell electrons were replaced by M and N shell electrons and these also emitted L_α and L_β radiation. The radiation emitted by electron transfer was detected by the XRF counter and was characteristic for particular elements [63].

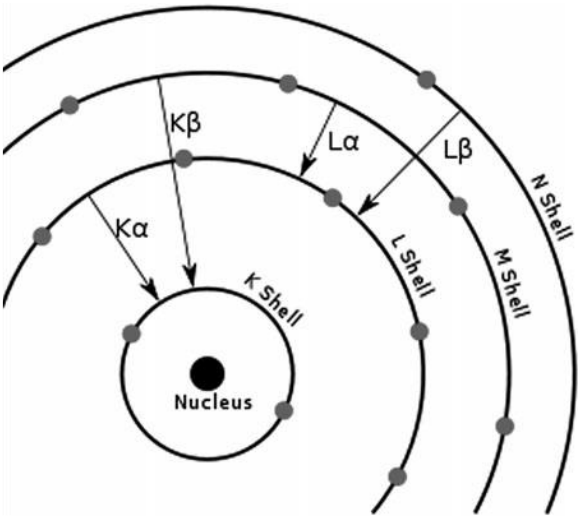

Figure 26 An illustration of an atom showing energy levels K, L, M and N [63].

3.2.6 X-ray diffraction (XRD)

Phase identification and the level of purity determination of magnesia (Nedmag) and alumina (KSM99) powders was conducted using PANalytical x-ray diffractometer fitted with Co as the target material. The results were analysed using XPert high score software which was capable of identifying the phases present. X-rays are

electromagnetic radiation of a wavelength of the order of 1x 10^{-10} m or 1 Å, which is much shorter than that of visible light. When x-rays strike a crystal or polycrystalline powder they are scattered by the electrons of the constituent atoms [64]. The scattered radiation generates reflected beams through constructive interference of the scattered radiation from all the atoms involved. The conditions for constructive interference dictate at what angle the x-ray beams need to strike a particular crystallographic plane in order for this process to take place. The principle of this interaction between the x-ray beam and the crystal is shown in Figure 27.

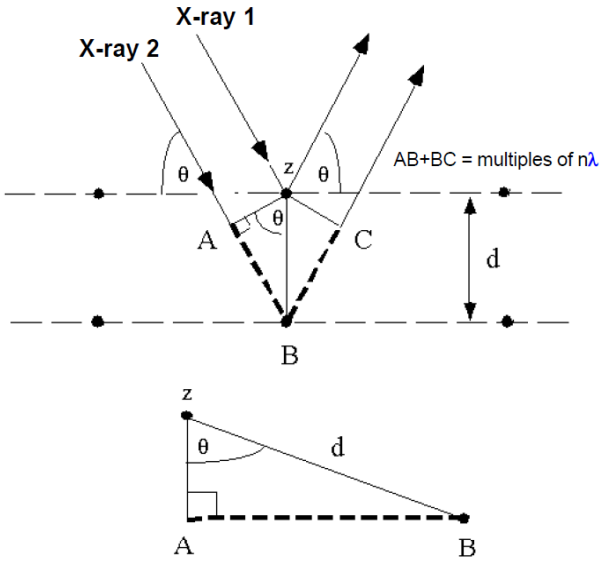

Figure 27 X-ray 1 and 2 diffraction [65].

The horizontal parallel black dotted lines in Figure 27 denote crystal atoms lying on two parallel crystallographic planes. Diffraction occurs when Bragg's law is satisfied, i.e. when the length of path ABC in is a multiple of the impinging radiation's wavelength. Bragg's law is given by Equation 20.

$$\lambda = 2d_{hkl}\mathrm{Sin}\theta_{hkl} \qquad \text{Equation 20}$$

λ = wavelength of an x-ray beam

d = crystal planes spacing

Bragg's law determines the position 2θ of the x-ray diffraction peaks, Miller indices h, k and l are used to identify lattice plane and the inter-planar spacing d for different unit cells are given by the following Equations 21 to 25, for different crystal system.

$$\text{Cubic } \frac{1}{d^2} = \frac{(h^2 + k^2 + l^2)}{a^2} \qquad \text{Equation 21}$$

$$\text{Tetragonal } \frac{1}{d^2} = \frac{(h^2 + k^2)}{a^2} + \frac{l^2}{c^2} \qquad \text{Equation 22}$$

$$\text{Orthorhombic } \frac{1}{d^2} = \frac{h^2}{a^2} + \frac{k^2}{b^2} + \frac{l^2}{c^2} \qquad \text{Equation 23}$$

$$\text{Hexagonal } \frac{1}{d^2} = \frac{4}{3}\left(\frac{(h^2 + hk + k^2)}{a^2}\right) + \frac{l^2}{c^2} \qquad \text{Equation 24}$$

$$\text{Monoclinic } \frac{1}{d^2} = \frac{1}{Sin^2\beta}\left(\frac{h^2}{a^2} + \frac{k^2 Sin^2\beta}{b^2} + \frac{l^2}{c^2} - \frac{2hlCos\beta}{ac}\right) \qquad \text{Equation 25}$$

Where a, b and c represent the smallest non coplanar vectors that describe the unit cell with included angles of α, β and γ [66]. These peaks were used to identify the crystalline phases present in the magnesia and alumina powders, the area under the peaks is related to the amount of each phase present [61].

3.2.7 Thermogravimetric analysis (TGA)

TGA measures the amount of weight gain or loss of a sample with temperature or time in a controlled atmosphere [67]. A Mettler Toledo TGA2 STAR System, TGA was used to compare magnesia (Nedmag) powder and alumina (KSM99) powder moisture uptake from ambient air. The powders were cleaned by heating in a muffle furnace at 900 ^{o}C for an hour to remove moisture and any volatiles that might be present, cooled in a desiccator before they were left in ambient air for some weeks. Thermal cycles were conducted in synthetic air to reduce natural air variation such as moisture fluctuations and repeated in a nitrogen (non-oxidising) environment to check the influence of oxygen on powders. The powders were analysed and compared just after being cleaned in a 900 ^{o}C muffle furnace and after exposure to ambient air for some weeks. The powders moisture uptake was monitored on a weekly basis using loss on ignition (LOI) method described 3.2.4 and the results were plotted on moisture vs time graph.

3.2.8 Scanning electron microscope (SEM)

The SEM was used to analyse raw magnesia (Nedmag) and alumina (KSM99) and spray dried magnesia and alumina powders, respectively. This was done to compare the morphology of raw and spray dried powders, SEM was capable of identifying the presence of impurities by use of compositional difference (z contrast). The SEMs used in the study was a Phillips XL30 and a Jeol 7500. The powders were placed onto a sample holder using a nonconductive double sided tape to prevent movement while moving the stage. The voltage was set at 15keV, Secondary Electron (SE) and Backscattered Electron detectors (BE) were used for the analysis. The BE detector shows a good crystal orientation (channelling contrast) from crystalline samples but has a poor spatial resolution. The SE detector has a good spatial resolution and shows crystal orientation but poor compositional differences [68]. The SEM had Electron Dispersive Spectroscopy (EDS) attached to identify elemental composition present in the powders [69].

3.2.9 Compressive fracture strength test

Seedpads hold diamond seeds at defined spacing and orientation, therefore it is imperative that they have some strength to withstand fracture during a cubic capsule assembly and initial compressive forces at the beginning of HPHT press compaction. A compression test was done at ambient temperature to predict the behaviour of fired magnesia compacts and alumina compacts under the compressive forces on an Instron test rig model 1175 shown in Figure 28 at Mintek, Johannesburg. The standard used to ensure conformity of this test was ASTM C1424-15.



Figure 28 Instron test rig model 1175.

The surfaces of compression fixture plates were cleaned using a lint free paper before loading each sample to ensure no debris remained on the surface to affect results. The load was applied to the sample until fracture, remnants were observed for evidence of vertical splitting that indicated invalid test; intact ends shown in Figure 29 indicated a valid test.

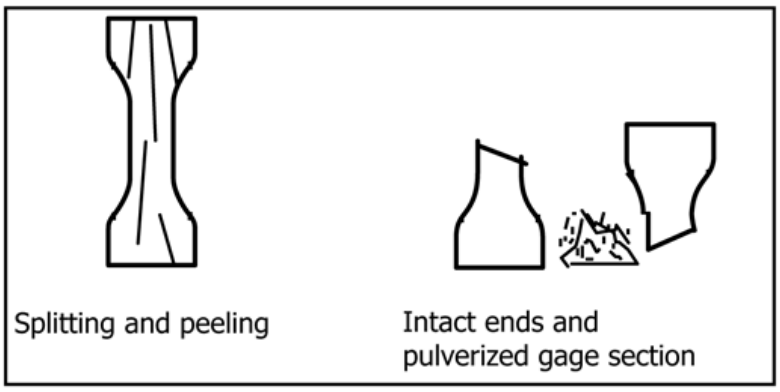

Figure 29 Illustration of peeling and splitting compared to intact ends [70].

The compressive strength of rods was given by Equation 26.

$$S_u = \frac{P_{max}}{A} \qquad \text{Equation 26}$$

S_u = compressive strength, MPa

P_{max} = maximum force, N

A = original cross section, m^2

Cross sectional area, A is calculated as, Equation 27.

$$A = \frac{\pi d^2}{4} \qquad \text{Equation 27}$$

d = average diameter of the gage, m

Magnesia and alumina cylindrical compacts samples for compression test were prepared by an 80 tonne uniaxial press, fired at 1100 ^oC for 4hrs in air, to achieve a 70 % density similar to that of fired seedpads. The slugs outside diameter (OD) to height (H) ratio was designed to be greater than two. Samples showing visible flaws such as cracks and holes were removed from the lot. Samples were OD and H were measured accurately with a calibrated micrometre to the accuracy of 0.001mm. Flatness, perpendicularity and concentricity specifications were measured to tolerance and accuracy shown in Figure 30 using a CMM 3D ZEISS machine. The surface finish was measured using a Mitutoyo SJ 201. Twenty magnesia and twenty alumina samples were prepared for compression test as per the recommended sample size for Weibull analysis [50].

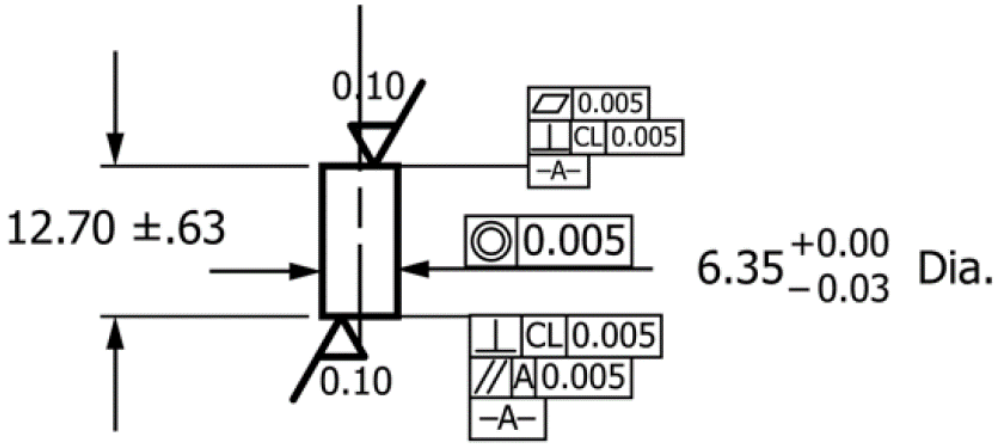

Figure 30 Drawing and specifications of samples prepared for compression test [70].

The Weibull analysis was used to analyse and compare the compressive fracture of magnesia and alumina samples. Weibull parameters were determined by a graphical plot as detailed in section 2.4.4.

3.3 HPHT diamond synthesis components preparation

Spray dried magnesia powder and spray dried alumina powder were sourced from different suppliers ready to uniaxial press seedpads compacts. GMS granules and GMS slugs were manufactured by following Element Six Pty Ltd production method. Seedpads and GMS slugs were fired under different conditions assembled with diamond seeds and other capsule components into cubic capsules for HPHT diamond synthesis. Details of these processes are given below.

3.3.1 Magnesia seedpads and alumina seedpads preparation

A 100 tonne uniaxial press was used for making green seedpads compacts from spray dried powders. Press hydraulic pressure was adjusted to vary green seedpads density to achieve a fired density specification 2.40 g/cm^3 – 2.45 g/cm^3 equivalent to 60 % to 70 % theoretical density as per current magnesia seedpads using 1100 ^{o}C profile shown in Figure 31. Theoretical % density was preferred as this would assist in comparing porosity of the two fired seedpads compacts. Pressed to size magnesia seedpads compacts and alumina seedpads compacts final discs geometry and mass:

Outside Diameter (OD) 40 mm, Thickness (T) 6 mm and Mass (M) 20 g to satisfy the final cubic capsule HPHT cubic press requirements. The pressure exerted on pressed components was calculated from the conversion formula given by Equation 28.

$$P_1 \text{ x } A_1 = P_2 \text{ x } A_2 \qquad \text{Equation 28}$$

P_1 = press hydraulic pressure, MPa

A_1 = hydraulic cylinder cross sectional area, m^2

P_2 = pressure exerted on pressed component, MPa

A_2 = die cross sectional area, m^2

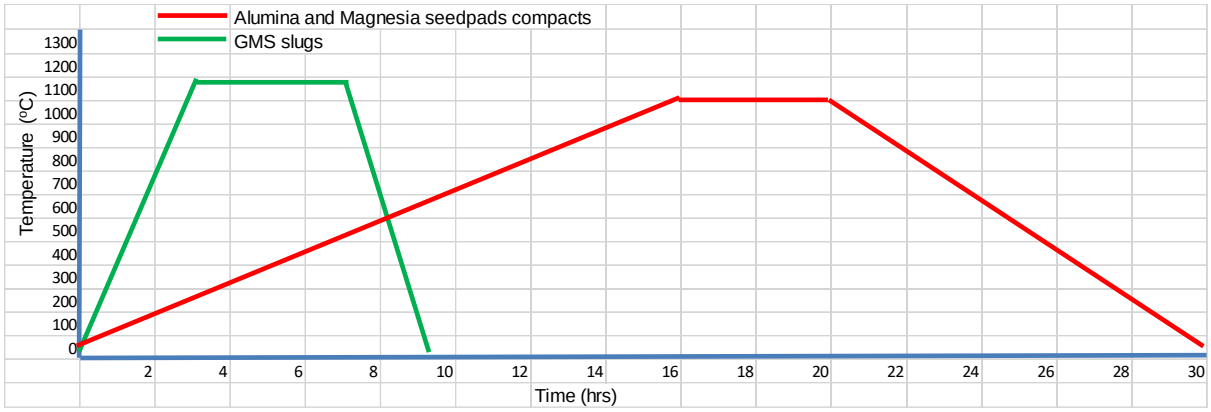

Figure 31 Firing profile cycle for magnesia and alumina seedpads compacts and GMS slugs.

3.3.2 Graphite with metal solvents (GMS) slugs

The flow diagram shown in Figure 32, describes sequential steps followed during the manufacture of GMS slugs under a clean environment to prevent possible contamination. Graphite, metal solvent powders iron, nickel, cobalt and binders methylcellulose and polyethene glycol were batched, mixed for an hour to form a uniform slurry using deionised water. The slurry was tape cast at 400 ºC to speed up drying to achieve a moisture content of less than 1.5 %. Tape cast material was passed through a hydrogen furnace with argon purging at 1020 ºC to reduce metal oxides.

Hydrogen furnace reduces metals at a faster rate, liberating water vapour to form high purity metals given by Equations 29 to 31 [71].

$$Fe_2 2O_3(s) + 3H_2(g) = 2Fe(s) + 3H_2O(g) \quad \text{Equation 29}$$

$$NiO(s) + H_2(g) = Ni(s) + H_2O(g) \quad \text{Equation 30}$$

$$CoO(s) + H_2(g) = Co(s) + H_2O(g) \quad \text{Equation 31}$$

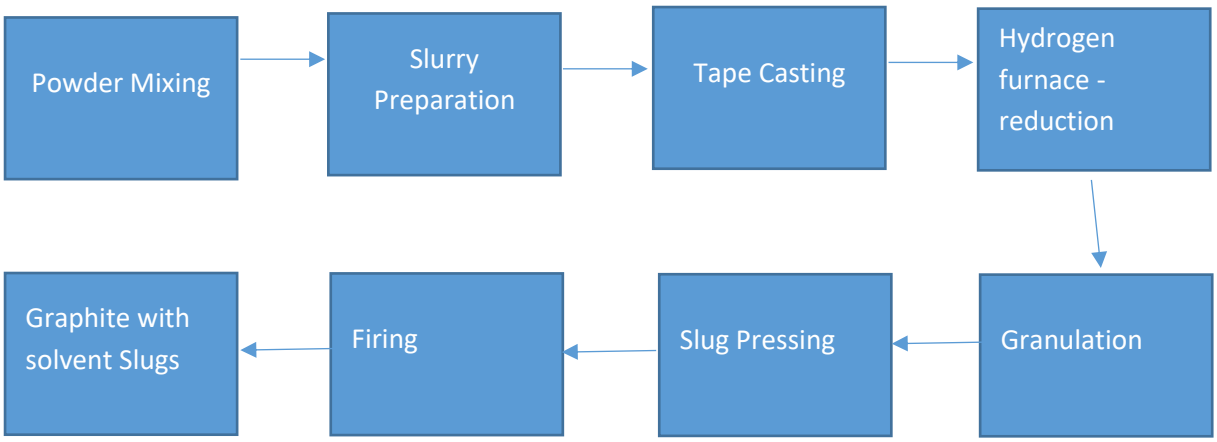

Figure 32 Flow diagram used for manufacturing GMS slugs.

Material from hydrogen furnace was granulated to form GMS granules used for compacting GMS slugs in a uniaxial press. GMS granules were checked for bulk density 1.0 - 1.3 g/cm^3 using method describe 3.2.1 and particle size distribution according to specification (>2.0 mm, 45.0 % to 65.0 %), (2.0 mm to 1.8mm, 20 % to 30 %), (<1.8 mm, 20 % to 30 %) using test sieves and method described 3.2.3. GMS granules were uniaxially pressed to form GMS green slugs using a 200 tonne uniaxial press to achieve a fired density of 4.4 g/cm^3 to 4.8 g/cm^3. The hydraulic press oil pressure was set at 90 bar (441 MPa of die pressing pressure) and dwell time was set to 1 sec. Pressed to size green GMS slug were fired in a vacuum furnace at 1175 ^{o}C shown Figure 31, under argon purging at 0.8 bar to prevent oxygen reacting with solvent metals to form oxides final discs geometry and mass were: Outside Diameter (OD) 40 mm, Thickness (T) 12 mm and Mass (M) 73 g to satisfy final cubic capsule requirement loaded into the HPHT cubic press.

3.4 Characterisation of seedpad compacts, GMS granules and GMS slugs

Seedpads and GMS granules and slugs were characterised before HPHT synthesis test to ensure they had a desired and consistent quality status.

3.4.1 The density of fired compacts

GSM slugs and seedpads compact density were calculated using obtained mass and dimensions using Equation 32.

$$\text{Density } (\text{g/cm}^3) = \frac{\text{mass (g)}}{\text{volume (cm}^3)} \qquad \text{Equation 32}$$

3.4.2 Inductively coupled plasma spectrometry (ICP)

The Spectro Ciros CCD ICP was used to verify the concentration of solvent metals, monitor trace elements and check for possible contaminations during GMS granules production as per Element Six Pty Ltd specification. A sample of 1.28 g was weighed on a Sartorius scale LP3200 to an accuracy of 0.0001g and added into boiling aqua regia for 30min until all granules dissolved. The solution was filtered through a 541 Whatman filter paper to obtain a clear solution. The filtered solution was introduced into the ICP and results of metal solvents and trace elements concentration were obtained.

3.4.3 Oxygen and carbon analysis

The LECO TC500 Oxygen/Nitrogen Determinator was used for analysing oxygen in GMS fired slugs as per Element Six Pty Ltd specification of less than 150 ppm. Oxygen analysis gave an indication of how much oxygen was present in metal solvents as oxides, oxygen destabilises diamond growth during HPHT diamond synthesis. The graphite crucible was outgassed to ensure there was no was oxygen present, a 0.5 g sample was weighed on a Sartorius scale LP3200 to an accuracy of 0.0001 g and placed in a crucible and heated to 900 ^{o}C at a pressure of 1.5 Bar for 15 minutes under purging helium. Carbon analysis was conducted to verify the amount of graphite in GMS Slug to ensure a correct ratio of graphite to metal solvents was within Element

Six Pty Ltd standard production specification. Carbon analysis was done on a LECO CS200 using Lecocel III and copper accelerator. The sample was prepared by weighing 0.01 g using a Sartorius scale LP3200 to an accuracy of 0.0001g. The sample was placed on the crucible and introduced to a LECO to analyse carbon content.

3.5 High pressure high temperature (HPHT) diamond synthesis

HPHT diamond synthesis using magnesia seedpad and alumina seedpad capsules was conducted at Element Six Pty Ltd using a cubic press Pressure – Temperature diamond synthesis profile and standard operating procedure, at 6.4 GPa and temperature of 1475°C for an hour.

3.5.1 Capsule design for HPHT synthesis

The arrangement for assembling 0.5 mm cubic diamond seeds with magnesia seedpad compact and alumina seedpad compact is shown in Figure 33. Seedpads compacts had five 0.8mm deep holes drilled on one side to place diamond seeds. Two types of tests were employed (i) Unseeded test: diamond seeds were not embedded in the seedpads surface during HPHT synthesis. This test focused on determining stability of magnesia seedpad material and alumina seedpad materials in contact with GMS in the absence of diamond seeds under HPHT synthesis conditions. (ii) Seeded test: diamond seeds were embedded on the surface of the magnesia seedpads compacts and alumina seedpads compacts. This test focused on the comparison of diamond grown from magnesia seedpad and alumina seedpad using HPHT cubic diamond synthesis.

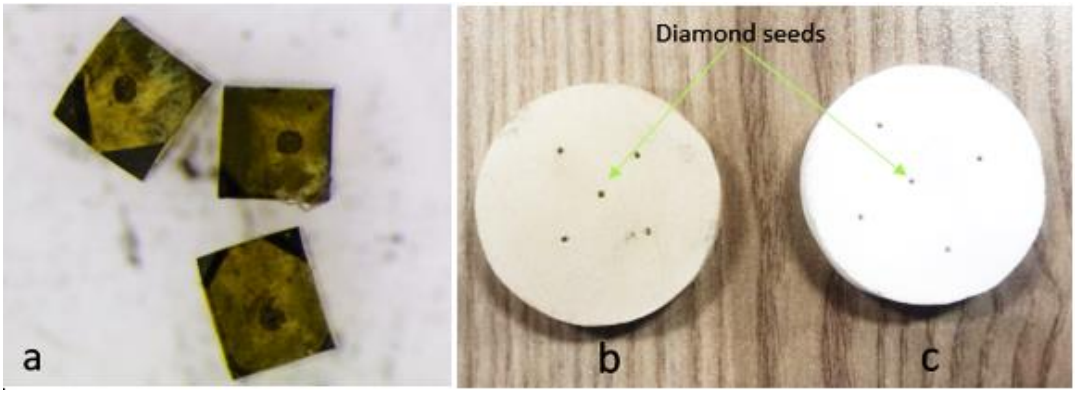

Figure 33 (a) 0.5 mm cubic diamond seeds, 40 mm diameter seedpads compacts with embedded diamond seeds assembly for (b) magnesia seedpad and (c) alumina seedpad.

The GMS slugs were assembled with seedpads as shown in Figure 34, diamond seeds were in contact with GMS slugs.

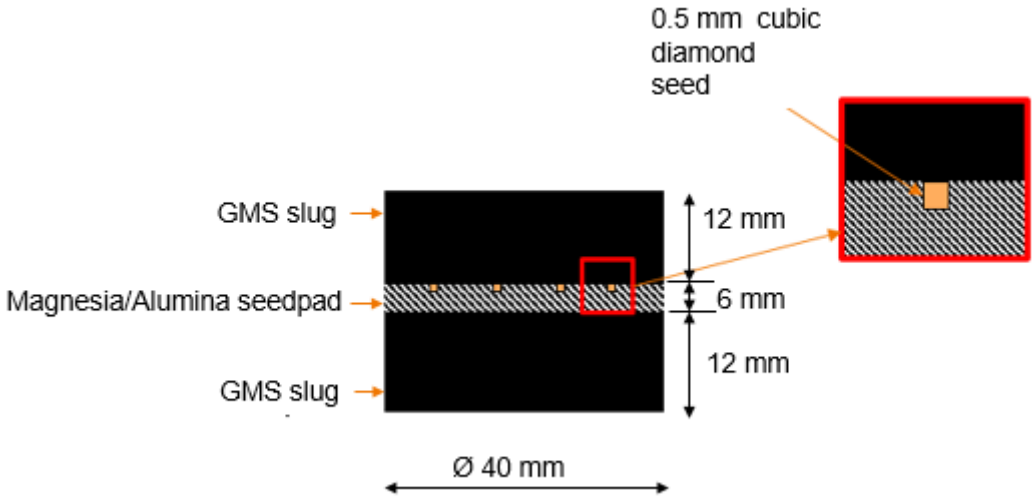

Figure 34 An illustration section view showing the arrangement of seeded magnesia or alumina seedpad and GMS slugs in a capsule.

A 41 mm cubic press capsule in Figure 35 (a) and (b) was used to test seedpads material during HPHT diamond synthesis. The components were conditioned for an hour in an oven in the air at 150 ^{o}C to remove moisture and to prevent thermal shock

that may lead to cracking of capsule components. Magnesia seedpads were further pretreated in a vacuum furnace at 1100 ^{o}C prior to synthesis to reduce metal oxides impurities like iron oxides and magnesium oxides.

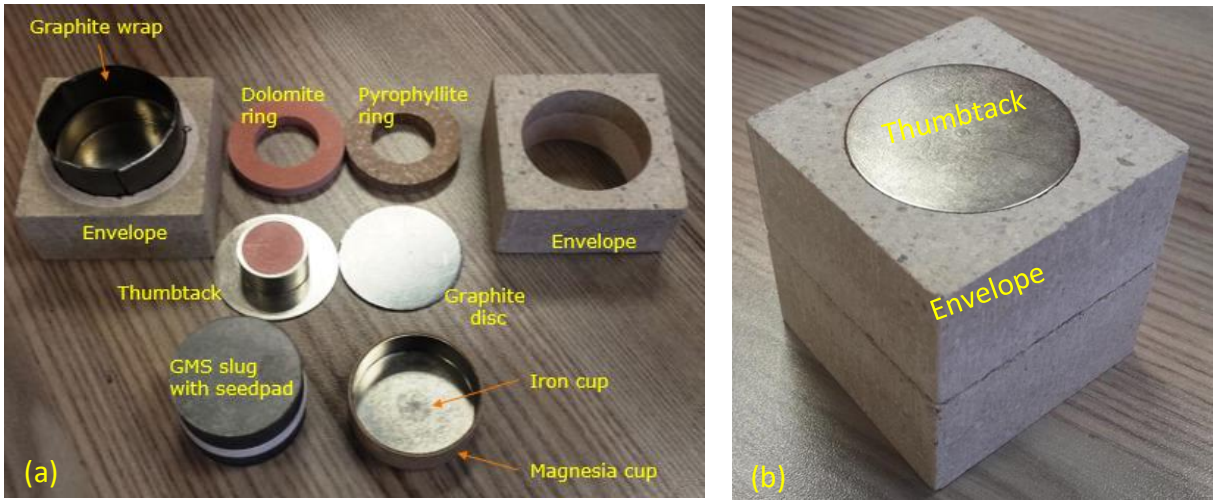

Figure 35 (a) 41 mm cubic capsule components (b) assembled and closed cubic capsule showing outer envelope and a thumbtack metal casing.

The pyrophyllite envelope houses capsule components provide thermal and electrical insulation and form a gasket in-between cubic press anvils during HTHP diamond synthesis. Steel thumbtacks provide an electric current path to the graphite wrap and graphite disc heaters in the capsule. Pyrophyllite rings and dolomite rings were placed into the thumbtacks in this sequence to provide thermal and electrical insulation. Iron cup provided iron source required for diamond synthesis. Magnesia cup provided electrical insulation for the slugs against the heater carrying electrical current.

3.6 Characterisation of HPHT synthesised capsule

Synthesised magnesia seedpad capsule and alumina seedpad capsule components were carefully extracted from the press after HPHT synthesis and characterised to compare the two products. The outer envelopes were examined for physical appearance and measured for extruded gasket size formed. Capsule components thumbtacks and graphite heater were visually checked to examine their physical

appearance. Magnesia seedpads and alumina seedpads were carefully removed from the synthesised capsules for analysis. SEM-EDS was used to examine an unseeded seedpad compacts (without diamond seeds), specifically, the diffusion of graphite and metal solvents (Co, Ni and Fe) into magnesia and alumina seedpad materials were studied. The same was done for the diffusion of magnesia and alumina seedpad material into the GMS slugs. There was very little contrast shown between Co, Fe and Ni due to their proximity on the periodic table of elements, EDS was performed to determine the elemental composition in the slugs. The GMS from seeded capsules were examined using SEM-EDS around the seed position to check for a reduction in graphite concentration due to diamond growth and compare graphite concentration to the GMS slug bulk area. This was to check if graphite diffused into growing diamond during synthesis. Diamonds grown from magnesia and alumina seedpads were examined for colour and morphology using an optical microscope.

Chapter 4: Experimental Results

Experimental results and comparisons for magnesia seedpad and alumina seedpad tests are described in this section using techniques described in Chapter 2 and Chapter 3. For comparison graphs, tables and images were presented side to side to show the results.

4.1 Characterisation of raw magnesia (Nedmag) and raw alumina (KSM99) powders

Particle size distributions for both powders were determined using laser particle diffraction on a Malvern particle size analyser, Mastersizer 2000. Nedmag powder has larger particles with a wider spread and hence lower specific surface area than KSM99 powder shown in Table 7 and Figure 36.

Table 7 Results from Malvern comparing Nedmag and KSM99.

Parameter	Magnesia (Nedmag)	Alumina (KSM99)
D10 (µm)	2.3	0.8
D50 (µm)	23.7	2.4
D90 (µm)	77.9	4.9
Specific surface area (m^2/g)	1.05	3.51

Nedmag and KSM99 particle size distributions in Figure 36 show a bimodal distribution with some small fraction of fines for both Nedmag powder and KSM99 powder.

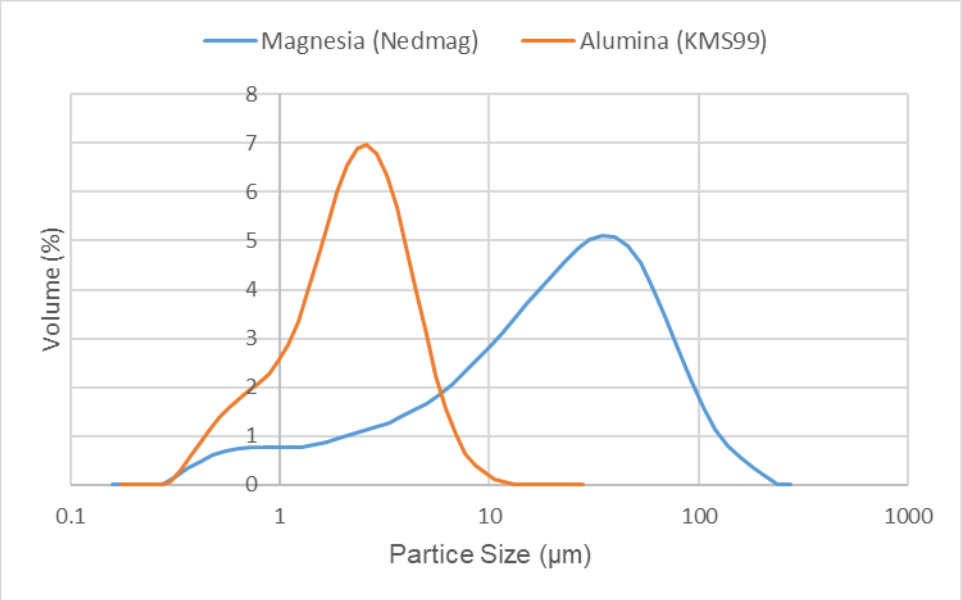

Figure 36 Particle size distribution of magnesia (Nedmag) and alumina (KSM99) powders from Malvern Mastersizer 2000 analyser.

The powder morphology was done using SEM, the results are shown in Figure 37 (a) and (b) for Nedmag and KSM99 powders, respectively. Nedmag particles were irregular shaped, KSM99 particles were plate like shaped. EDS confirms that the particles were magnesia and alumina, respectively.

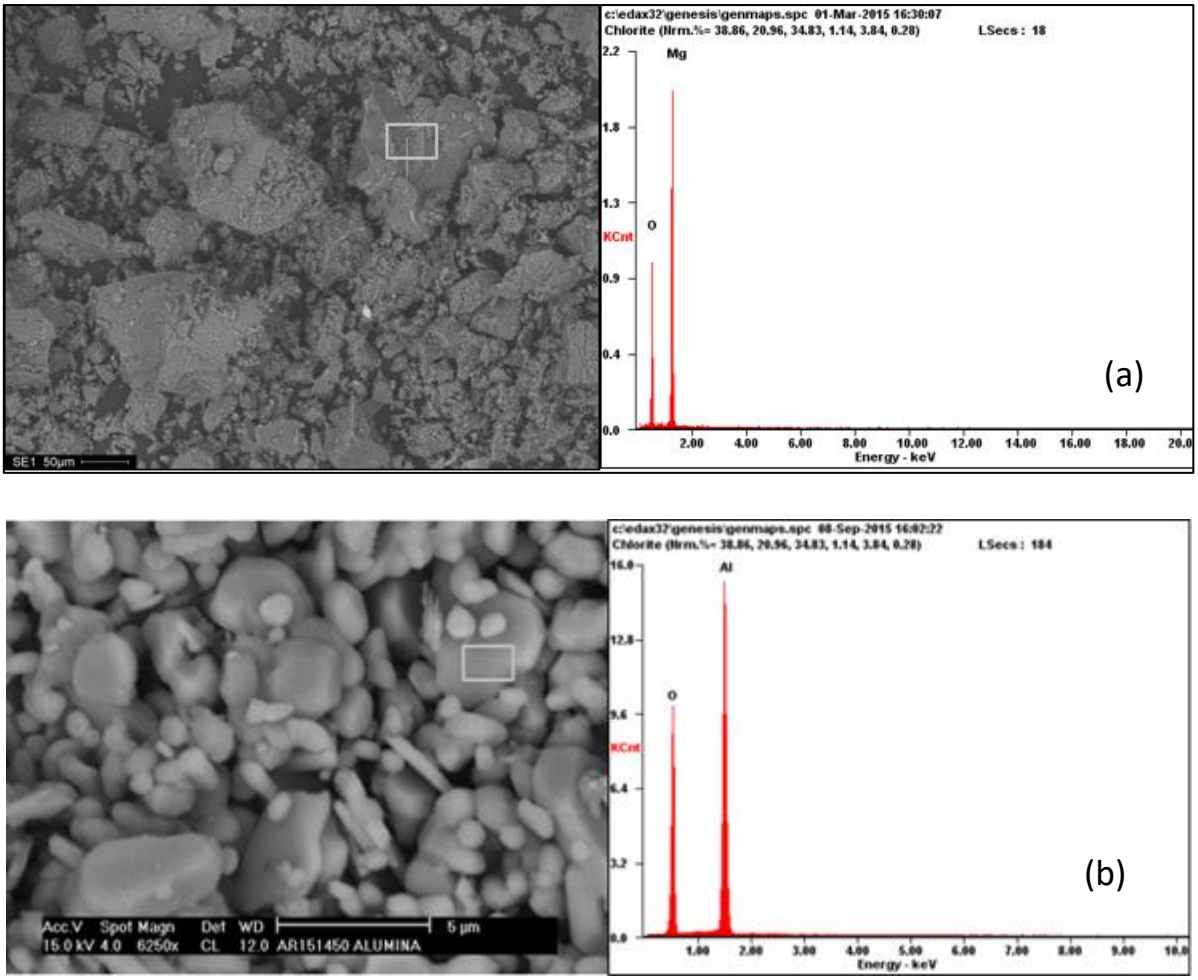

Figure 37 SEM-EDS for (a) magnesia (Nedmag) and (b) alumina (KSM99) powders.

4.2 Magnesia and alumina powders moisture absorption test

The moisture absorption test results from magnesia (Nedmag) and alumina (KSM99) powders in ambient air are shown in Table 8 and graphically in Figure 38. Weekly moisture determination using LOI (wt %) method in a muffle furnace set at 900 ^{o}C in air to ensure volatiles and moisture would leave the sample through decomposition and or evaporation, TGA complemented this test for the same purpose. The ambient air temperature in the laboratory room was monitored using a lab thermometer, fluctuations of 23°C to 25°C were recorded. This ensured the results were not affected by high temperature variations that could further influence the rate of absorption or desorption of moisture in and out of the powders being tested.

Table 8 Moisture absorption test results, measured using LOI (wt %).

Day	1	7	14	21	28	35	42
Magnesia (Nedmag) moisture (wt %)	0.01	0.0500	0.0800	0.0780	0.1000	0.1100	0.1150
Alumina (KSM99) moisture (wt %)	0.01	0.0250	0.0300	0.0500	0.0490	0.0490	0.0510
Conditions	Desiccator	Air	Air	Air	Air	Air	Air
Room Temperature (^{o}C)	25	25	24	23	23	24	24

The test was stopped after alumina had shown constant results, the results showed that the magnesia had a greater moisture uptake of the two powders.

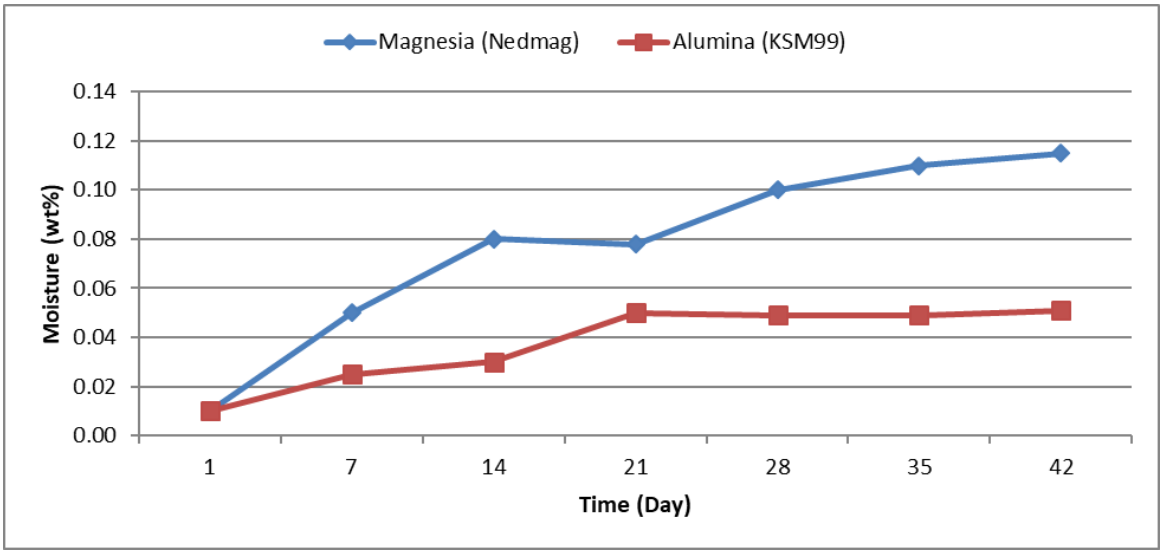

Figure 38 Moisture absorption results for magnesia (Nedmag) and alumina (KSM99).

TGA or thermal analysis gives an insight into the effect temperature has on a sample by monitoring its mass through temperature change. The TGA for magnesia (Nedmag) and alumina (KSM99) powders after the moisture absorption test was conducted in

nitrogen and in synthetic air. TGA graphs for Nedmag and KSM99 as a percentage of mass loss with temperature are shown in Figure 39. The final mass losses were 0.08 % and 0.04 % for Nedmag and KSM99 powders, respectively, indicating a higher mass loss in magnesia powder. The TGA graph for Nedmag in nitrogen and in synthetic air environments did not show similar trends, an indication that an oxidation chemical reaction and material loss in synthetic air was taking place for Nedmag. This was however not observed with TGA graphs for KSM99 in synthetic air and under nitrogen. Mass loss in Nedmag was rapid at the initial stages up to 400 ^{o}C compared to KSM99, this showed magnesia had absorbed moisture more than alumina. There was a sharp drop mass loss in magnesia at 550 ^{o}C, both in synthetic air and under nitrogen in magnesia, this was however not observed in alumina. This was thought to be a decomposition of hydrated water in magnesia, a feature not shown by alumina.

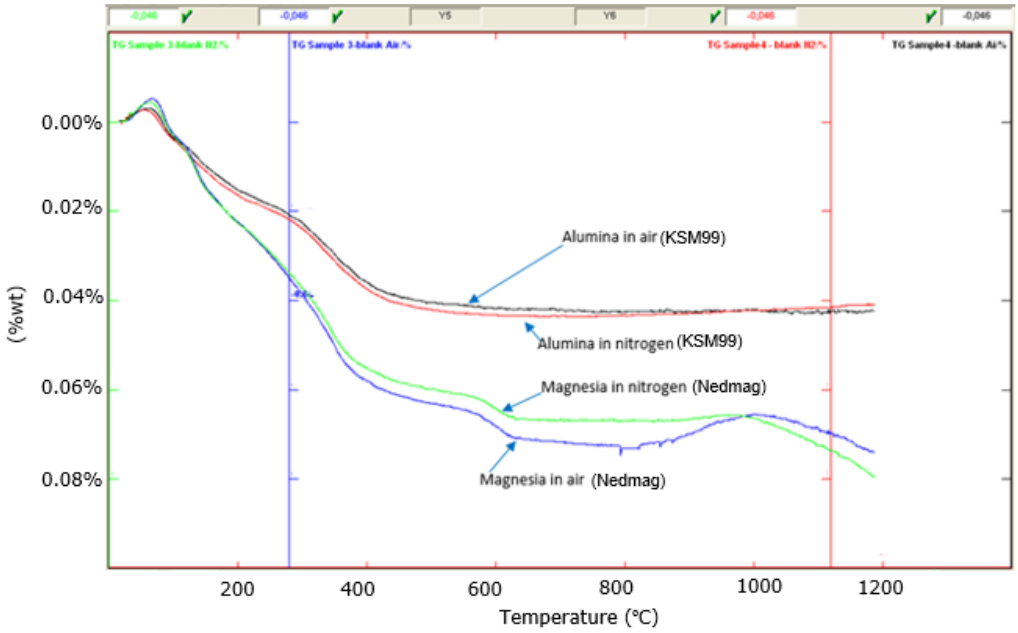

Figure 39 TGA graphs for magnesia (Nedmag) and alumina (KSM99) in synthetic air and nitrogen.

4.3 Characterisation of spray dried magnesia and spray dried alumina powders

Nedmag and KSM99 were raw materials or feedstocks used for spray drying magnesia and alumina, respectively. Spray dried magnesia (and specification) is currently used

for making seedpads compacts at Element Six Pty Ltd, spray dried alumina powder sourced for alumina seedpads test was already spray dried. Spray dried powder characterisation was done to determine the similarity between the spray dried magnesia and spray dried alumina powders and to predict powder behaviour during handling, compacting and firing.

4.3.1 PSD, LOI, moisture and density of powders results

The comparison results for sieve analysis, bulk density, tap density, moisture and LOI are shown in Table 9. The particle size retained from each screen size category, bulk and tap density was comparably closer for the two powders. This led to the flowability of the two powders to be within the specification of the Carr compressibility index and Hausner ratio of less than 15 % and less than 1.18, respectively. This indicated that both powders would be free flowing during powder handling at uniaxial pressing.

Table 9 Spray dried magnesia and spray dried alumina powders characterisation.

		Specification	Spray dried Magnesia	Spray dried Alumina
Screen Size (µm)	+500 (wt %)	0.0 - 0.5	0	0.01
	-500 to +300 (wt %)	2.0 - 16.0	6.63	9.04
	-300 to +125 (wt %)	42.0 - 77.0	74.56	76.81
	-125 to +45 (wt %)	7.0 - 41.0	17.3	13.59
	-45 (wt%)	4.5 - 9.5	1.1	0.37
Bulk density (g/cm^3)		1.10 -1.30	1.15	1.12
Tap density (g/cm^3)		1.23 -1.48	1.25	1.22
Carr compressibility index (%)		< 15.0	8.7	8.9
Hausner Ratio		<1.18	1.1	1.1
Moisture (wt %)		0.6 -1.0	0.5	0.4
LOI at 900°C (wt %)		2.2 - 4.5	3.4	3.1

The fractions obtained from sieve analysis of magnesia and alumina spray dried powders were similar and followed a normal distribution, as shown in Figure 40. The settling and positioning of powders in die cavity during uniaxial compacting of seedpads compacts was predicted to be similar.

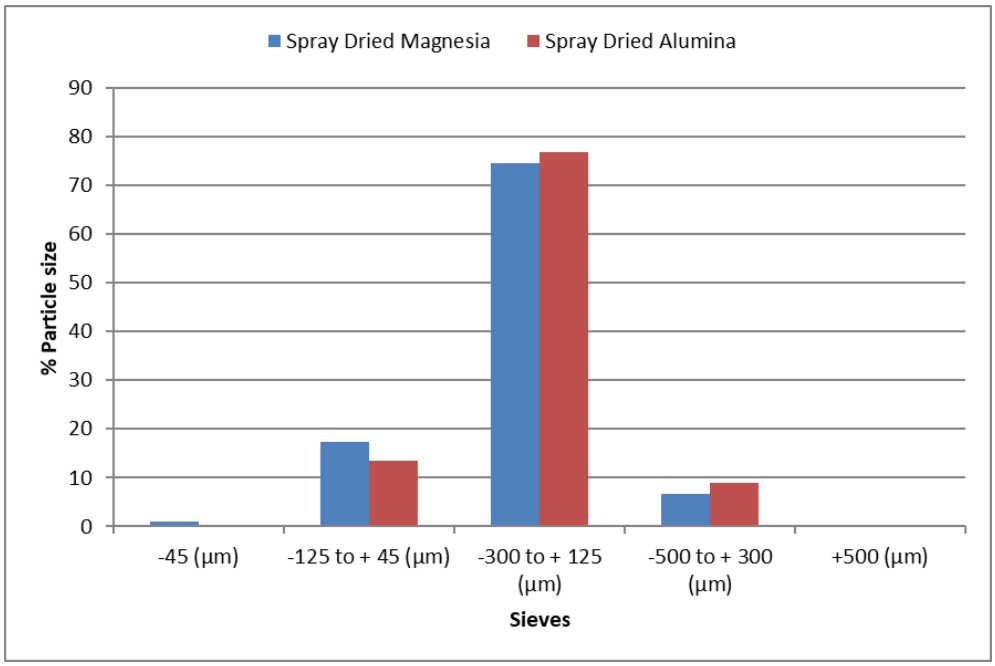

Figure 40 Particle size distribution of spray dried magnesia and spray dried alumina.

The LOI and moisture content of the two powders are comparable, an indication of similar behaviour during uniaxial compaction of the two powders. Mass loss from green state to fired state may be slightly more for magnesia due to a slightly higher LOI value, higher value in magnesia may be due to higher binder contents added or hydrated moisture.

4.3.2 Powder particle morphology

Spray dried magnesia and spray dried alumina powders were analysed for particle morphology using SEM, the results are shown in Figure 41 (a) and (b). Both powders had spherical shaped granules, the shape indicated they would flow easily. The surfaces of spray dried magnesia granules seemed to be rougher than that of spray

dried alumina. This might be due to the coarser grains used for spray drying magnesia compared to finer grains used for spray drying alumina or spray dry conditions, slurry viscosity, flow rate, temperature, pressure in the spray drying process. Some of the alumina granules seem to be hollow, an undesirable property for materials formed by powder compaction. The holes may translate to pores in the compacts and manifest as points of crack initiation.

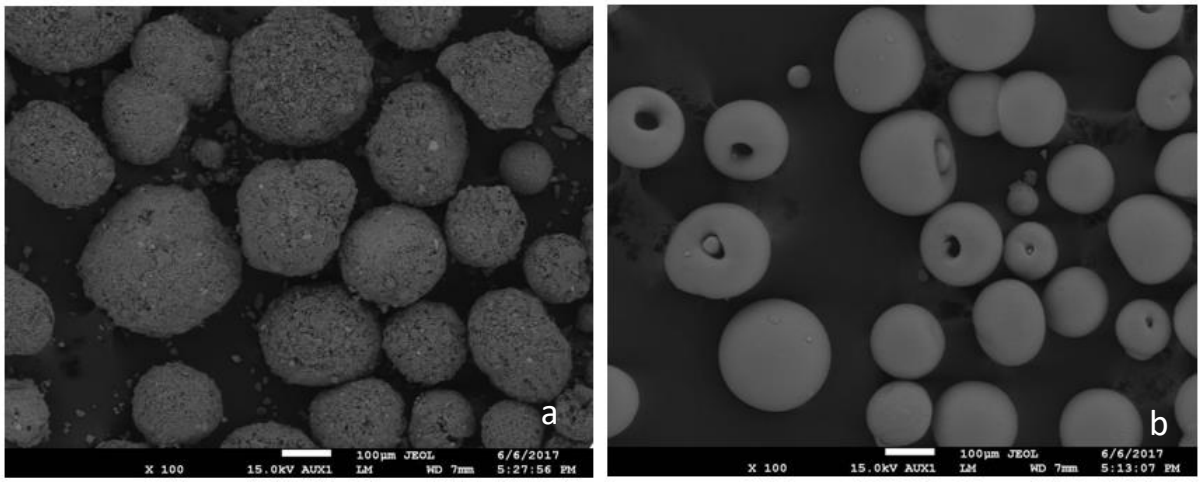

Figure 41 SEM images of (a) spray dried magnesia powder and (b) spray dried alumina powder.

4.3.3 XRD and XRF powder results

Powder XRD was done to verify phases present in the spray dried powders. Some impurities that could not be detected by XRD because of detection limitations on XRD of 1-3 % [61] were detected through XRF. Magnesia powder XRD results shown in Figure 42 identified the phases in the powder as MgO, CaO, SiO_2 and MnO.

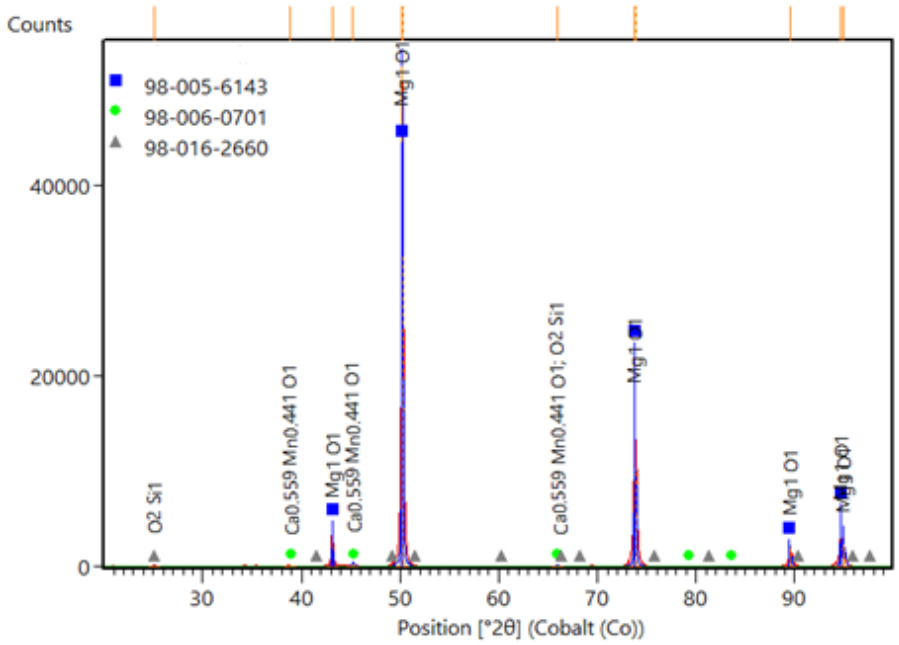

Figure 42 XRD for spray dried magnesia powder.

The XRD traces for spray dried alumina powder in Figure 43 shows pure alumina and no other phases were identified. This shows alumina powder obtained was qualified as pure material for alumina seedpads compacts manufacture, the desired property for diamond synthesis.

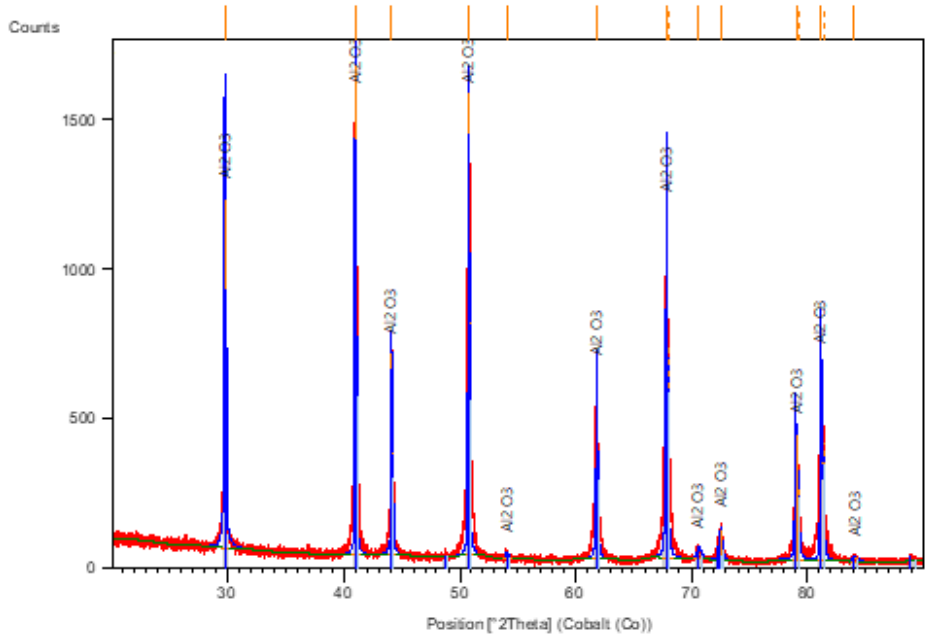

Figure 43 XRD for spray dried alumina powder.

XRF of powders was done using the PW2000 XRF machine. The results in Table 10 (a) and (b) show that magnesia had some impurities whilst alumina did not show any presence of impurities. Phases identified in magnesia powder were MgO and impurities MnO_2, Fe_2O_3, CaO, and SiO_2. The spectra peaks showing impurities from XRF are included in appendix A, Figure A2 and Figure A3.

Table 10 (a) spray dried magnesia and (b) spray dried alumina XRF results.

(a) Spray Dried Magnesia	
Compound	Concentration (%)
MgO	94.359
SiO_2	0.39
CaO	2.991
MnO_2	0.258
Fe_3O_2	2.001

(b) Spray Dried Alumina	
Compound	Concentration (%)
Al_2O_3	100

4.4 Manufacture of magnesia seedpads and alumina seedpads compacts

A uniaxial press was used to prepare magnesia and alumina seedpads compacts. The outside diameter (OD), thickness and mass of seedpads were measured to determine green and fired densities detailed in Appendix B, Tables 17 and 18. Figure 44 shows the average fired densities attained as a function of applied compaction pressure. Three samples per compaction pressure were measured. A desired fired density of 70 – 80 % was obtained at a pressure of 539 MPa for magnesia seedpads. Alumina seedpads required a higher pressure to achieve a fired density above 60 %. Alumina green seedpads compacts started to form some cracks above 735 MPa and hence pressure increase was stopped.

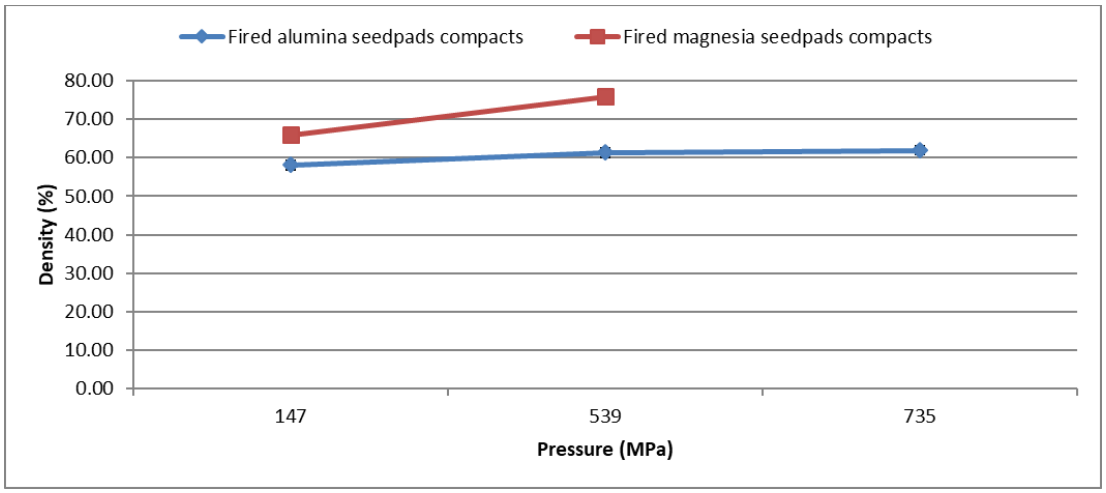

Figure 44 Density vs pressure of fired magnesia seedpads compacts and alumina seedpads compacts.

Fired seedpads compacts were checked for phases present using XRD, magnesia seedpad compact traces in Figure 45 shows the presence of impurities manganese oxide and calcium oxide, undesirable compact purity for diamond synthesis.

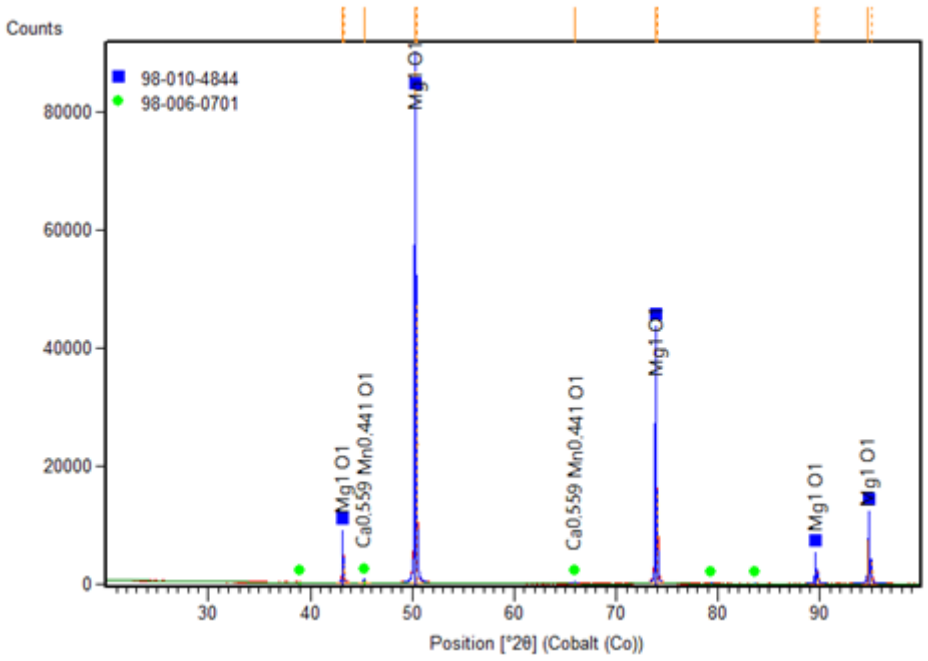

Figure 45 XRD for fired magnesia seedpad compacts.

The XRD traces for fired alumina seedpad compact in Figure 46 shows only alumina phases and no other phases were identified. This showed evidence of high purity fired alumina seedpads compacts, a desirable compact purity for diamond synthesis.

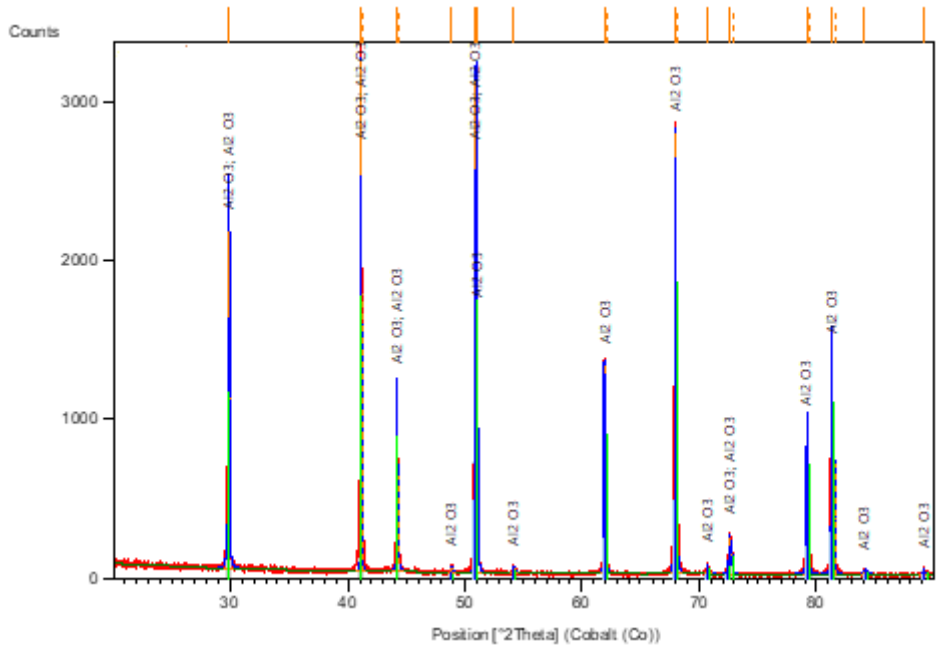

Figure 46 XRD for fired alumina seedpad compacts.

4.5 Compressive fracture strength test for magnesia and alumina

Compressive fracture strength tests for fired magnesia and alumina compacts were conducted to compare the behaviour of magnesia cylindrical compacts and alumina cylindrical compacts under compressive force. This test predicted fracture strength behaviour of seedpads compacts during handling and under initial cubic press compressive forces. The tests were done on an Instron test rig shown in Figure 47 at 1 mm/min displacement rate until fracture occurred. The fracture strength test results are tabulated in Appendix C Table 19 and Table 20, magnesia compacts and alumina compact samples showed a fair degree of variability in that property.



Figure 47 Test sample under the Instron test rig.

Magnesia compacts and alumina compacts fractured in a manner shown in Figure 48 (a) and (b), respectively. Cones were formed at the ends of fractured samples and this showed the samples failed in a shear mode.

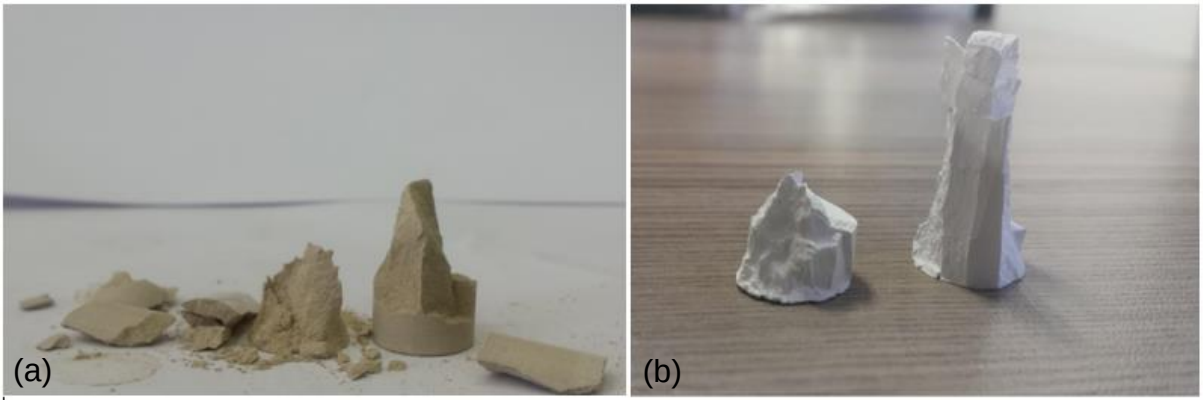

Figure 48 Fractured samples of (a) magnesia compact and (b) alumina compact.

Figures 49 and Figure 50 show the graphs of compressive stress vs strain during testing for the lowest, highest and average strength of magnesia and alumina compacts samples.

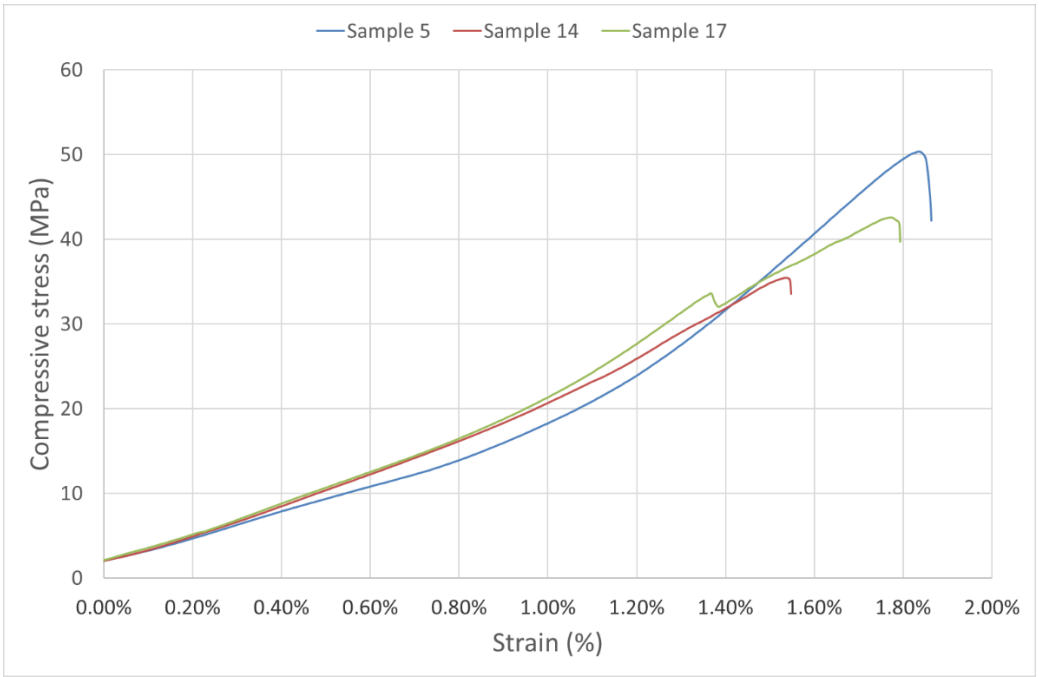

Figure 49 Magnesia compacts compressive stress-strain graph.

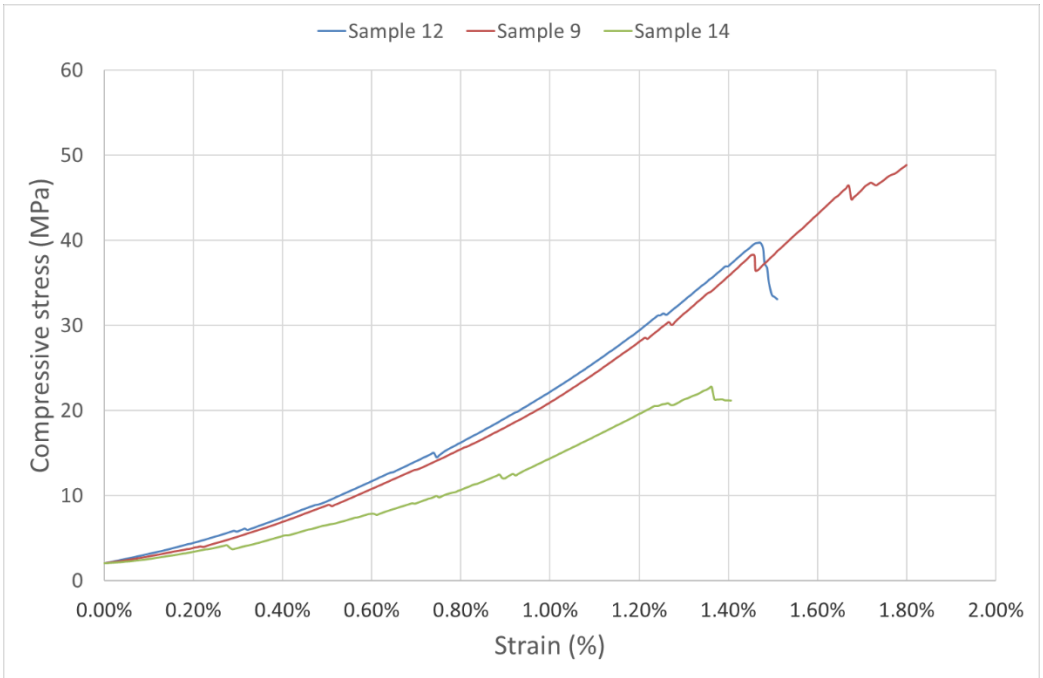

Figure 50 Alumina compacts compressive stress-strain graph.

The box plots in Figure 51 shows that the compressive fracture strength of magnesia and alumina samples were comparable, although alumina shows a wider distribution.

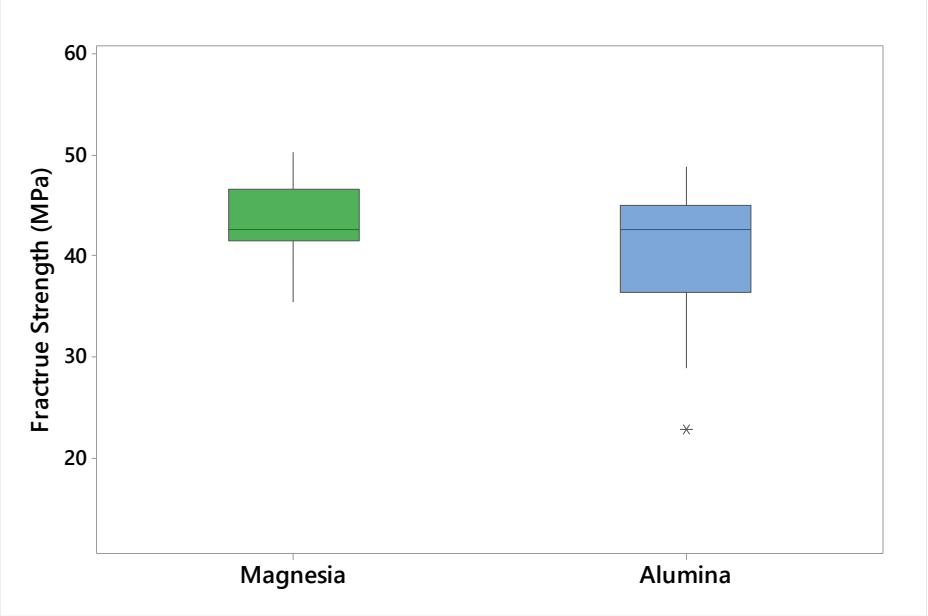

Figure 51 Compressive fracture strength of magnesia and alumina compacts box plot.

Figure 52 shows the density of magnesia compacts was higher than the density of alumina compacts. Alumina compacts were more porous than the magnesia compacts as indicated by the percentage of theoretical density of the two compacts.

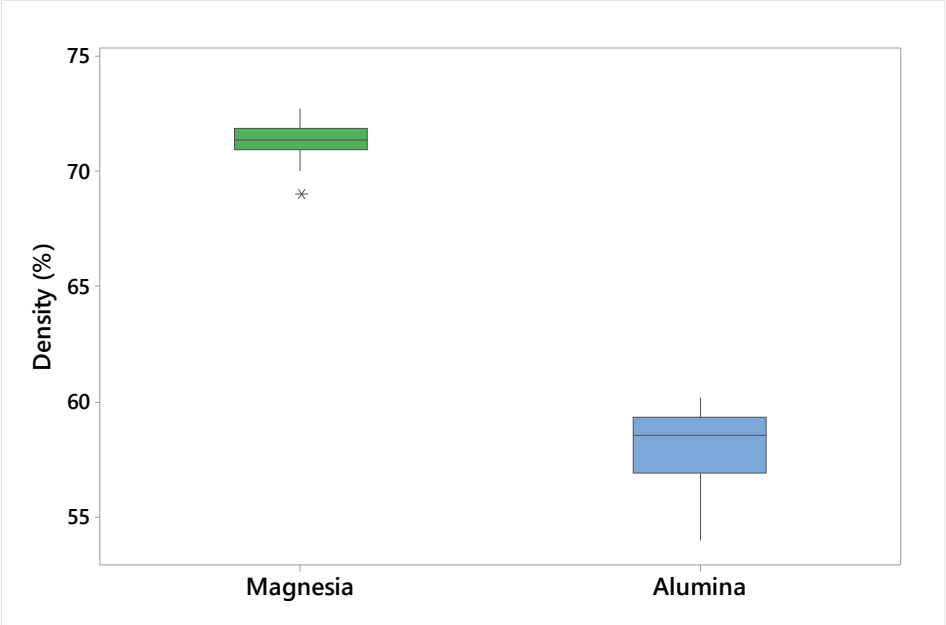

Figure 52 % density of magnesia compacts and alumina compacts.

Weibull parameters were determined for magnesia and alumina compacts using the gradient of the fitted lines in Figure 53 was obtained from the data set in Appendix C Table 21. The Weibull modulus was 6.35 for alumina, smaller than that of magnesia 13.33.

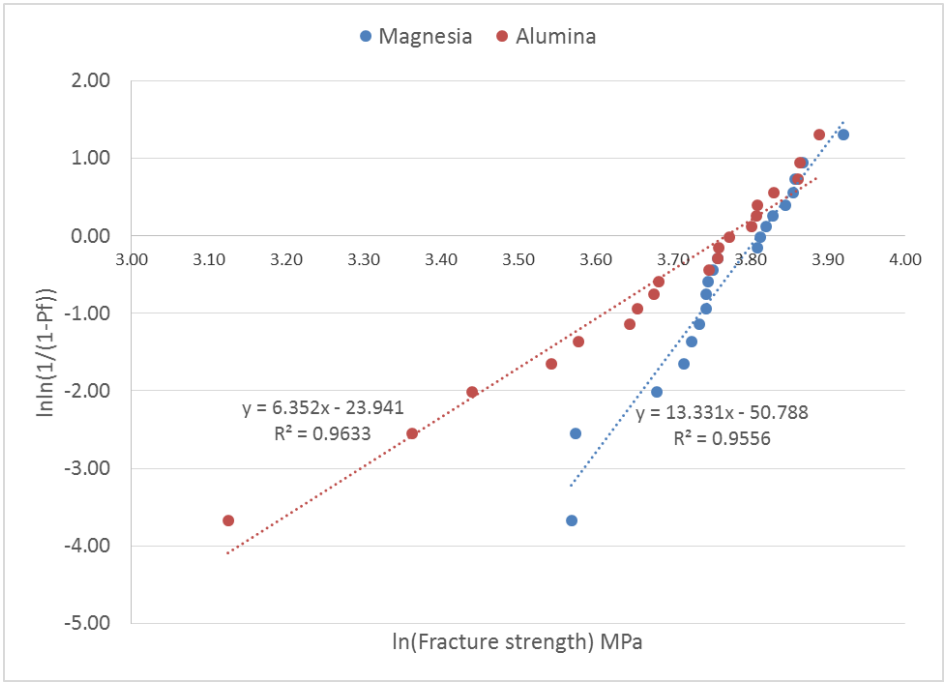

Figure 53 Weibull parameter determination graph.

The characteristic strengths of magnesia compacts and alumina compacts were obtained from the graphs in Figure 53, by finding the value of ln(Fracture strength) on the x-axis for which lnln(1/(1-P*f*)) on the y-axis is zero. The characteristic strength together with a summary for compressive test data obtained from Appendix D Table 22 is shown in Table 11.

Table 11 Summary of magnesia and alumina fracture strength results.

Material	Weibull Modulus	Characteristic fracture strength (MPa)	Average fracture strength (MPa)	Standard deviation fracture strength (MPa)
Magnesia	13.33	45.81	43.45	3.86
Alumina	6.35	43.82	40.30	6.38

The Weibull analysis confirms that alumina is stronger enough to hold during capsule assembly and cubic press initial compaction. It is important for diamond seed carrying seedpad to withstand capsule building and initial press compressive forces to prevent falling apart as seeds are needed to maintain set orientation and spatial arrangement.

4.6 Manufacture of GMS slugs

Element Six Pty Ltd production procedure was used to prepare GMS slugs. The granules produced shown in Figure 54 were used for uniaxial pressing GMS slugs.

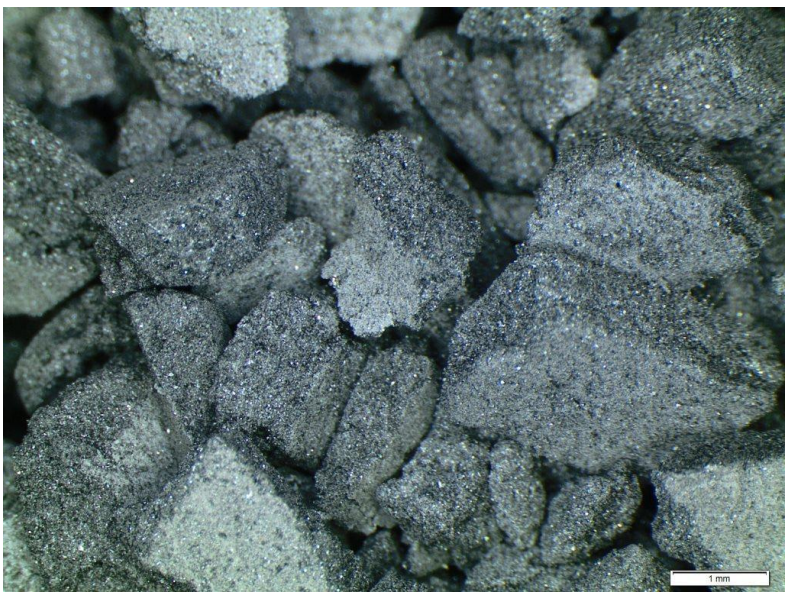

Figure 54 GMS granule particles used for uniaxial pressing GMS slugs.

The GMS granules SEM-EDS in Figure 55 was done to understand solvent metals and graphite positions in the matrix,

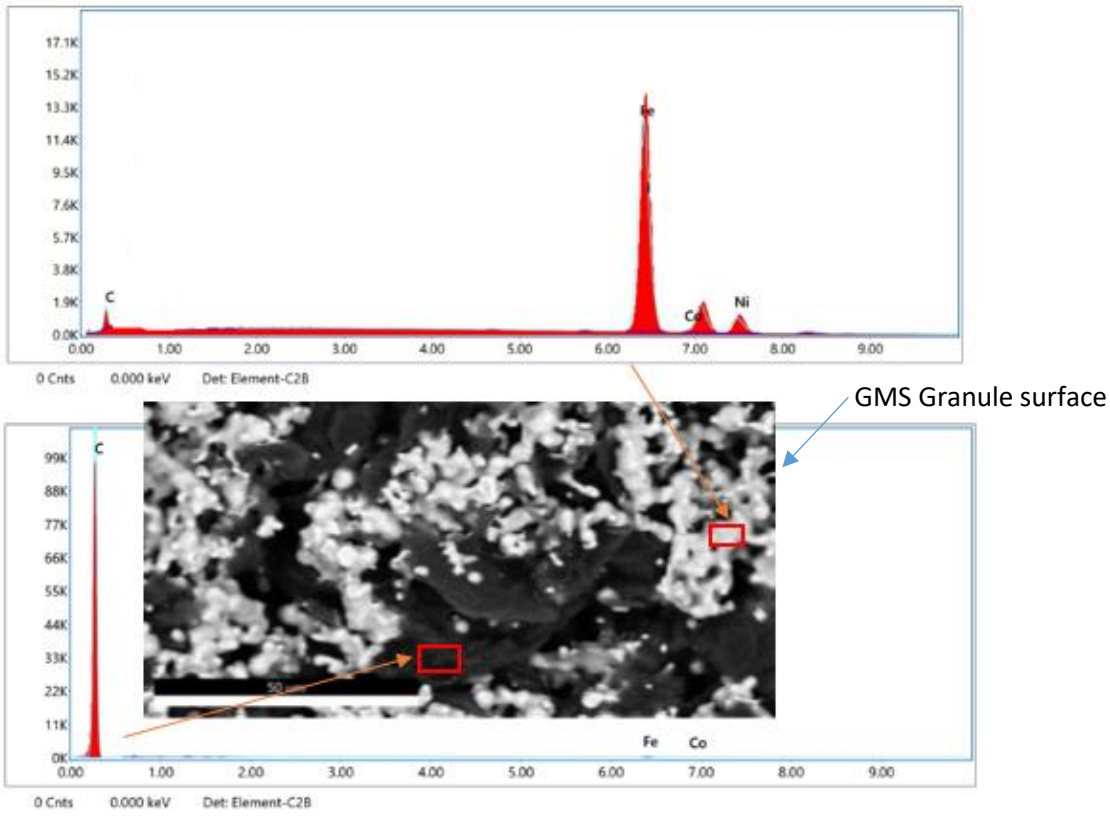

Figure 55 SEM-EDS of a GMS solvent granule surface showing graphite and metal solvents distribution.

Pressing of GMS granules was done using a uniaxial press, the hydraulic oil pressure was set at 90 bar translating to a die pressure of 441 MPa. Green compacts were fired in a vacuum furnace with argon purging to obtain slugs compacts fired density shown in Tables 12 and 13, respectively.

Table 12 Results of green GMS slugs.

Outside diameter	Thickness (mm)	Mass (g)	Density (g/cm^3)
39.40	12.58	73.27	4.78
39.41	12.57	73.22	4.78
39.41	12.57	73.20	4.78
39.41	12.57	73.20	4.78
39.44	12.59	73.18	4.76
39.44	12.59	73.19	4.76

Table 13 Results of fired GMS slugs.

Outside Diameter	Thickness (mm)	Mass (g)	Density (g/cm^3)
39.48	12.73	73.02	4.69
39.42	12.71	73.06	4.71
39.47	12.80	73.13	4.67
39.46	12.72	73.07	4.70
39.46	12.73	73.09	4.70

4.7 HPHT Diamond synthesis results

The diamond synthesis involved assembling seedpad, GMS slugs and capsule components from Figure 35. Capsule components were selected to ensure mass and dimensions were fairly similar for both magnesia seedpad capsules and alumina seedpad capsules. Capsules were assembled to specified mass and height before loading into a cubic press. Table 14 shows mass and dimensions obtained after assembling cubic capsule envelopes.

Table 14 Magnesia seedpad capsule and alumina seedpad capsule.

Capsule parameter	Magnesia seedpad capsule	Alumina seedpad capsule
Mass	657.31 g	658.6 g
Height	61.37 mm	61.45 mm
Length and Width	60 mm x 60 mm	60 mm x 60 mm

4.7.1 Cubic synthesis test using seedpads without diamond seeds

The first test conducted was to test the stability of GMS and a blank seedpad (seedpads without diamond seeds) under HTHP diamond synthesis condition. A cubic press selected was used for both magnesia seedpad capsules and alumina seedpad capsules in order to minimise press to press variability. Table 15 shows the press parameter results were similar for both magnesia and alumina seedpad-containing capsules. The press process control parameters load, anvil-to-anvil, electrical resistance, final distance and maximum applied pressure did not show major differences. The resistance generated by both runs was similar but it was slightly higher in the case of alumina.

Table 15 Cubic press feedback results for HPHT synthesis.

	Press No.	Run No.	Max of power (W)	Max Pressure (GPa)
Alumina	1120	8965	7051	6.4
Magnesia	1120	8966	7035	6.4

Pyrophyllite envelope gasket formation after synthesis was examined to determine anvil penetration. The physical appearance and thickness of the pyrophyllite gasket in Figure 56 were 4.6 mm for both the alumina and magnesia seedpads capsules. The external visual appearance of the two capsules looked similar with no visible cracks

observed on either of the capsule envelopes. No differences were observed between the magnesia and the alumina capsule components used for the test.

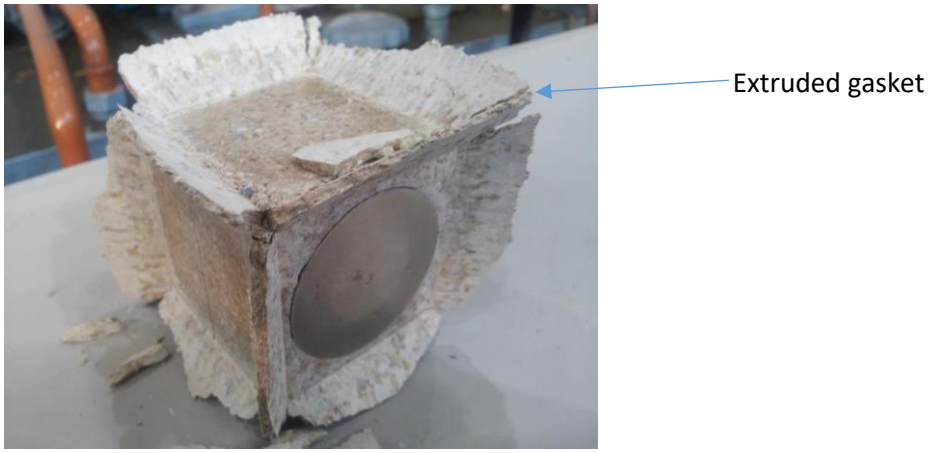

Figure 56 Pressed cubic capsule showing self-extruded gasket and metal casing disc from a thumbtack.

Magnesia seedpad compact and alumina seedpad compact surfaces were both coated by a black material that was thought to be graphite. Figure 57 shows (a) alumina seedpads and GMS slugs, (b) magnesia seedpads and GMS slugs capsule before HTHP diamond synthesis, (c) alumina seedpads and (d) magnesia seedpads after HTHP synthesis.

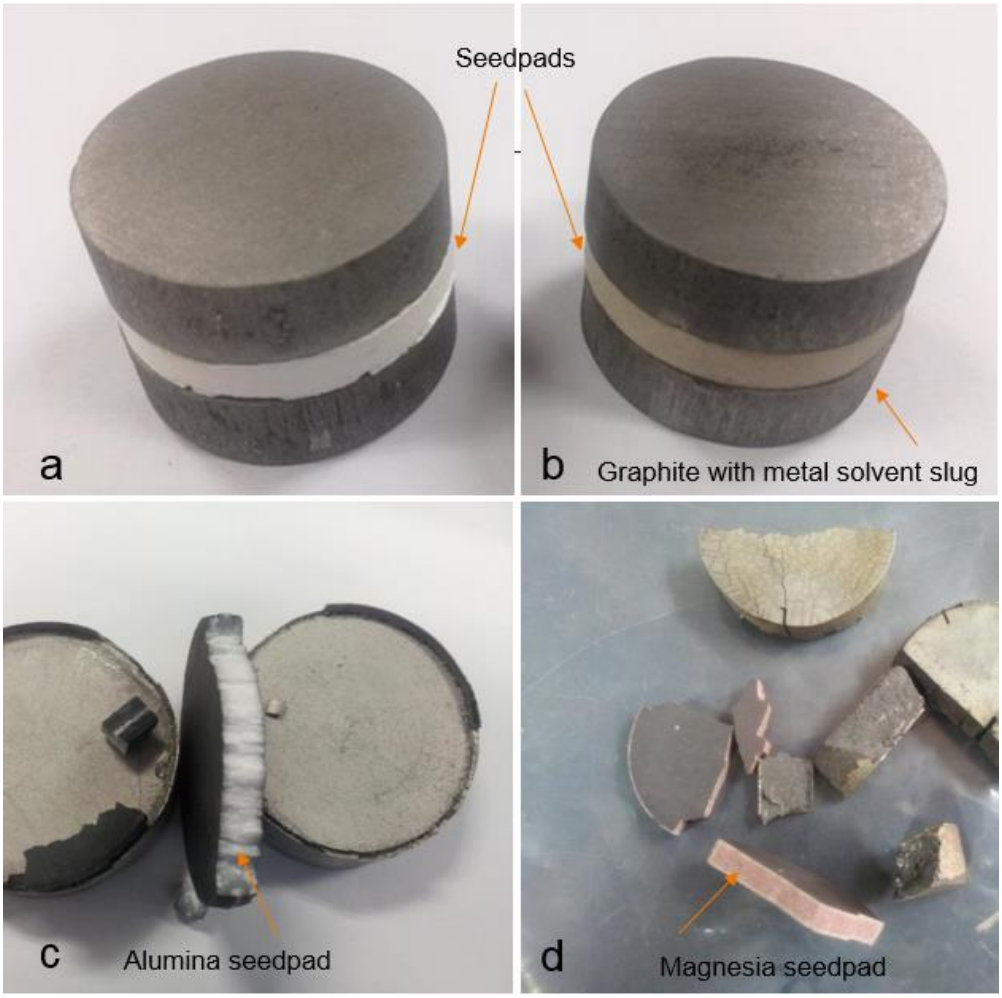

Figure 57 (a) and (c) alumina seedpad before and after HTHP synthesis, (b) and (d) magnesia seedpad before and after HPHT synthesis.

4.7.2 SEM-EDS profile of seedpads and GMS slugs

Microstructures of GMS slugs, magnesia seedpad and alumina seedpad after HTHP synthesis, were prepared examined under the SEM to compare the physical appearance of grains and to obtain EDS profile after HPHT synthesis. The microstructures obtained are shown in Figure 58 and they revealed sintering with some extent of grain growth for both magnesia and alumina.

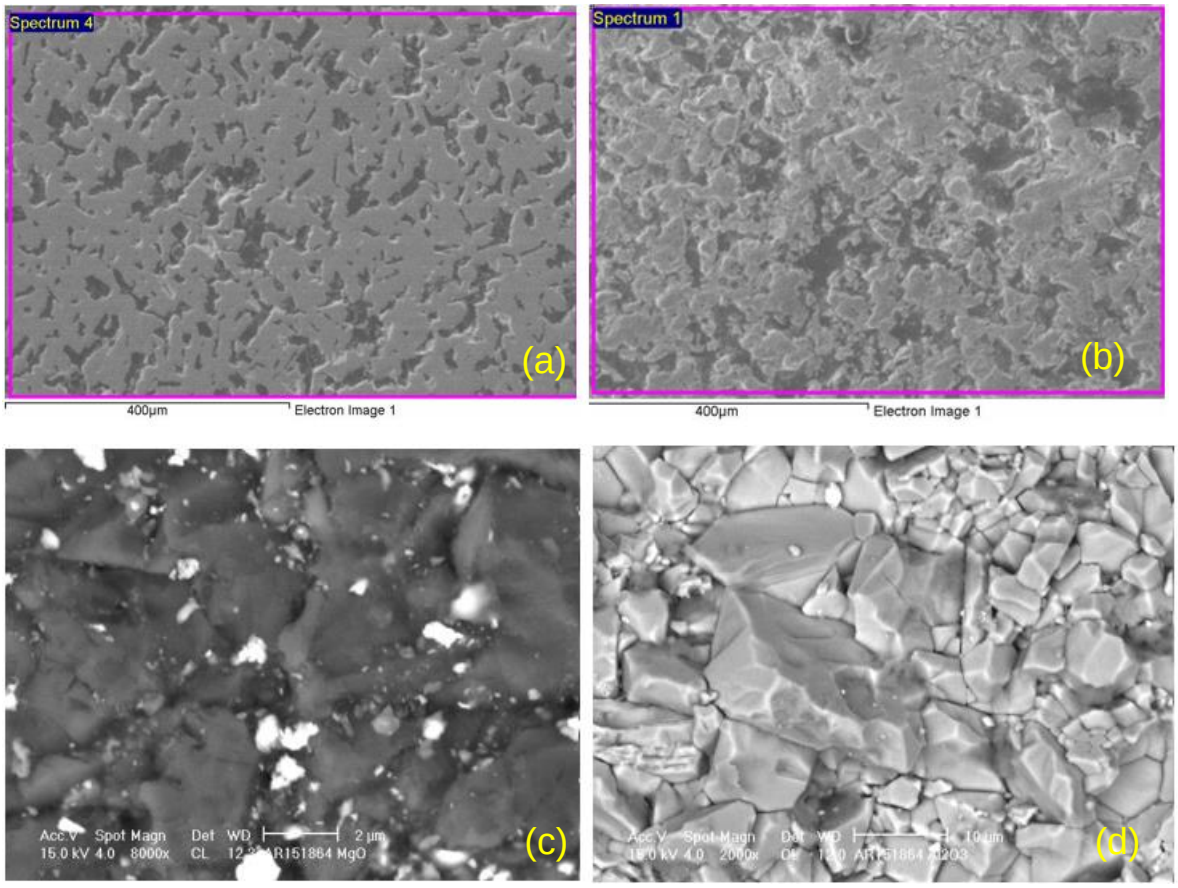

Figure 58 SEM images of (a) GMS slug for magnesia seedpad, (c) magnesia seedpad, (b) GMS slug for alumina seedpad, (d) alumina seedpad after HPHT synthesis.

Seedpads were in contact with GMS during HPHT, there should be very limited or no diffusion of seedpad material into GMS slug material, and GMS slug material should not diffuse into seedpads material during HPHT diamond synthesis. The diffusion to either side will cause destabilisation of GMS slug constituent's concentration (C, Co, Ni and Fe) required for diamond growth. EDS profile measured the concentration of elements present in the samples analysed. EDS profiles were done to check diffusion of seedpad material into the GMS slug and to check GMS slug (C, Co, Ni and Fe) diffusion into seedpad after HTHP synthesis. EDS profiles were obtained from images shown in Figure 58 (i) through GMS slugs (a) interface of GMS slugs and magnesia (a)-(c) to magnesia seedpad (c) (ii) through GMS slugs (b) interface of GMS slugs and alumina (b)-(d) to alumina seedpad. These were magnesium (Mg), aluminium (Al), nickel (Ni), iron (Fe), and cobalt (Co) Table 22 in Appendix D.

The concentration of magnesia and alumina seedpads material in GMS slugs results are shown in Figure 59. Neither magnesia nor alumina traces were found in the GMS slugs after synthesis. This shows that both types of seedpad material could not diffuse into respective GMS slugs during HPHT synthesis. Distance 0.000µm represents seedpad-GMS slug interface.

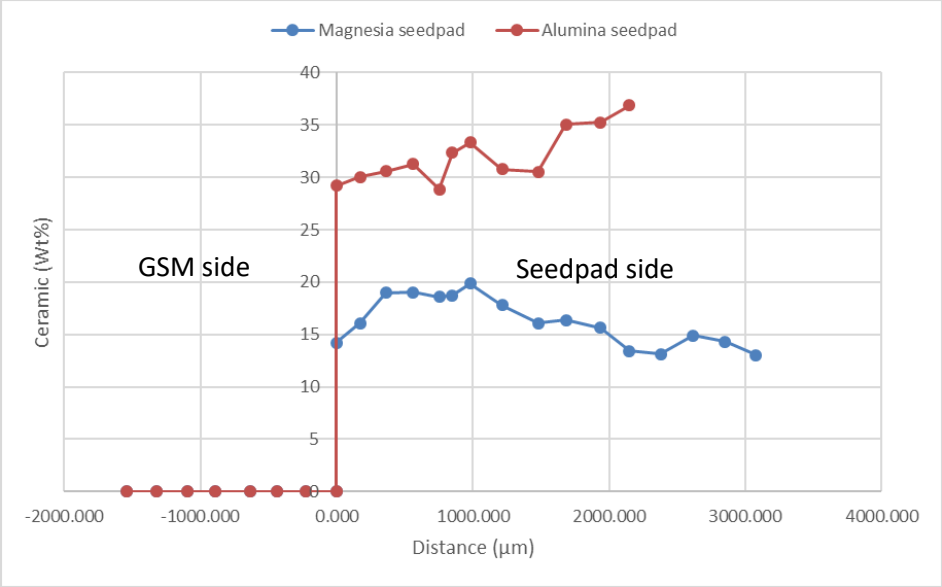

Figure 59 % weight concentration of magnesia and alumina through the GMS slugs and through the magnesia seedpad or alumina seedpad interface.

Iron from GMS slugs in Figure 60 did not diffuse into magnesia or alumina seedpads, however, some traces of iron were found in the magnesia seedpads material in small amounts less than 1% weight as stated in the Nedmag powder specification. This is an indication of Fe present in the starting magnesia powder.

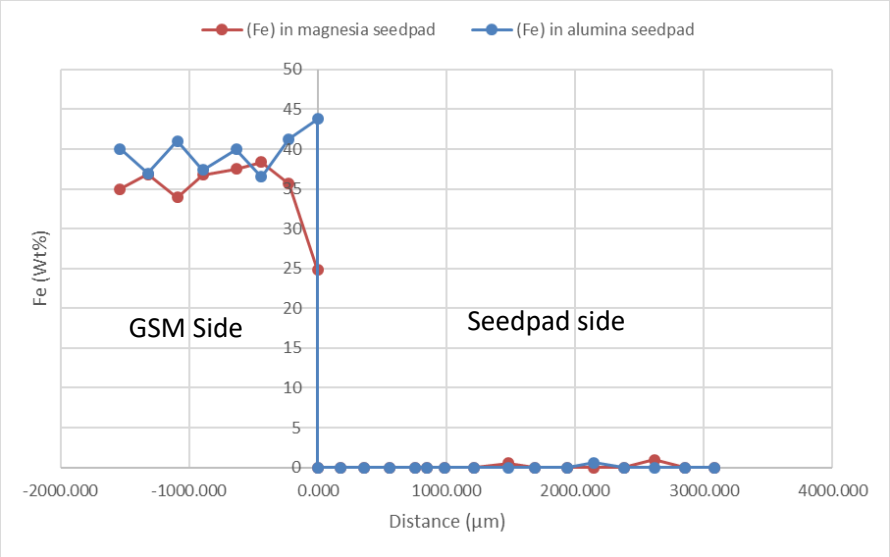

Figure 60 % weight concentration of iron through the GMS and magnesia seedpad or alumina seedpad interface.

Nickel from GMS slugs did not diffuse into magnesia seedpads and alumina seedpads, shown in Figure 61.

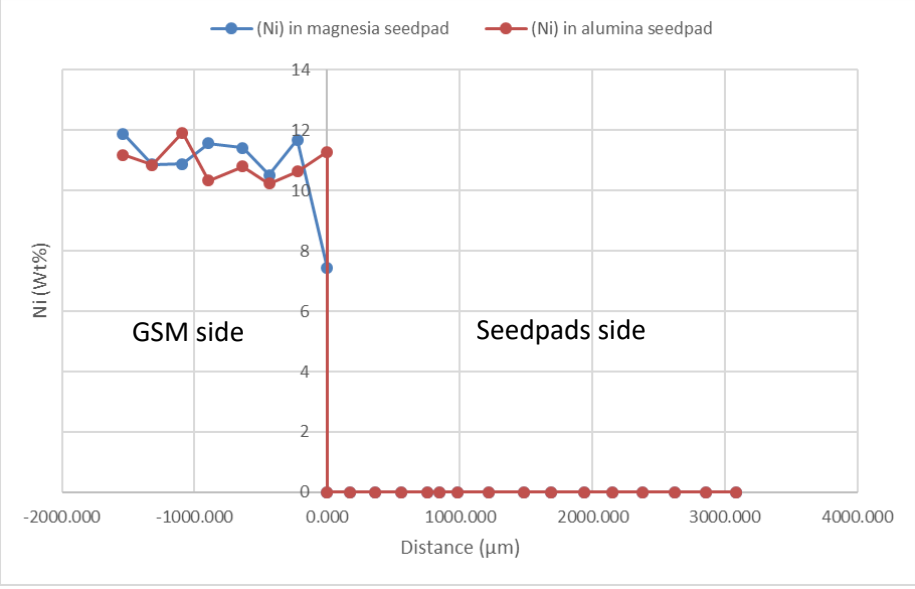

Figure 61 % weight concentration of nickel through GMS slugs and magnesia seedpads or alumina seedpad interface.

4.7.3 Diamond synthesis at HPHT

Magnesia seeded seedpads and alumina seeded seedpads were introduced for second HPHT synthesis test to compare morphology and colour of diamond synthesised from the current magnesia seedpads used at Element Six Pty Ltd and test alumina seedpads. Diamond synthesised from both seedpad compacts had a similar physical appearance of yellow colour and cubic shape shown in Figure 62 (a) and (b).

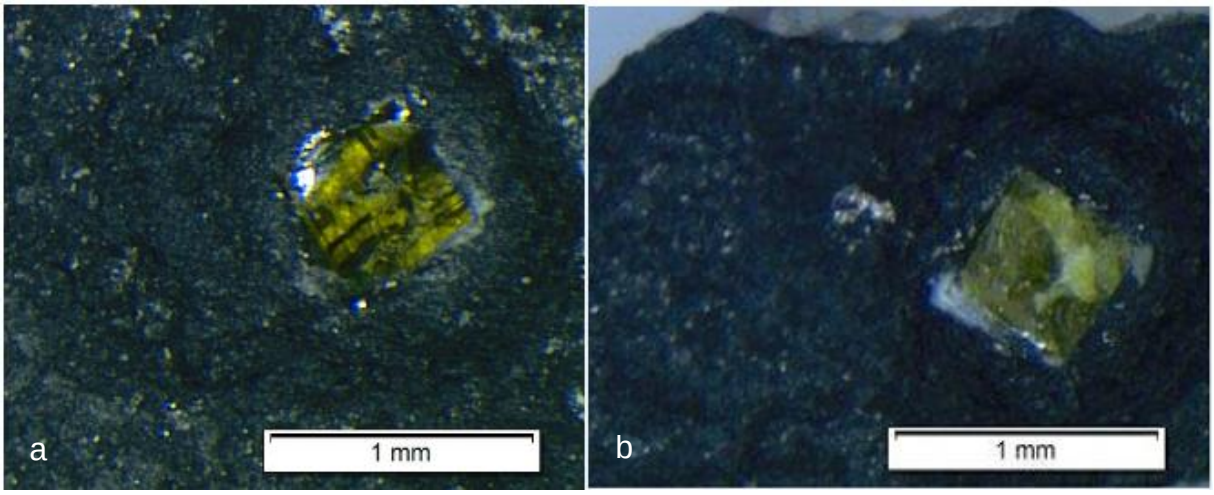

Figure 62 Diamond synthesised from (a) magnesia seedpads (b) alumina seedpads.

Diamonds grew due to their intimate contact with the GMS slugs at HTHP diamond synthesis conditions. The SEM of polished GMS slugs from magnesia and alumina capsule samples from the material adjacent to the grown diamond in Figure 63, shows that the carbon (graphite) concentration was reduced near the synthesised diamond site because graphite was converted to a diamond as it grew. The carbon (graphite and diamond) appear darker than solvent metals due to their atomic weight differences. Graphite appears in the bulk of slugs as pockets of darker area.

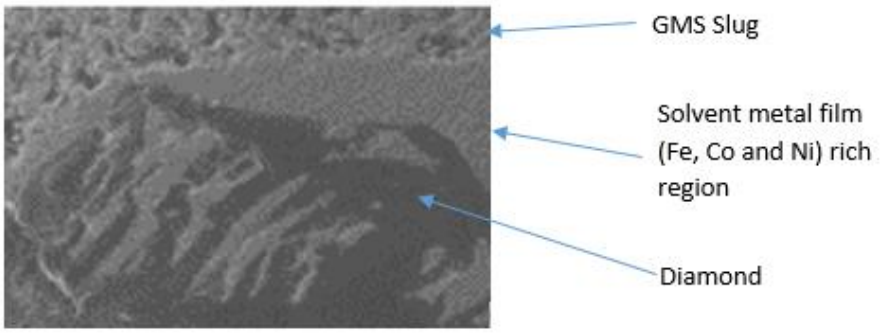

Figure 63 Section of GMS slug and solvent metal film region surrounding the synthesised diamond.

Chapter 5: Discussion

5.1 Moisture absorption by magnesia and alumina ceramics

Magnesia seedpads moisture absorption ability at ambient conditions and the low purity of magnesia used at Element Six Pty Ltd are undesirable characteristics for HPHT diamond synthesis. Ceramic moisture removal prior to HPHT diamond synthesis requires huge investments and the presence of impurities such as SiO_2 and CaO contaminate synthesised diamond. Exploring high grade alumina as a substitute for magnesia seedpads material promises to bring some synthesis stability in seedpads material. The moisture test using percentage LOI method confirmed that moisture uptake in magnesia powder is greater than that of alumina powder. Malvern Mastersizer 2000 analyser results in Appendix A, Figure A1 give the specific surface area of magnesia (Nedmag) and alumina (KSM99) powder particles. The powders had different particle size distribution, the Nedmag powder had significantly larger particles compared to KSM99. The measured specific surface area was utilised to calculate the percentage of LOI per unit surface area of powders. The ratio of % LOI/unit surface area was larger for Nedmag an indication the magnesia powder absorbed more moisture than that calculated in the experimental % LOI results. Table 16 shows that magnesia powder absorbed moisture 8 times per unit area more than alumina powder.

Table 16 % LOI per surface area of the particle.

Material	Specific Surface area (mm^2/g)	Mass of sample (g)	Surface area of particles (mm^2)	LOI (%)	LOI/Surface area (%/mm^2)
Nedmag	1.05	20	21.0	0.115	0.00548
KSM99	3.51	20	70.2	0.051	0.00073

Magnesia (Nedmag) absorbs moisture in two forms: (i) through the crystalline lattice (bound water $MgO.H_2O$) [72], and (ii) through the hygroscopic particle surfaces known as free moisture. Water in the crystalline lattice is removed starting at temperatures of about 550 ^oC whilst free moisture is removed at temperatures of up to 200 ^oC [73].

The TGA graphs in Figure 64 confirm that water was removed in two stages (i) at temperature region of up to above 200 ^{o}C, surface moisture and (ii) at a temperature of 550 ^{o}C, crystalline bound moisture. [72]. A sharp mass loss increase would be attributed to decomposing of magnesium carbonate at temperatures of 350 ^{o}C [74], carbonates are formed from magnesium hydroxide kept for a prolonged time in ambient air due to reaction with carbon dioxide from the air. Alumina (KSM99) shows only free moisture removal in the early stages of TGA analysis and up to temperatures of up to 400 ^{o}C, once water evaporated or decomposed there was no evidence of other phase formation.

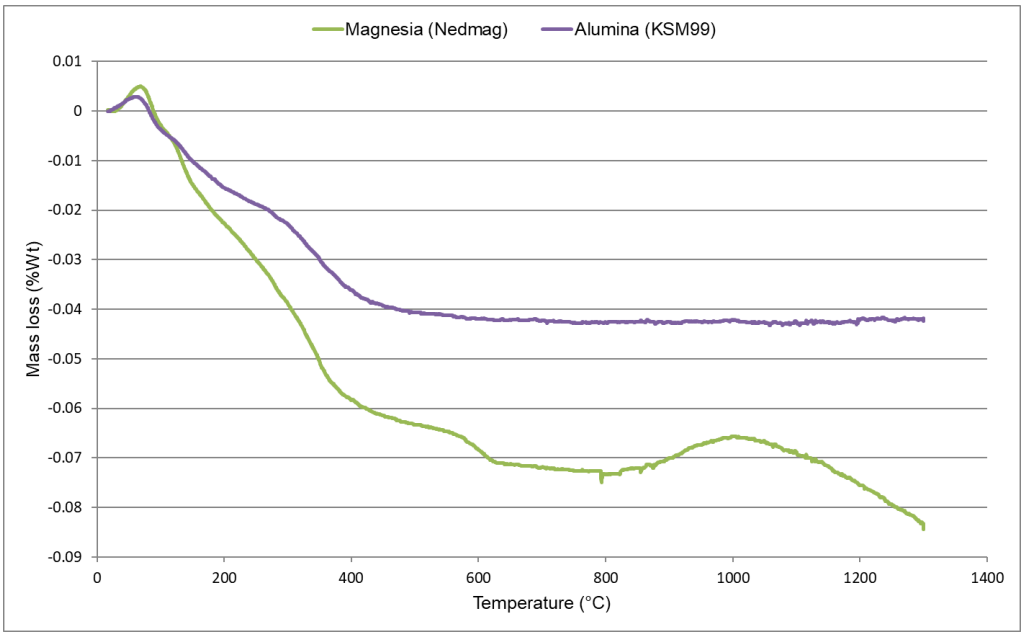

Figure 64 TGA graphs for magnesia (Nedmag) and alumina (KSM99) powders in synthetic air.

5.2 Components manufacture

Particle size distributions of spray dried magnesia and spray dried alumina powders were similar, and so were the relative densities of the resulting compacts. Figure 65 shows the particle sizes distribution accumulated at the same rate across all size ranges. Carr compressibility index and Hausner ratios indicated that both spray dried powders were free flowing, hence the powders performed in a fairly similar manner

during powder handling, volume feeding and particle positioning in the die filling during compaction in a uniaxial press. The moisture in compacted powders played a crucial role in preventing compact cracking during uniaxial compaction.

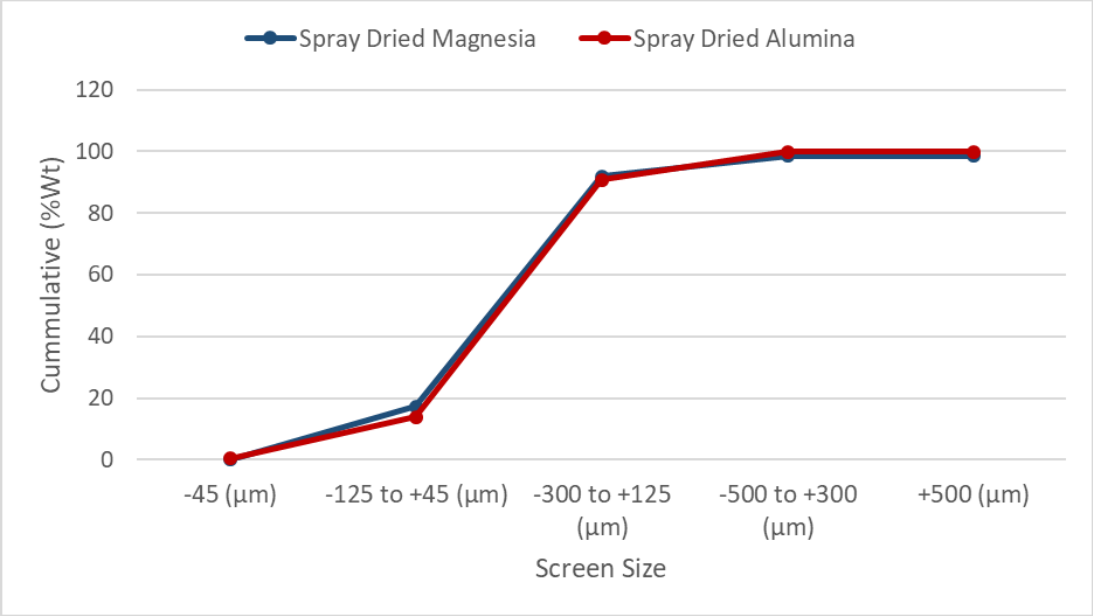

Figure 65 Cumulative particle size distribution of spray dried magnesia and spray dried alumina powders.

The moisture contents of the two spray dried powders were fairly similar and cracking was not prevalent on two green seedpads compacts. The LOI indicated binder content of spray dried powders was comparable, although magnesia had a higher LOI, this could be due to bound water absorbed in the crystalline lattice. The spray dried powders made green seedpads compacts that were easier to handle after uniaxial compaction.

The GMS granules were manufactured from tape casting slurry for fast drying on a steel belt, followed by granulation. The slurry was given sufficient time, an hour in the mixing process, to ensure a homogenous mixture of de-ionised water, Co, Fe, Ni and graphite was formed. The components of the slurry graphite and metals had a wider density difference and hence the tape casting was conducted while stirring the mixture.

GMS granules made from a dried tape cast and passed through a reducing Hydrogen furnace had metals reduced to acceptable oxygen levels of less than 300 ppm as per Element Six Pty Ltd standard. GMS granules were pressed in a uniaxial press to make green GMS slugs, followed by firing in a vacuum furnace to further reduce metal oxides in slugs that have been exposed to air to the oxygen level of less than 150ppm.

Magnesia and alumina seedpad compacts were fired in the air because they are inert to oxygen. Magnesia, alumina and GMS slugs green compacts were checked for green density before being fired in furnaces, green density predicted the fired components mass by using LOI as an equivalent of mass loss. The green GMS slugs were fired under purging argon because the metals Co, Fe and Ni could react with atmospheric oxygen and be oxidised.

5.3 Mechanical behaviour and properties of seedpads

Seedpads used in the HPHT diamond synthesis are subjected to capsule building and press compressive forces, hence they should withstand the mechanical forces so that they do not fall apart affecting diamond seeds orientation and spacing. A predictive test to study the mechanical behaviour of prepared cylindrical magnesia compacts and alumina compacts under compression conducted using an Instron test rig and Weibull statistics analysis gave a comparable characteristic strength for magnesia compacts 45.81 MPa, and alumina compacts 43.82 MPa. The average strength of ceramics was also comparable for both materials, with that for magnesia compacts being 43.45 MPa, and alumina compacts being 40.30 MPa. The characteristic strengths were greater than mean strengths for both magnesia and alumina, an indication both ceramics were likely to fracture above their mean values. The Weibull modulus for alumina compacts was 6.35 MPa, this was lower than that of magnesia 13.33 MPa, an indication of a wider spread in alumina flaw sizes in the compacts. The standard deviation for magnesia compacts 3.86 MPa was smaller than that of alumina compacts 6.38 MPa. Ceramics with a wider spread in strength values or a low value of Weibull modulus are less reliable when subjected to compressive stresses.

The values of the percentage of the theoretical density of the ceramics indicate that the porosity of alumina compacts was higher than that of the magnesia compacts. The stress vs strain graph for alumina was not as smooth as the magnesia graph and this was an evidence of the presence of a broad-size range population of flaws in the alumina samples. The particle size distribution obtained from Malvern Mastersizer 2000 analyser was not similar for magnesia (Nedmag) and alumina (KSM99), this resulted in a difference in sintering properties of the two materials. The spread in magnesia was wider and promotes good cold compaction packing and subsequent sintering, the spread in alumina powder is narrower and does not promote good packing and sintering.

The compressive strength of a fully dense or 100% of theoretical density alumina is far higher than that of 100 % theoretical density magnesia at 5500 MPa and 1666.6 MPa, respectively [27]. The compressive strength of both magnesia and alumina obtained for the fired seedpad materials have median values of 47 MPa due to the lower density of alumina 59% than magnesia 72%. The holes in spray dried alumina powder shown in Figure 66 may have become flaws that promoted subcritical crack growth of the many flaws that material, being more than 40% porous would contain.

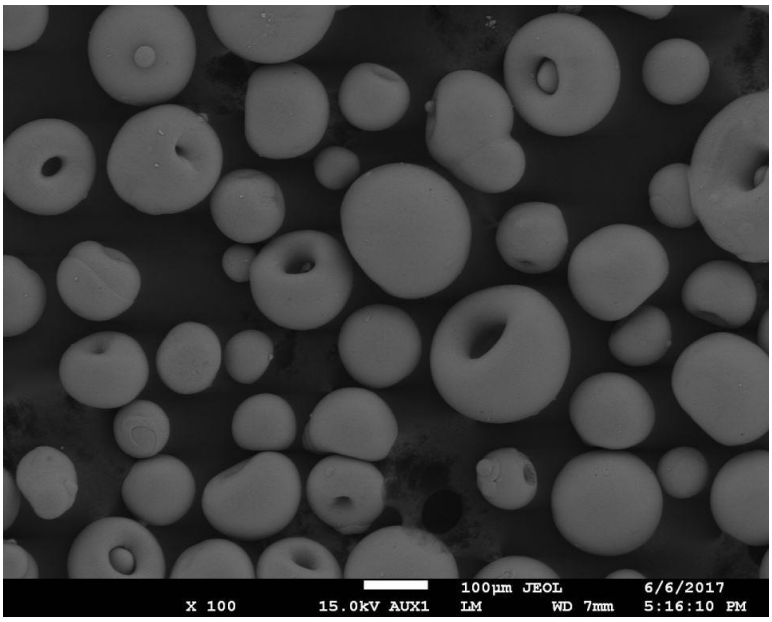

Figure 66 SEM image of alumina spray dried particles with some voids.

Improvement on the spray drying of alumina is necessary to obtain good void free granules, Figure 66 SEM image shows pores in alumina granules. Alumina compacts with minor transverse cracks were removed from the population used for the compression tests. However, some cracks may have been internal and not have been removed. Reduction in size and number of flaws can improve alumina fracture strength.

5.4 Diamond synthesis

Mechanical strength, purity and moisture absorption stability shown by alumina provided stability required for diamond synthesis, hence GMS slugs were assembled into capsules for HPHT diamond synthesis test. The SEM-EDS of Magnesia seedpad and alumina seedpad materials did not show any evidence of reacting with GMS, nor evidence of diffusion of GMS metals Fe, Ni and Co into both seedpads materials. Metal solvents loaded with carbon did not diffuse into magnesia and alumina due to poor wetting. It was necessary for metals to remain in the graphite matrix, their concentration was required for successful diamond synthesis. Graphite, magnesia and alumina remained solid at synthesis temperature 1450 ^{o}C because of high melting points. Graphite has a high sublimation temperature of 3642 ^{o}C at atmospheric pressure, the melting points of magnesia and alumina at atmospheric pressure, are 2852 ^{o}C and 2070 ^{o}C, respectively. Diamond synthesised from magnesia and alumina seedpads had similar shape and colour, the impurities in diamond were not assessed at this stage. The diamond seeds cubic shape did not change after HPHT diamond synthesis and this indicated thermodynamic conditions (pressure and temperature) favouring cubic crystal habit. No changes to synthesised diamond colour were noted and this showed no interference of both magnesia and alumina ceramics with the diamond lattice structure or composition.

Chapter 6: Conclusion

The instability of magnesia seedpads with respect to moisture absorption from the atmosphere and the presence of impurities in the supplied magnesia (Nedmag) powder is not desirable for HPHT synthesis and diamond growth stability. Magnesia absorbs ambient air moisture that can be removed at temperatures of up to above 200 ^{o}C, and some moisture further reacts with magnesia to form chemically bound moisture that can be removed at temperatures of above 400 ^{o}C. Availability of pure grade and mechanical stability of alumina seedpads with respect to moisture absorption serves to eliminate investments required to pre-treat magnesia seedpads in a vacuum furnace at 1100 ^{o}C to reduce impurities metal oxides before HPHT diamond synthesis.

Seedpads are subjected to handling during capsule assembly and initial compressive forces in the HPHT diamond synthesis. Mechanical strength of seedpads is crucial in holding seeds at defined orientation and spacing. Mechanical behaviour of magnesia seedpads compacts and alumina seedpads compacts proved to be similar with respect to withstanding fracture during capsule building and initial HPHT compaction. The seedpads further sinter during the HPHT diamond synthesis to full density, thus the initial density is crucial to prevent pressure loss and in order to achieve a reproducible pressure-temperature-time synthesis profile.

Magnesia seedpad and alumina seedpad materials did not diffuse or react with GMS slugs during HPHT diamond synthesis, this stability ensures a consistent ratio of graphite (C) and metal solvents (Ni, Co and Fe) in GMS slugs. The synthesised diamond colour and shape were not affected by the use of alumina seedpads material, the characteristics required in the grown diamond crystal.

References

[1] K. Yamauchi, N. Murayama, and J. Shibata, “Absorption and Release of Carbon Dioxide with Various Metal Oxides and Hydroxides,” Mater. Transactions, vol. 48, no. 10, 2007.

[2] R. Tappert and M. C. Tappert, ''Diamonds in nature, a guide to rough diamonds,'' Berlin, Springer-Verlag, 2011.

[3] “Alpha Alumina : Advanced Ceramics,” [Online]. Available at: http://repository.uobabylon.edu.iq/2010_2011/4_8526_258.pdf.

[4] M. A. Aswad, “Residual Stress and Fracture in High Temperature Ceramics,” The University of Manchester, 2012.

[5] “2008 Annual Report on Magnesia Market,” Asian Metal Ltd, 2008. [Online]. Available at: http://www.asianmetal.com/report/en/2008meisha_en.pdf.

[6] T. Sletten, “Aluminium Industry and Market,” [Online]. Available at: https://hydro.com/globalassets/1-english/investor-relations/other-presentations/2012/20120918---sparebanken-1-aluminium-presentation---ts-vs2.pdf.

[7] Z. Luo and A. Soria, “Prospective Study of the World Aluminium Industry Technical Report,'' EUR 22951 EN - 2007, Luxembourg, 2007.

[8] R. Riedel, “Handbook of Ceramic Hard Materials (Volume 2),” Weinheim, Wiley-VCH Verlag GmbH & Co. KGaA, 2000.

[9] D. Choudhary and J. Bellare, “Manufacture of gem-quality diamonds, a review,” Ceram. Int., vol. 26, no. 1, pp. 73–85, 2000.

[10] B. Y. D. & S. Nekarae, “Structure of Diamond and Sodium Chloride,” [Online]. Available at: www2.tissch.ir/fa/file/Exams/chemproj.pdf.

[11] G. Peschel, “Carbon-Carbon bonds: Hybridization,” [Online]. Available at: https://www.physik.fu-berlin.de/einrichtungen/ag/ag-reich/lehre/Archiv/ss2011/docs/Gina_Peschel-Handout.pdf.

[12] K. Miyoshi, “Structures and Mechanical Properties of Natural and Synthetic Diamonds.” Cleveland, Ohio NASA TM - Lewis Research Centre, 1998.

[13] H. O. Pierson, “Handbook of Carbon, Graphite, Diamond and Fullerenes.” New Jersey, Noyes Publication, 1993.

[14] F. P. Bundy, H. P. Bovenkerk, H. M. Strong, and R. H. Wentorf, “Diamond-graphite equilibrium line from growth and graphitization of diamond,” J. Chem. Phys., vol. 35, no. 2, pp. 383–391, 1961.

[15] P. S. Decarli and J. C. Jamieson, “Formation of diamond by explosive shock,” Science, vol. 133, no. 3467, pp. 1821–1822, 1961.

[16] F. P. Bundy, “Direct conversion of graphite to diamond in static pressure apparatus,” J. Chem. Phys., vol. 38, no. 3, pp. 631–643, 1963.

[17] J. C. Angus, H. A. Will, and W. S. Stanko, “Growth of diamond seed crystals by vapour deposition,” J. Appl. Phys., vol. 39, no. 6, pp. 2915–2922, 1968.

[18] J. M. Zazula, “On Graphite Transformations at High Temperature and Pressure Induced by Absorption of the LHC Beam 1 Introduction,” LHC Proj. Note, vol. 78, 1997.

[19] F. J. T. Carmichael, “Diamond-Graphite Equilibria The formation of diamond from graphite is simply a phase transformation.” [Online]. Available at: http://showard.sdsmt.edu/MET320/Handouts/Graphite_to_Diamond_pdf.pdf.

[20] “Diamond and Graphite: Calculating a Simple Phase Diagram,” 2012. [Online]. Available at: https://d32ogoqmya1dw8.cloudfront.net/files/NAGTWorkshops/petrology/teaching_examples/05-Diamond.v2.pdf.

[21] J. E. Field, “The Properties of Natural and Synthetic Diamond.” Cambridge, Academic Press, 1992.

[22] H. Kanda, “Crystal Growth of Diamond,” in Bulk crystal growth of electronic, optical and optoelectronic ceramics, Ibaraki, John Wily and Sons, Inc, 2005.

[23] T. Taniguchi, D. Dobson, A. P. Jones, R. Rabe, and H. J. Milledge, “Synthesis of Cubic Diamond in the Graphite-Magnesium Carbonate and Graphite-$K_2Mg(CO_3)_2$ Systems at High Pressure of 9-10 GPa Region,” J. Mater. Res., vol. 11, no. 10, pp. 2622–2632, 1996.

[24] Y. Palyanov, I. Kupriyanov, Y. Borzdov, D. Nechaev, and Y. Bataleva, “HPHT Diamond Crystallization in the Mg-Si-C System: Effect of Mg/Si Composition,” Crystals, vol. 7, no. 5, p. 119, 2017.

[25] X. Liu, “A large volume cubic press with a pressure-generating capability up to about 10GPa,” High Press. Res., vol. 32, no. 2, pp. 239–254, 2012.

[26] H. Wang, “Note: An anvil-preformed gasket system to extend the pressure range for large volume cubic presses,” Rev. Sci. Instrum., vol. 81, no. 11, pp. 11–13, 2010.

[27] “AZO Materials,” 2001. [Online]. Available at: http://www.azom.com/properties.aspx?ArticleID=54.

[28] “ASM Alloy Phase Diagram Database.” [Online]. Available at: http://mio.asminternational.org/apd/index.aspx.

[29] H. Z. Harraz, “Beneficiation and Mineral Processing of Mineral Sands Beneficiation and Mineral Processing of Magnesium Minerals,” 2017. [Online]. Available at: https://www.researchgate.net/Magnesium-Minerals-Beneficiation-and-Mineral-Processing.pdf.

[30] “Chapter 2. Production and Processing of Aluminum.” [Online]. Available at: www.tms.org/pubs/books/4062.chapter2.pdf.

[31] K. Davis, “Material Review: Alumina (Al_2O_3),” Sch. Dr Stud. Eur. Union J., pp. 109–114, 2010.

[32] B. B. Karki and J. Crain, “Structure and Elasticity of MgO at High Pressure,” Am. Mineral., vol. 82, pp. 51–60, 1997.

[33] “Wikipedia,” 2017. [Online]. Available at: https://en.wikipedia.org/wiki/Magnesium_oxide.

[34] T. Shirai, H. Watanabe, M. Fuji, and M. Takahashi, “Structural Properties and Surface Characteristics on Aluminium Oxide Powders,” Annu. Rep. Ceram. Res. Lab. Nagoya Inst. Technol., vol. 9, pp. 23–31, 2009.

[35] R. Riedel, “Ceramic Science and Technology, Synthesis and Processing Vol 3,” Darmstadt, Wiley-VCH Verlag GmbH & Co. KGaA, 2012.

[36] P. Boch and J.-C. Nièpce, “Ceramics Materials - Process, Properties and Applications,” London, ISTE Limited, 2007.

[37] H. Hofmann and P. Bowen, “Powder Technology,” 2004. [Online]. Available at: https://pdfs.semanticscholar.org/7957/0bcbe143d868a714a141260cdfe81f8e14e0.pdf.

[38] J. Reed, “Principles of Ceramics Processing,” Second Edi. New York, John Wily and Sons Inc, 1995.

[39] J. G. Heinrich, “Introduction to the Principles of Ceramic Forming,” New York, Wiley Interscience, 1998.

[40] K. G. Ewsuk and J. G. Argüello, “Controlled Ceramic Powder Compaction Through Science-Based Understanding,” Key Eng. Mater., vol. 264–268, pp. 149–154, 2004.

[41] A. Kaiser and R. Lutz, “Uniaxial Hydraulic Pressing as Shaping Technology for Advanced Ceramic - Products of Larger Size,” vol. 59, pp. 230–234, 2011.

[42] R. W. CAHN, “Physical Metallurgy,” Fourth Edi. Amsterdam, North Holland, 1996.

[43] K. Bodišová, D. Galusek, P. Švančárek, V. Pouchlý, and K. Maca, “Grain Growth Suppression in Alumina via Doping and Two Step Sintering,” Ceram. Int., vol. 41, no. 9, Part B, pp. 11975–11983, 2015.

[44] S. Li, C. Song, X. Qin, and Z. Zeng, “Densification and grain growth behaviour of highly dense MgO ceramics in pressureless sintering,” Ceram. Int., vol. 41, no. 8, pp. 10148–10151, 2015.

[45] Z. Sun, B. Li, P. Hu, F. Ding, and F. Yuan, “Alumina Ceramics with Uniform Grains Prepared from Al_2O_3 Nanospheres,” J. Alloys Compd., vol. 688, pp. 933–938, 2016.

[46] R. C. Hibheler, “Mechanics of Material,” Eighth Edi. New York, Prentice-Hall, 2011.

[47] W. D. Calister, “Fundamentals of Material Science and Engineering,” Fifth Edit. New York, John Wily and Sons Inc, 2001.

[48] G. Murray, “Introduction to Engineering of Materials,” Second Edi. London, Taylor and Frances, 2007.

[49] W. F. Hosford, “Mechanical Behaviour of Materials.” Cambridge, Cambridge University Press, 2005.

[50] R. Riedel, “Handbook of Ceramic Hard Materials (Volume 1).” Weinheim, Wiley-VCH Verlag GmbH & Co. KGaA, 2000.

[51] J. B. Quinn and G. D. Quinn, “A Practical and Systematic Review of Weibull Statistics for Reporting Strengths of Dental Materials,” Dent. Mater., vol. 6, no. 26, pp. 135–147, 2009.

[52] J. Kübler and P. L. J. Gauckler, “Mechanical Properties of Ceramics, Lecture Notes,” ETH Zurich Materials Department, 2010.

[53] “Albemarle Martoxid: Aluminium oxide KMS 99 Specification,” 2009. [Online]. Available at: http://www.martinswerk.de/pdf/newsletter_kms.pdf.

[54] “Magnesium Oxide - nedMag99 DIN 50 - E Specification,” 2006. [Online]. Available at: http://www.nedmag.nl/sites/default/files/downloads/nedMag 99 DIN 50.pdf.

[55] “Getting Started - Manual Malvern Instruments.” Worcestershire WR14 1XZ, Malvern Instruments Ltd, 2007.

[56] “A Guidebook To Particle Size Analysis : Horiba,” 2013. [Online]. Available at: http://www.horiba.com/fileadmin/uploads/Scientific/Documents/PSA/PSA_Guidebook.pdf.

[57] “A&D Moisture Analyser Instruction Manual for MS 70 MX 50 MF 50 ML 50,” A&D Company Ltd, Tokyo, 2004.

[58] S. Rudolph, “Establishment of the Characteristics of the Various UHPU Powders using Hosokawa Powder Characteristics Tester Manual,” Springs, Element Six Pty Ltd, 1977.

[59] R. N. Dave, “Particle and Powder Flow Properties- Part II Topics / Outline,” NJ Centre for Engineered Particulates Purdue University, West Lafayette, 2006.

[60] M. Copley, “Measuring Powder Flow Characteristics - A Test of Quality,” Manufacturing Chemist, 2008. [Online]. Available at: www.copleyscientific.com.

[61] S. Speakman, “Basics of X-ray Diffraction,” Cambridge, Massachusetts Institutes of Technology (MIT), 2001.

[62] P. Brouwer, “Theory of XRF - Getting Acquainted with the Principles.” Almelo PANalytical B.V., 2010.

[63] M. S. Shackley, “An Introduction to X-ray Fluorescence (XRF) Analysis in Archaeology,” Berkeley, Business Media, 2011.

[64] K. Majumdar, “Theory of X-ray Diffraction.” [Online]. Available at: http://studylib.net/doc/10957174/theory-of-x-ray-diffraction-kingshuk-majumdar.

[65] R. Riley, “Bragg’s law for X-ray Crystal Diffraction - Topic 5a Lecture Notes XRD,” IOP Publishing. [Online]. Available at: http://stacks.iop.org.

[66] “X-ray Powder Diffraction II Peak Positions and Indexing - Solid State Chemistry Lecture 10,” Ohio State University, 2005. [Online]. Available at: https://www.researchgate.net/file.PostFileLoader.html.

[67] D. Dean, “Thermal Gravimetric Analysis,” Birmingham, University of Alabama, 2003.

[68] J. Ltd, “Jeol Application Data Sheet Reference SEM SM-A-004-OOE.” Joel Ltd, 2011.

[69] Philips, “The Philips FEG SEM User Manual Handbook,” Eindhoven, Philips Ltd, 2000.

[70] J. Lawrence, “ASTM International: Standard Test Method for Monotonic Compressive Strength of Advanced ceramics at ambient temperature C1454.” Pulp Books, West Conshohocken, 2016.

[71] S. Luidold and H. Antrekowitsch, “Hydrogen as a reducing agent: State-of-the-art science and technology,” Jom J. Miner. Met. Materials Soc., vol. 59, no. 6, pp. 20–26, 2007.

[72] Z. Pan and C. Y. Zhao, “Dehydration/Hydration of MgO/H_2O Chemical Thermal Storage System,” Energy, vol. 82, pp. 611–618, 2015.

[73] M. E. Aphane, “The Hydration of Magnesium Oxide with Different Reactivities by Water and Magnesium Acetate,” Pretoria, University of South Africa, 2007.

[74] C. Unluer, “Characterization of Light and Heavy Hydrated Magnesium Carbonates Using Thermal Analysis,” Therm. Anal. Calorim., vol. 1, no. 115, 2014.

Appendicies

Appendix A Characterisation of powders

Malvern analyser results showing specific surface area used to calculate LOI/area of particles

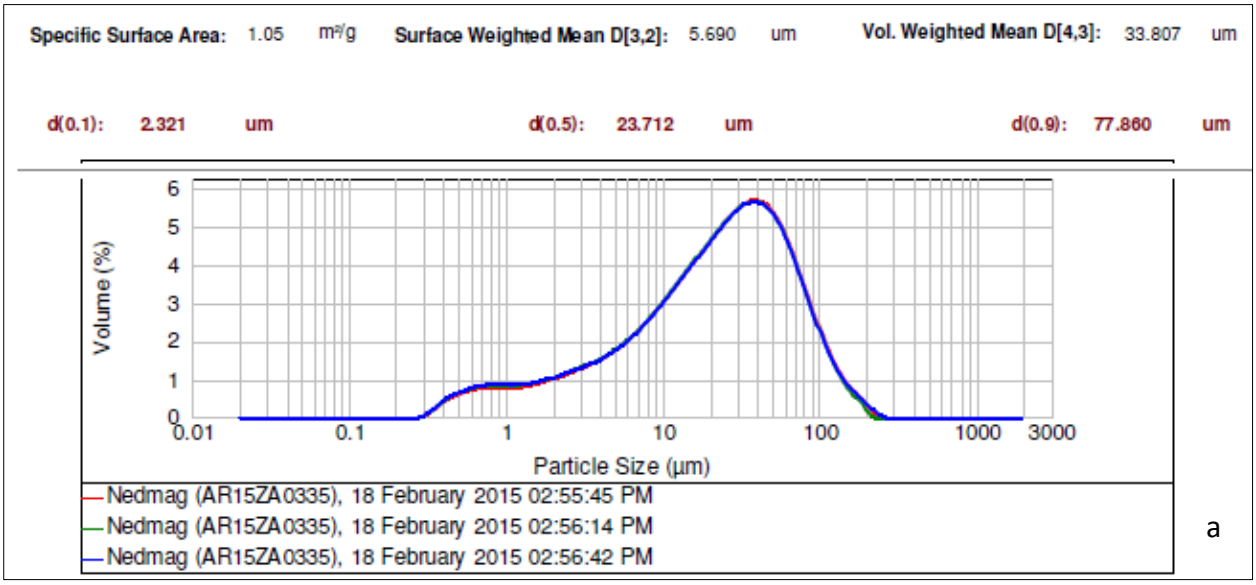

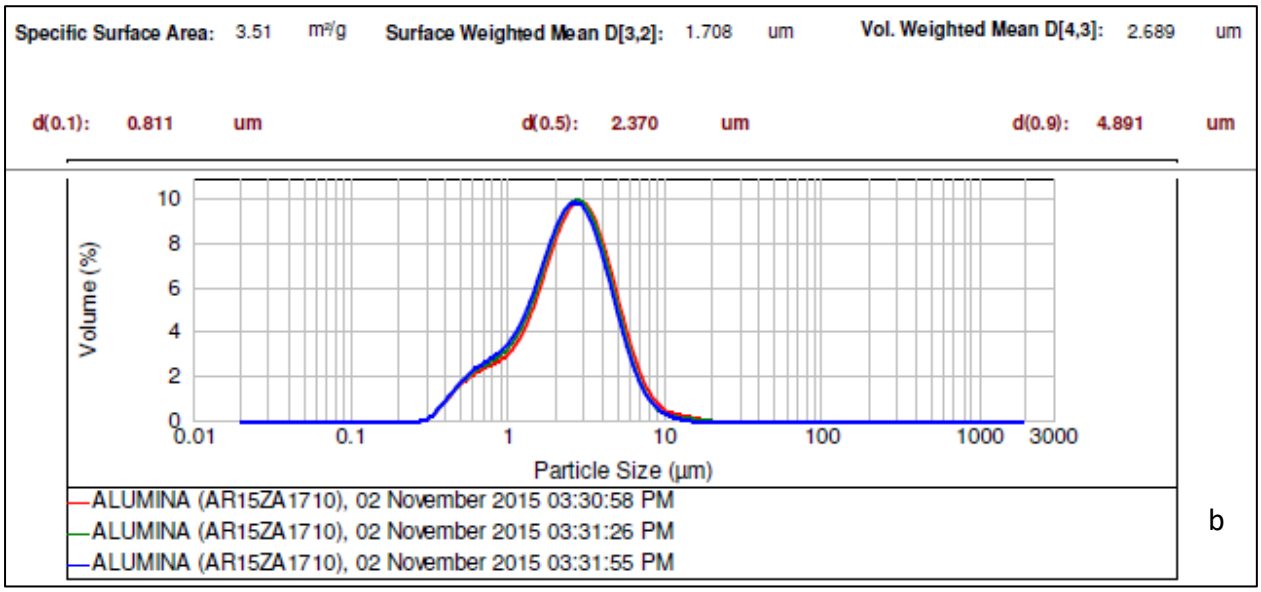

Figure A1 (a) magnesia (Nedmag) (b) alumina (KSM99) powder particle size distribution (before spray drying).

XRF of spray dried magnesia and alumina powders to determine the purity of magnesia and alumina.

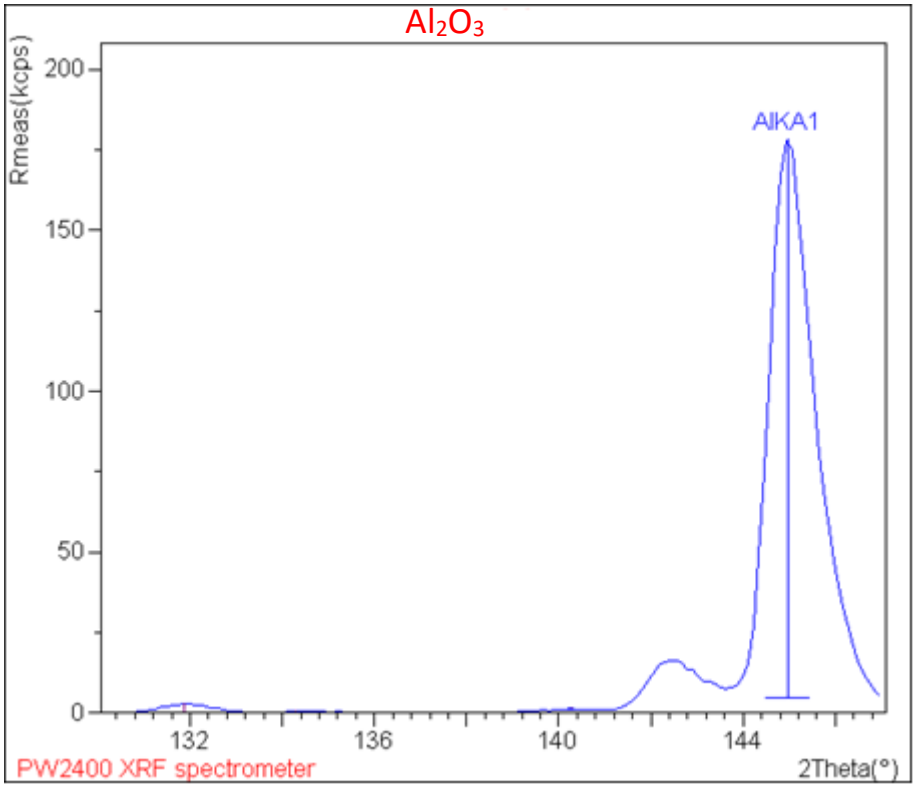

Figure A2 XRF results of spray dried alumina.

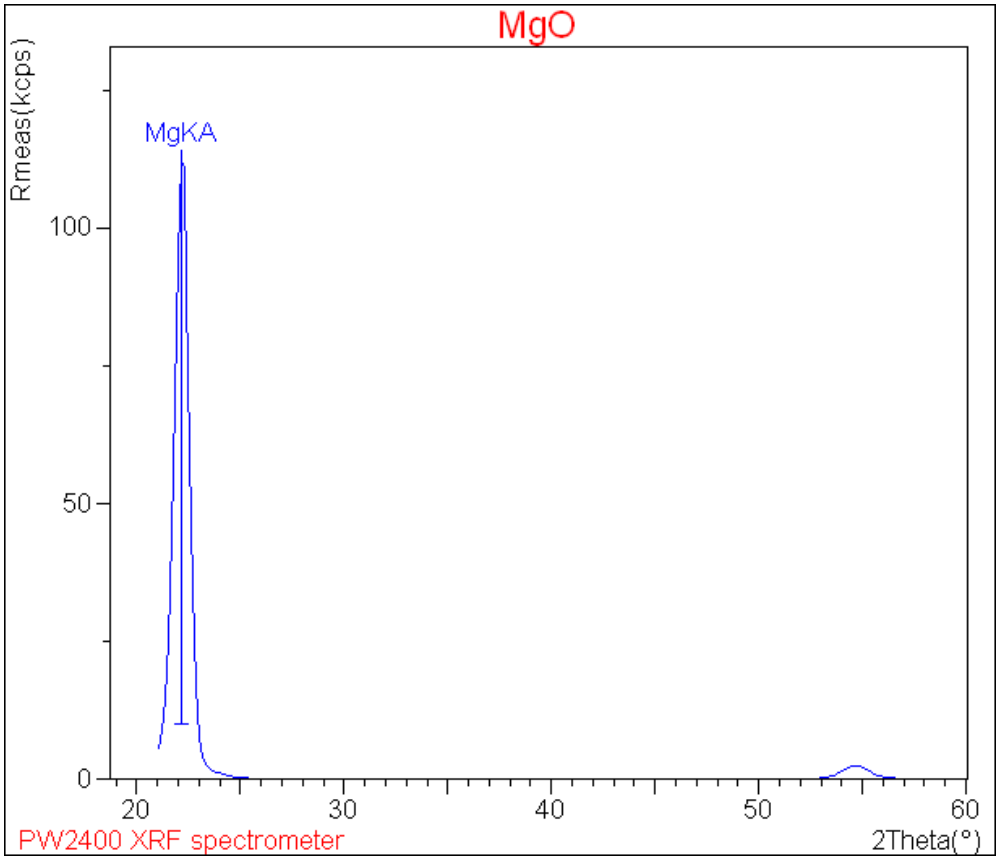
MgO
Rmeas(kcps)
MgKA
100
50
0
20
30
40
50
60
PW2400 XRF spectrometer
2Theta(°)

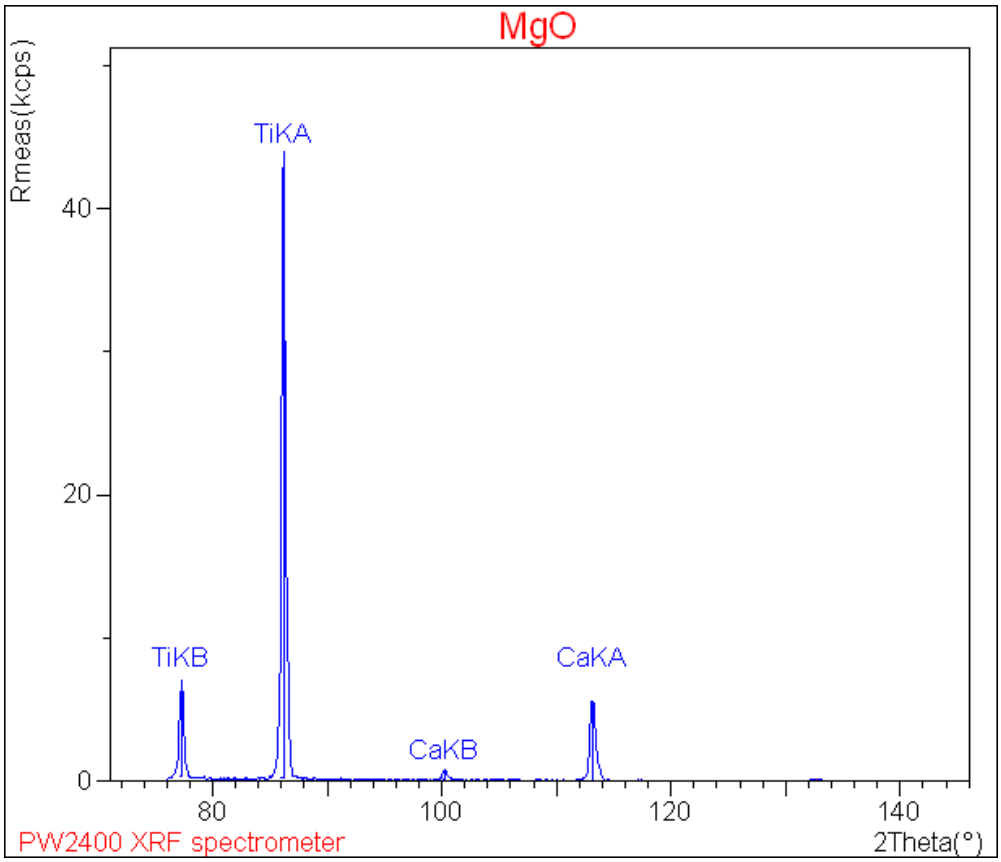
MgO
Rmeas(kcps)
TiKA
40
20
0
TiKB
CaKB
CaKA
80
100
120
140
PW2400 XRF spectrometer
2Theta(°)

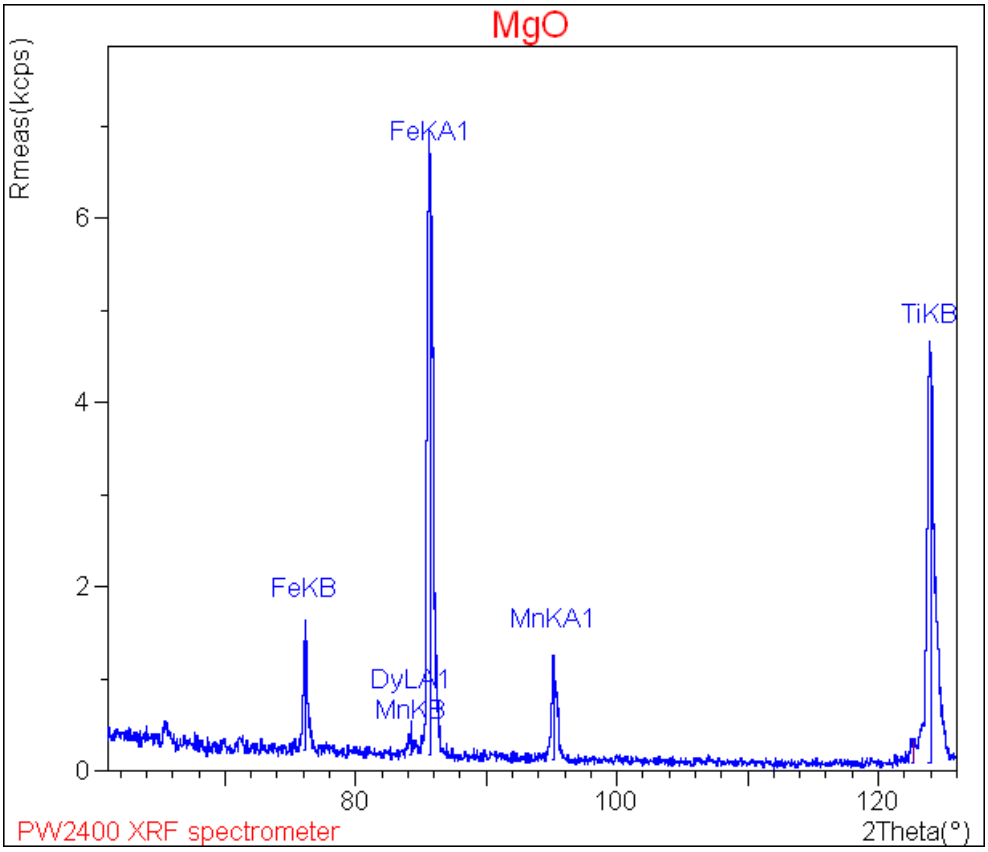

Figure A3 XRF results of spray dried magnesia.

Appendix B Components manufacturing

Results of components pressing at various pressure to achieve the desired density are shown in the tables below.

Table 17 Pressed results of (a) green magnesia seedpads (b) alumina seedpads.

	Magnesia green seedpad (a)				**Press Pressure**	
Sample	**OD (mm)**	**Thickness (mm)**	**Mass (g)**	**Density (g/cm^3)**	**Hydraulic (bar)**	**Die (MPa)**
1	40.98	6.16	20.50	2.52	30	147
2	40.94	6.06	20.09	2.52	30	147
3	40.95	6.10	20.23	2.52	30	147
4	41.01	5.57	20.44	2.78	110	539
5	41.03	5.54	20.24	2.76	110	539
6	41.00	5.42	19.98	2.79	110	539

	Alumina green seedpad (b)				**Press Pressure**	
Sample	**OD (mm)**	**Thickness (mm)**	**Mass (g)**	**Density (g/cm^3)**	**Hydraulic (bar)**	**Die (MPa)**
1	40.98	6.55	20.09	2.33	30	147
2	40.93	6.60	20.31	2.34	30	147
3	40.96	6.57	20.17	2.33	30	147
4	40.95	6.41	20.64	2.45	110	539
5	40.94	6.56	21.02	2.44	110	539
6	40.96	6.25	20.18	2.45	110	539
7	40.98	6.17	20.19	2.48	150	735
8	40.97	6.16	20.20	2.49	150	735
9	40.98	6.14	20.19	2.49	150	735

Table 18 Fired compacts results of (a) magnesia seedpads (b) alumina seedpads.

	Fired magnesia seedpads (a)					Press Pressure	
Sample	OD (mm)	Thickness (mm)	Mass (g)	Density (g/cm^3)	Density (%)	Hydraulic (bar)	Die (MPa)
1	40.87	6.15	19.64	2.40	67.04	30	147
2	40.89	6.05	19.48	2.45	68.52	30	147
3	40.97	6.77	19.92	2.23	62.38	30	147
4	40.98	5.45	19.46	2.71	75.66	110	539
5	40.99	5.55	19.89	2.72	75.90	110	539
6	40.98	5.47	19.62	2.72	76.00	110	539

	Fired Alumina seedpads (b)					Press Pressure	
Sample	OD (mm)	Thickness (mm)	Mass (g)	Density (g/cm^3)	Density (%)	Hydraulic (bar)	Die (MPa)
1	40.54	6.41	19.19	2.32	58.60	30	147
2	40.66	6.48	19.14	2.28	57.47	30	147
3	40.55	6.49	19.34	2.31	58.30	30	147
4	40.57	6.18	19.47	2.44	61.57	110	539
5	40.6	6.26	19.56	2.41	60.98	110	539
6	40.6	6.23	19.65	2.44	61.55	110	539
7	40.65	6.12	19.53	2.46	62.12	150	735
8	40.66	6.14	19.49	2.45	61.77	150	735
9	40.66	6.11	19.43	2.45	61.88	150	735

Appendix C Mechanical behaviour of materials

Table 19 Magnesia compacts results.

Sample	Diameter	Area	Length	L/D	Max load	Fracture Strength	Mass	Density	Density
Units	(mm)	(mm^2)	Mm		(kN)	(MPa)	(g)	(g/cm^3)	%
1	13.84	150.4	21.96	1.59	6.354	42.2	8.40	2.54	0.71
2	13.85	150.7	21.82	1.58	6.876	45.6	8.49	2.58	0.72
3	13.89	151.5	21.81	1.57	6.000	39.6	8.50	2.57	0.72
4	13.94	152.6	22.07	1.58	6.882	45.1	8.44	2.51	0.70
5	13.88	151.3	21.88	1.58	7.624	50.4	8.36	2.53	0.71
6	14.12	156.6	22.11	1.57	7.394	47.2	8.55	2.47	0.69
7	13.89	151.5	22.09	1.59	7.090	46.8	8.56	2.56	0.71
8	13.85	150.7	21.93	1.58	7.137	47.4	8.60	2.60	0.73
9	13.90	151.7	22.06	1.59	6.984	46.0	8.54	2.55	0.71
10	13.89	151.5	21.98	1.58	6.215	41.0	8.45	2.54	0.71
11	13.85	150.7	22.01	1.59	6.306	41.9	8.49	2.56	0.72
12	13.86	150.9	21.76	1.57	6.384	42.3	8.52	2.60	0.72
13	13.87	151.1	21.97	1.58	6.473	42.8	8.51	2.56	0.72
14	13.87	151.1	22.01	1.59	5.361	35.5	8.47	2.55	0.71
15	13.87	151.1	22.17	1.60	5.390	35.7	8.49	2.53	0.71
16	13.94	152.6	22.07	1.58	7.304	47.9	8.56	2.54	0.71
17	13.87	151.1	22.06	1.59	6.432	42.6	8.55	2.57	0.72
18	13.86	150.9	21.99	1.59	6.254	41.4	8.45	2.55	0.71
19	13.83	150.2	21.78	1.57	6.800	45.3	8.46	2.58	0.72
20	13.81	149.8	21.97	1.59	6.326	42.2	8.47	2.57	0.72
Minimum	13.81	149.79	21.76	1.57	5.36	35.48	8.36	2.47	0.69
Maximum	14.12	156.59	22.17	1.60	7.62	50.38	8.60	2.60	0.73
Average	13.88	151.40	21.98	1.58	6.58	43.45	8.49	2.55	0.71
Std. dev.	0.06	1.41	0.12	0.01	0.61	3.86	0.06	0.03	0.01

Table 20 Alumina compacts results.

Sample	Diameter	Area	Length	L/D	Max load	Fracture Strength	Mass	Density	Density
Units	(mm)	(mm^2)	(mm)		(kN)	(MPa)	(g)	(g/cm^3)	%
1	13.96	153.1	27.41	1.96	6.899	45.1	9.30	2.22	56%
2	13.70	147.4	27.74	2.02	5.696	38.6	9.01	2.20	56%
3	13.70	147.4	27.66	2.02	4.259	28.9	8.72	2.14	54%
4	13.65	146.3	27.07	1.98	5.239	35.8	9.32	2.35	59%
5	13.66	146.6	28.03	2.05	6.751	46.1	9.35	2.28	57%
6	13.69	147.2	27.75	2.03	6.307	42.8	9.33	2.28	58%
7	13.64	146.1	27.41	2.01	6.271	42.9	9.42	2.35	59%
8	13.69	147.2	27.17	1.98	6.997	47.5	9.37	2.34	59%
9	13.59	145.1	27.10	1.99	7.087	48.9	9.37	2.38	60%
10	13.76	148.7	27.10	1.97	6.656	44.8	9.44	2.34	59%
11	13.71	147.6	27.53	2.01	5.825	39.5	9.49	2.34	59%
12	13.70	147.4	27.51	2.01	5.852	39.7	9.47	2.34	59%
13	13.70	147.4	27.65	2.02	6.412	43.5	9.44	2.32	58%
14	13.72	147.8	27.27	1.99	3.366	22.8	9.30	2.31	58%
15	13.67	146.8	28.00	2.05	6.619	45.1	9.50	2.31	58%
16	13.65	146.3	27.82	2.04	5.599	38.3	8.99	2.21	56%
17	13.69	147.2	28.03	2.05	5.091	34.6	9.26	2.24	57%
18	13.68	147.0	27.30	2.00	6.232	42.4	9.30	2.32	59%
19	13.61	145.5	27.40	2.01	6.932	47.7	9.45	2.37	60%
20	13.72	147.8	28.31	2.06	4.616	31.2	9.90	2.37	60%
Minimum	13.59	145.1	27.07	1.96	3.366	22.8	8.72	2.14	54%
Maximum	13.96	153.1	28.31	2.06	7.087	48.9	9.90	2.38	60%
Average	13.69	147.3	27.56	2.01	5.935	40.3	9.34	2.30	58%
Std. dev.	0.07	1.6	0.35	0.03	1.003	6.8	0.23	0.07	2%

Table 21 Weibull analysis

	ln(Fracture Strength)				lnln(1/(1-Pf))	
I	**MgO**	**Al_2O_3**	**Pf= (i-0.5)/20**	**%Pf**	**MgO**	**Al_2O_3**
1	3.57	3.13	0.025	2.5	-3.68	-3.68
2	3.57	3.36	0.075	7.5	-2.55	-2.55
3	3.68	3.44	0.125	12.5	-2.01	-2.01
4	3.71	3.54	0.175	17.5	-1.65	-1.65
5	3.72	3.58	0.225	22.5	-1.37	-1.37
6	3.73	3.64	0.275	27.5	-1.13	-1.13
7	3.74	3.65	0.325	32.5	-0.93	-0.93
8	3.74	3.68	0.375	37.5	-0.76	-0.76
9	3.75	3.68	0.425	42.5	-0.59	-0.59
10	3.75	3.75	0.475	47.5	-0.44	-0.44
11	3.76	3.76	0.525	52.5	-0.30	-0.30
12	3.81	3.76	0.575	57.5	-0.16	-0.16
13	3.81	3.77	0.625	62.5	-0.02	-0.02
14	3.82	3.80	0.675	67.5	0.12	0.12
15	3.83	3.81	0.725	72.5	0.26	0.26
16	3.85	3.81	0.775	77.5	0.40	0.40
17	3.85	3.83	0.825	82.5	0.56	0.56
18	3.86	3.86	0.875	87.5	0.73	0.73
19	3.87	3.86	0.925	92.5	0.95	0.95
20	3.92	3.89	0.975	97.5	1.31	1.31

Appendix D Synthesis

Results of diffusion of various elements between seedpads and GMS slugs.

Table 22 Composition of various elements through seedpads and GMS interface.

Material	(μm)	Carbon (%)		Seedpads (%)		Fe (%)		Co (%)		Ni (%)	
Section	Distance	Magnesia	Alumina	Magnesia	Alumina	Magnesia	Alumina	Magnesia	Alumina	Magnesia	Alumina
Seedpads side	3080.030	40.3		13.02		0	0	0	0	0	0
	2852.475	39.18		14.32		0	0	0	0	0	0
	2616.993	37.39		14.9		0.94	0	0	0	0	0
	2379.088	39.55		13.13		0	0	0	0	0	0
	2147.294	39.85	12.48	13.41	36.86	0	0.57		0.8	0	0
	1938.688	37.58	13.83	15.65	35.23	0	0	0	0.68	0	0
	1685.547	36.81	15.29	16.38	35.03	0	0	0	0	0	0
	1481.550	36.42	17.76	16.08	30.51	0.5	0	0	0	0	0
	1215.848	35.28	20.94	17.78	30.79	0	0	0	0.67	0	0
	982.434	32.54	18.58	19.86	33.32	0	0	0	0	0	0
	849.488	33.59	19.93	18.75	32.36	0	0	0	0	0	0
	755.077	33.86	21.94	18.59	28.84	0	0	0	0	0	0
	560.190	33.43	21.02	19.03	31.26	0	0	0	0	0	0
	359.866	33.73	19.01	18.98	30.56	0	0	0	0	0	0
	173.527	37.27	21.94	16.07	30.04	0	0	0	0	0	0
	0.000	41.61	22.97	14.19	29.22	0	0	0	0	0	0
GMS slug side	0.000	57.83	36.81	0	0	24.81	43.78	2.27	3.07	7.43	11.28
	-226.185	43.71	40.94	0	0	35.66	41.28		2.62	11.68	10.63
	-438.504	42.3	45.02	0	0	38.35	36.55			10.51	10.23
	-636.642	43.22	45.37	0	0	37.48	40	3.35		11.42	10.8
	-894.337	42.64	43.87	0	0	36.78	37.39			11.56	10.33
	-1093.646	44.98	39.02	0	0	33.92	41.03	2.37		10.89	11.92
	-1321.004	44.36	44.76	0	0	36.81	36.93	2.7		10.86	10.85
	-1538.907	41.19	45.7	0	0	34.98	40.01	2.44	3.1	11.88	11.19